

**DESIGN OF AN ACTIVE HELICOPTER CONTROL
EXPERIMENT AT THE PRINCETON ROTORCRAFT
DYNAMICS LABORATORY**

**Andrew M. Marraffa
R. M. McKillip, Jr.**

**Department of Mechanical and Aerospace Engineering
Princeton University
Princeton, NJ 08544-5263**

**Principal Investigator: R. M. McKillip, Jr.
Technical Report No. 1861T**

**NASA Ames Research Center Grant No. NAG 2-415
Experimental Studies in System Identification
of Helicopter Rotor Dynamics**

NASA Technical Officer for this Grant: S. Jacklin

**INTERIM REPORT
Covering the period January 1988-May 1989**

May 1989

Design of an Active Helicopter Control Experiment at the Princeton
Rotorcraft Dynamics Laboratory

ABSTRACT

In an effort to develop an active control technique for reducing helicopter vibrations stemming from the main rotor system, a helicopter model was designed and tested at the Princeton Rotorcraft Dynamics Laboratory (PRDL). A description of this facility, including its latest data acquisition upgrade, are given. The design procedures for the test model and its Froude scaled rotor system are also discussed.

The approach for performing active control in this paper is based on the idea that rotor states can be identified by instrumenting the rotor blades. Using this knowledge then, Individual Blade Control (IBC) or Higher Harmonic Control (HHC) pitch input commands may be used to impact on rotor dynamics in such a way as to reduce rotor vibrations. This paper discusses an instrumentation configuration utilizing miniature accelerometers to measure and estimate first and second out-of-plane bending mode positions and velocities. To verify this technique, the model was tested in the PRDL. Resulting data were used to estimate rotor states as well as flap and bending coefficients, procedures for which are discussed.

Overall results show that a cost- and time-effective method for building a useful test model for future active control experiments was developed. With some fine-tuning or slight adjustments in sensor configuration, prospects for obtaining good state estimates look promising.

LIST OF FIGURES

- Fig. 1.1 Rotor blade reaction forces at hinge.
- Fig. 2.1 Description of the Princeton Rotorcraft Dynamics Lab.
- Fig. 2.2 Data acquisition functional diagram.
- Fig. 3.1 Helicopter test model arrangement.
- Fig. 3.2 a Rotor blade and holder arrangement (side view).
- Fig. 3.2 b Rotor blade and holder arrangement (top view).
- Fig. 3.3 Typical transfer function.
- Fig. 3.4 Cambell diagram of rotor blade properties.
- Fig. 3.5 Blade accelerometer dynamics.
- Fig. 3.6 Impact test locations.
- Fig. 3.7 a Transfer functions for positions 10 through 7.
- Fig. 3.7 b Transfer functions for positions 6 through 4.
- Fig. 3.7 c Transfer functions for positions 3 through 1.
- Fig. 3.8 a Coherence functions for positions 10 and 9.
- Fig. 3.8 b Coherence functions for positions 8 and 7.
- Fig. 3.8 c Coherence functions for positions 6 and 5.
- Fig. 3.8 d Coherence functions for positions 4 and 3.
- Fig. 3.8 e Coherence functions for positions 2 and 1.
- Fig. 3.9 1st and 2nd bending modeshape data with 5th-order polynomial fits.
- Fig. 3.10 Accelerometer position layout in a rotor blade.
- Fig. 4.1 a Model-strain gauge balance adapter setup (side view).
- Fig. 4.1 b Model-strain gauge balance adapter setup (rear view).
- Fig. 5.1 One per rev ramp signal.
- Fig. 5.2 One per rev clock.
- Fig. 5.3 Forward flight velocity (tachometer output).
- Fig. 5.4 Reference blade pitch angle (θ_1).

- Fig. 5.5 Second blade pitch angle (θ_2).
- Fig. 5.6 Third blade pitch angle (θ_3).
- Fig. 5.7 Tip accelerometer response (acc. 6, out-of-plane).
- Fig. 5.8 Accelerometer 4 response (out-of-plane).
- Fig. 5.9 Accelerometer 3 response (out-of-plane).
- Fig. 5.10 Root accelerometer response (acc. 1, out-of-plane).
- Fig. 5.11 Accelerometer 5 response (lead-lag).
- Fig. 5.12 Accelerometer 2 response (lead-lag).
- Fig. 5.13 Aerodynamic x-force.
- Fig. 5.14 Aerodynamic y-force.
- Fig. 5.15 Aerodynamic z-force.
- Fig. 5.16 Aerodynamic Roll moment.
- Fig. 5.17 Aerodynamic Pitch moment.
- Fig. 5.18 Aerodynamic Yaw moment.
- Fig. 5.19 Pre-filtered accelerometer output from acc. 1.
- Fig. 5.20 Pre-filtered accelerometer output from acc. 3.
- Fig. 5.21 Pre-filtered accelerometer output from acc. 4.
- Fig. 5.22 Pre-filtered accelerometer output from acc. 6.
- Fig. 5.23 First mode displacement estimate.
- Fig. 5.24 First mode velocity estimate.
- Fig. 5.25 First mode acceleration measurements.
- Fig. 5.26 Second mode displacement estimate.
- Fig. 5.27 Second mode velocity estimate.
- Fig. 5.28 Second mode acceleration measurements.
- Fig. 5.29 Non-dimensional flap spring coefficient.
- Fig. 5.30 Non-dimensional flap damping coefficient.
- Fig. 5.31 Non-dimensional first mode pitch forcing coefficient.
- Fig. 5.32 Non-dimensional second bending mode spring coefficient.

Fig. 5.33 Non-dimensional second bending mode damping coefficient.

Fig. 5.34 Non-dimensional second bending mode pitch forcing coefficient.

LIST OF SYMBOLS

a	...	2-dimensional lift coefficient curve slope
a_n	...	non-rotating beam frequency coefficient for nth mode
b	...	number of rotor blades
c	...	blade chord
e	...	offset of flap hinge or point of fixity from rotation axis
g	...	second mode
g_i	...	ith modal position
\dot{g}_i	...	ith modal velocity
\ddot{g}_i	...	ith modal acceleration
m_0	...	mass per unit length of beam at root
r_n	...	non-dimensional nth accelerometer location on blade
$u(t)$...	system input
$v(t)$...	system output
v_i	...	measurement noise
w_i	...	external disturbances
x	...	sting balance voltage outputs
x_d	...	differenced voltage outputs
y	...	six degree of freedom vector of model states
y_d	...	differenced force and moment inputs
X_k	...	x-force component of kth blade
Y_k	...	y-force component of kth blade
A_{1s}	...	longitudinal cyclic
B_{1s}	...	lateral cyclic
C_P	...	Power coefficient
C_Q	...	Torque coefficient

C_T	...	Thrust coefficient
EI_0	...	bending stiffness of beam at root
F	...	F-test value
$G_u(f)$...	power spectrum of u
$G_{uv}(f)$...	cross-spectrum between $u(t)$ and $v(t)$
H	...	sting balance calibration matrix
$H(f)$...	frequency response function
I_b	...	blade inertia
K_n	...	Southwell coefficient for the n th mode
K_{0n}	...	zero-offset Southwell coefficient
K_{1n}	...	offset correction factor to K_{0n}
L	...	model roll moment, rotor length (R)
M	...	model pitch moment, blade mass, modal sensitivity matrix
$M_{\beta}(t)$...	flap spring coefficient
$M_{\dot{\beta}/\Omega}(t)$...	flap damping coefficient
$M_{\theta_1}(t)$...	flap pitch forcing coefficient
$M_g(t)$...	second mode spring coefficient
$M_{\dot{g}/\Omega}(t)$...	second mode damping coefficient
$M_{\theta_2}(t)$...	second mode pitch forcing coefficient
N	...	model yaw moment
P	...	Power
R	...	rotor radius
R_{1k}	...	rotating frame radial force component on k th blade
R_{2k}	...	rotating frame tangential force component on k th blade
R_{3k}	...	rotating frame vertical force component on k th blade
$U(f)$...	Fourier transform of $u(t)$

$U^*(f)$...	complex conjugate of $U(f)$
$V(f)$...	Fourier transform of $v(t)$
V_{ni}	...	variance for n_i parameters
X	...	x-force acting on model
Y	...	y-force acting on model
Y_{mode1}	...	first mode shape function
Y_{mode2}	...	second mode shape function
Z	...	z-force acting on model
Z_k	...	z-force component of kth blade
β	...	first mode
γ	...	blade lock number
$\gamma_{xy}(f)$...	coherence function between x and y
η_i	...	ith mode shape function
θ_k	...	pitch angle of kth blade
θ_0	...	collective pitch command
ρ	...	air density at sea level
σ	...	solidity
ω_{NRn}	...	non-rotating natural frequency of the nth mode
ω_{Rn}	...	rotating natural frequency of the nth mode
Ω	...	rotor speed (Hz)
ψ_k	...	azimuth angle of kth blade

TABLE OF CONTENTS

	page #
Chapter 1 Introduction	
1.1 Motivation	1
1.2 Background	2
1.3 Thesis objectives	5
Chapter 2 The Princeton Rotorcraft Dynamics Laboratory	
2.1 The facility	6
2.2 The data acquisition system	8
2.3 Data collection and manipulation software	11
Chapter 3 Design of the test model	
3.1 Design objectives	14
3.2 Designing the model	15
3.2.1 Choosing the helicopter kit	16
3.2.2 The rotor blades	16
3.2.3 Powering the model	25
3.2.4 The servo actuators	26
3.2.5 Additional model modifications	27
3.3 Sensor configuration and instrumentation	29
3.3.1 Accelerometer signal content	29
3.3.2 Blade accelerometer installation	32
Chapter 4 Experimental procedure	
4.1 Test preparation	43
4.2 Test procedure	48
Chapter 5 Results and conclusions	
5.1 Resulting data and post-processing	50
5.2 Conclusions	55
References	91
Appendix	93

CHAPTER 1

Introduction

1.1 Motivation

For many years research has been going on in an effort to reduce vibrations in helicopters. There are three main sources of vibrations, and they can be placed in three categories, low, medium, and high frequency [1]. The highest frequency vibrations are caused mainly by the drive train. The medium frequency source is primarily the tail rotor which typically spins about five times as fast as the main rotor. The lowest frequency vibrations stem almost exclusively from the main rotor, and it is because of their low frequency that they are the most pronounced and destructive ones. These vibrations not only cause discomfort for pilots and passengers, but are also responsible for shortening the useful life of many components in the rotor system as well as in the fuselage of the helicopter. They lessen performance and in some instances are the limiting factor in achieving top flight speeds.

Over the years, many different active control methods have been used for tackling this vibrations problem. Probably the most successful approach so far has been the use of higher harmonic control (HHC) [2]. In this method, various points on the fuselage, often including the pilots seat, are instrumented with vibration sensors. These are to detect vibrations introduced to the fuselage by the rotor system via its shaft. Then, based on these measurements, high frequency blade pitch commands are input to the rotor system.

Although HHC methods have demonstrated good results in reducing vibrations, a different, more direct technique is suggested in

this paper, and is directly responsible for the experiment described subsequently. The objective is to skip difficult dynamic modeling processes and to identify rotor states directly by instrumenting them. This process would tackle the vibrations problem at its root, and by using individual blade control (IBC) based on rotor state knowledge, could conceivably correct it there.

The experiment which was directly motivated by these facts is described in this paper.

1.2 Background

Vibrations of the helicopter fuselage are the response to oscillatory forces acting at the roots of the rotor blades. These are transmitted through the shaft to the non-rotating frame. The periodic forces occur at $1/\text{rev}$ and nb/rev frequencies, where b is the number of rotor blades and n any positive integer. This phenomenon can be explained analytically [3,4].

The resulting forces acting on each blade hinge can be represented as in figure 1.1 by R_1 , R_2 , and R_3 . If Ψ were the azimuth angle of the zeroth (reference) blade, then $\Psi_k = \Psi + (2\pi k)/b$ would be that of the k^{th} blade. The corresponding components acting in the non-rotating frame would then be:

$$X_k = -R_{1k} \cos(\Psi_k) + R_{2k} \sin(\Psi_k)$$

$$Y_k = R_{1k} \sin(\Psi_k) + R_{2k} \cos(\Psi_k)$$

$$Z_k = -R_{3k}$$

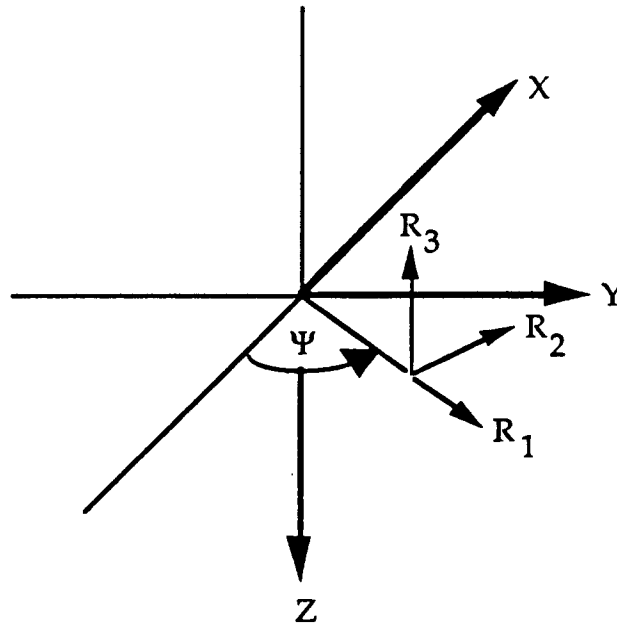


Fig. 1.1 Rotor blade reaction forces at hinge

Assuming steady flight conditions, R_{1k} , R_{2k} , and R_{3k} would be periodic and could be represented by Fourier expansions. Looking then at the overall X, Y, and Z forces transmitted through the shaft, they would take the forms of summations over the number of blades of the above equations with the R's in terms of their Fourier series. It can be shown mathematically [4] that by simplifying these expressions, in the resulting series, all harmonic terms cancel except those which are integer multiples of b .

This fact played an important role in this experiment. A three bladed rotor was designed which would have that $3/\text{rev}$ excitation. Rotor blades were then designed with second out-of-plane natural bending modes close to this excitation frequency. This was desirable for future experiments. The ability to suppress vibration would be much easier to show if large vibrations were present. Thus, a major task was

created, to make a rotor blade with just such characteristics, as well as insure similarity between the three blades. A process for making the subject rotor blades was developed and the resulting specimen were tested for modal properties. The frequency ratios were found to be 3.4 and 1.3 for second and first out-of-plane bending modes, respectively. Thus, a test operating condition of 8 Hz (480 RPM) was chosen for the model at which both the first and second natural modes were in close neighborhood of the 1/rev and 3/rev forcings.

As mentioned earlier, IBC was to be implemented to control rotor states in future experiments. This type of control is possible through the use of a conventional swashplate setup in the case of a three bladed rotor. If the rotor azimuth angle were known throughout operation, then analog $\sin\Psi$ and $\cos\Psi$ functions could be produced and combined with desired individual blade pitch angles Θ_1, Θ_2 , and Θ_3 according to [6] as:

$$\Theta_0(\Psi) = 1/3 [\Theta_1(\Psi) + \Theta_2(\Psi) + \Theta_3(\Psi)]$$

$$A_{1s}(\Psi) = -2/3 [\Theta_1(\Psi)\cos(\Psi) + \Theta_2(\Psi)\cos(\Psi+\pi/3) + \Theta_3(\Psi)\cos(\Psi+2\pi/3)]$$

$$B_{1s}(\Psi) = -2/3 [\Theta_1(\Psi)\sin(\Psi) + \Theta_2(\Psi)\sin(\Psi+\pi/3) + \Theta_3(\Psi)\sin(\Psi+2\pi/3)]$$

Thus collective and cyclic commands would be the result and could be input through conventional actuators to the rotor system. As will be seen, this was accomplished using a 1/rev sensor combined with analog circuitry.

Using this background information along with other design features, this experiment was conceived. A model was built and tested in the Princeton Rotorcraft Dynamics laboratory with certain objectives

in mind.

1.3 Thesis objectives

In order to be able to show in the future that a closed-loop controller, by using rotor state knowledge, could impact on rotor dynamics and achieve vibration reduction, a model had to be built and tested. This was necessary to perform system identification and to verify that a rotor state estimator could actually yield realistic results based on the instrumented blade configuration.

Thus, the main objectives of this experiment were to build a usable model with correct scaling factors, and to test it in the Princeton Rotorcraft Dynamics Laboratory, which is also described. The model was to have Froude scaled rotor blades, one of which was instrumented with six accelerometers. These were used to estimate first and second out of plane bending modal position and velocity as well as first lag modal position and velocity.

The final step was to do a dynamic test of the fully instrumented model on the track. This required additional support electronics all of which are also described in this paper. Actual data and post-processed results showing rotor states as well as parameter estimates are presented.

CHAPTER 2

The Princeton Rotorcraft Dynamics Laboratory

2.1 The Facility

In the mid 1950's, the Princeton Dynamic Model Track (PDMT) was built for the purpose of investigating aerodynamic characteristics of V/STOL aircraft at slow forward velocities and near hover using powered Froude scaled models. The PDMT which has since been upgraded with a new data system is today known as the Princeton Rotorcraft Dynamics Laboratory (PRDL). It consists of a 750 foot long metal building with an approximately 30x30 foot cross-section, as described in figure 2.1. Along one side of the building runs a monorail track, on which a hydraulically driven carriage rests. The carriage is supplied with three-phase power which it picks up via brushes along one of two sets of four rails spanning the length of the track. This source may be tapped in the form of 400 cycle power at 115 volts AC. It is used by the drive system as well as any necessary on-board experiment support electronics. In order to allow mounting of large, heavy models near the center of the test section, the drive system was located on the near wall side of the track to counterbalance the model weight. Thus, the system is capable of carrying models weighing up to 60 pounds and spanning up to 8 feet in diameter at speeds approaching 30 feet/second.

There are two modes of operation at the PRDL. In the dynamic testing mode, models can be mounted on a ball bearing gimbal support. Using this setup, any undesirable degrees of freedom of the model may be constrained, while desirable ones may be left unconstrained allowing small translational freedom with respect to the carriage. While the

model is actually moving inside the carriage reference frame, its motions can be measured. Originally, an on-board analog computer could use these feed-back signals to accurately position the carriage with respect to the model. The carriage's dynamic performance is sufficient for following the model in the Froude time scale [5]. Combining this arrangement with the capability for precise position and velocity measurements provides a complete system for system identification [6]. During static testing, which will be implemented for this experiment, a model is rigidly mounted on a six-component strain gauge balance constraining all degrees of freedom in the carriage frame. The forces and moments acting on it are then measured during an experimental run at specified conditions. The steel boom to which the strain gauge balance is attached may be rotated to provide any angle of attack for the model. It may also be interchanged with another boom allowing models to be mounted and tested in ground effect.

At various points along the track, light bulbs can be installed to act as light switches to activate or deactivate several functions. For example, near the end of the track, a light switch disengages the hydraulic drive system and brakes the carriage. Then it throws it in reverse and retrieves it at high velocity until another switch is encountered several feet before the control room is reached. This switch again brakes the carriage and allows a controller to hit a mechanical stop switch. A light switch can also be used to activate smoke release for flow visualization experiments.

The main advantages of the PRDL are low power requirements during operation of the track, ability to control the models' flight velocities very precisely, and the removal of all wall boundary layer effects on the test subjects. Of course, the main disadvantages include

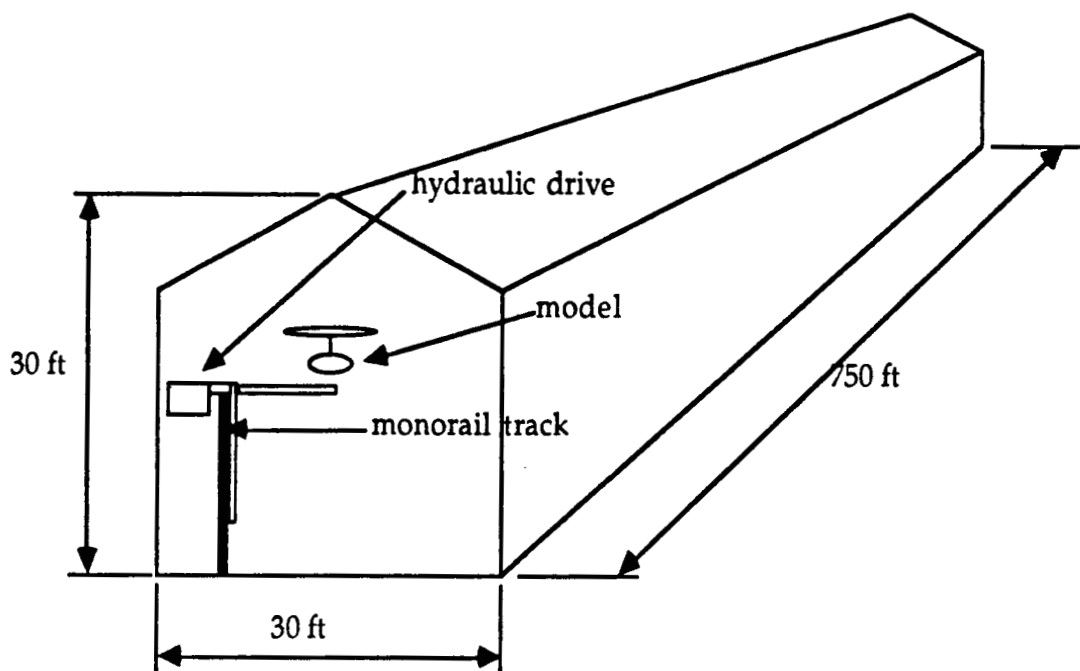


Fig. 2.1 Description of the PRDL

the fact that the carriage must be retrieved after each experimental run, thus disallowing continuous testing as may take place in wind tunnels. Also, in order to be able to look at data in real time, it must be telemetered from the moving reference frame to the control room.

2.2 The Data Acquisition System

One of the major upgrades that have taken place within the past two years is the data acquisition system. When the PRDL was originally built, there was no necessity for very high data sampling rates, since V/STOL aircraft flight dynamics happen on a relatively slow scale. Thus, the original data acquisition system had fairly low bandwidth. It was, however, capable of real-time data monitoring via strip chart recorders. After the telemetry system broke down, data was recorded during

experimental runs on magnetic tape on the moving carriage. At the end of each testing period, the tape had to be removed from the carriage and the information on it read into a computer for post processing. This system did not allow for real-time data monitoring.

Today, however, to make use of the PRDL facility for active helicopter control experiments such as the one described in this paper, greater demands are put on the data acquisition system. Signals from the instrumented blades must be sampled at high rates in order to obtain accurate rotor state profiles. The rotor in this experiment will be spinning at approximately 5 Hz during test conditions. Thus for samples on the order of 100 per revolution, a sampling rate of approximately 500 Hz would be necessary. Also, being able to monitor certain channels in real time could be very helpful in evaluating experimental runs on line, leading to more time efficient research. This is a not necessary but desirable characteristic to have.

Being faced with these new demands, a decision was reached to completely replace the old data acquisition system. A functional diagram of the new system is described in figure 2.2. It is based on the AYDIN VECTOR PDS-700 commutator and PAD-400 decommutator, both of which are fully documented [9,10]. The PDS-700 unit is capable of simultaneously sampling 44 channels at 1000 Hz each. 32 of these are high-level single-ended analog inputs while the other 12 are low-level strain gauge inputs. The commutator converts the 44 signals to 10 bit words corresponding to a voltage range between -5 and +5 volts. These words comprise a serial bit stream to the beginning of which two synchronization words are added. The result is a 46 word frame. This serial bit stream is then scaled to TTL voltage levels and fed into the American Laser Systems ALS-85 optical open-air transmitter [8]. This unit is mounted close to the supporting rail to minimize any vibratory

noise or misalignment effects. The highly directional optical signal is shot along the track while the carriage is moving and received by the ALS-85 receiver which is mounted at one end of the track. (An almost true monorail combined with accurate aligning sight glasses on each unit allow this type of system to work.) Next, the signal is sent via coax cable to the control room and into the PAD-400 decommutator box. From here the data is sent to a buffer card where an additional six channel identifier bits are added to each word. This buffer card performs several other functions as well. Two D/A converters and thumbwheels allow the operator to choose any two channels and look at them in real time on an oscilloscope. A frame clock divide is available to skip chosen frames of data. In addition, dip switches corresponding to each channel may be used to turn any unused channels off. These options allow sampling of data for longer periods of time by not filling the computer memory with useless information. From this point, data is sent directly into memory of an IBM PC/AT which is equipped with an HSD-16 card allowing direct memory access (dma). Using this card, data transfer rates of up to 120,000 16-bit words per second may be achieved, well beyond the 46,000 words per second requirement imposed by the PAD-400 decommutator.

Two sets of red and green LED's on the buffer box constantly display the decommutator's major and minor lock status. A green light indicates good lock. Data is read into the PC transparent to the central processor, such that it may be processed as it is coming in by the computer. This allows for real time data validity checks, the results of which can be used to adjust any parameters necessary for better results on line [8].

In order to manipulate the incoming data, a high level computer language had to be chosen to interface with the HSD-16 I/O card. The

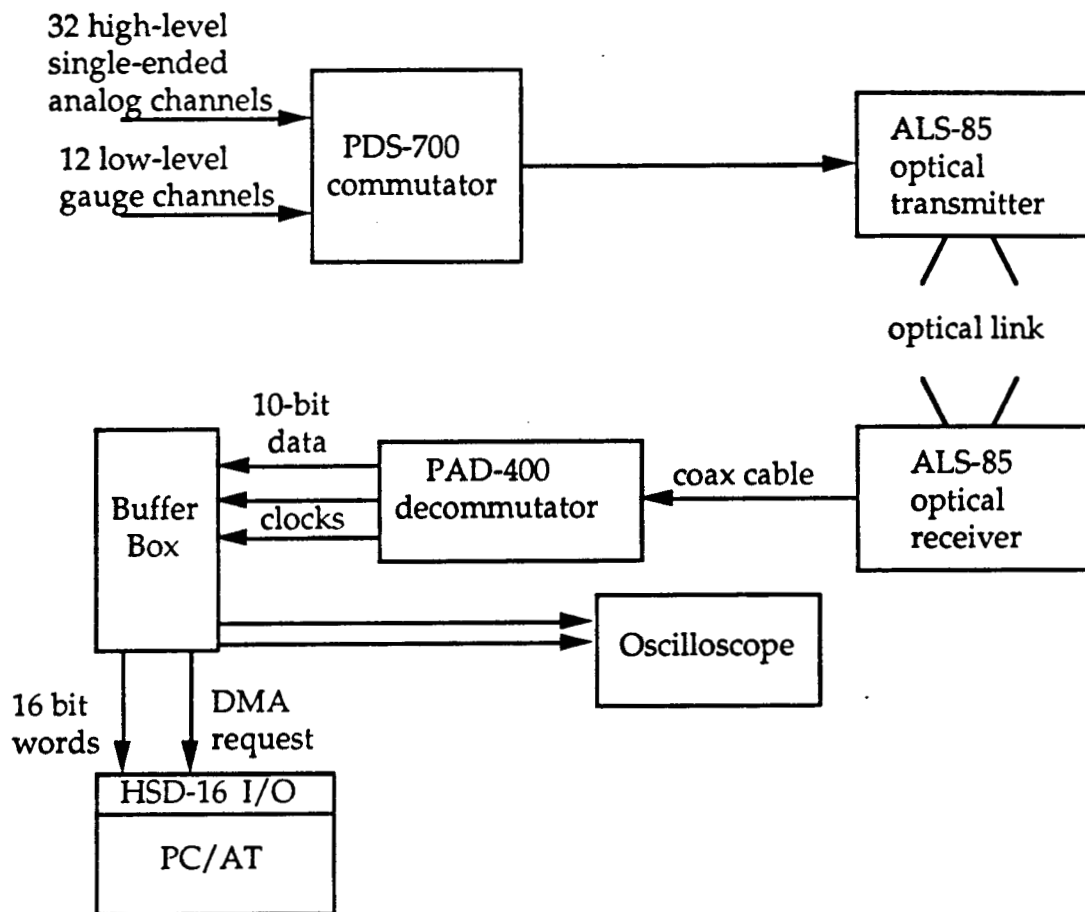


Fig. 2.2 Data acquisition functional diagram

APL language was picked for this task, since it is very convenient in the sense that it can easily be written and edited without cumbersome compilation delays and is very handy for data manipulation. APL may also call on compiled languages such as C or assembly to perform long iterative functions if necessary, by means of additional interface software [7].

2.3 Data Collection and Manipulation Software

Data may be sampled and written in several ways. If relatively few channels are to be sampled at slow rates such that only 10,000 or less elements will be written during the run, then this first method will suffice. While in the APL workspace DMA2APL, the menu driven function DMA must be called. Once it is entered, the operator is provided with 8 choices, according to which appropriate input data is requested by the program. If multiple channels are sampled at high rates, memory fills up very fast and much more space may be needed than can be provided in the first method. In this case, APL must be exited and the program DMA2FILE used. This routine will ask the user for the number of channels selected, sampling rate, and length of time data will be collected. It is very important that the response to number of channels coincides with the dip switches on the buffer box. Before data is written, the DMA trigger (toggle switch on buffer box) must be hit to ensure that it is collected from the beginning of a frame. Once the file is filled, the user is asked to provide a file name for the data. In this mode, 128 k of elements can be obtained at a time. A third method is available if sampling rates exceed 500 Hz while every other frame is skipped. In this case, data can't be written to memory fast enough and the program DMA2PAGE must be used. This program, however, limits the amount of data taken to 64 k [7].

Once data is written, it can be retrieved and processed within the APL environment. While in the DMA2APL workspace, the function GETCHN is used to get data from the file that was written earlier. When called upon, it requests that filename, the channel number, and the amount of data points desired. It will then check the top six bits of every data element and return with the ones corresponding to the given channel number. If more data is requested than was written, GETCHN

will return with -1's for excess requests. The function SCOPE is also available in the DMA2APL workspace. It is a semi-real time digital oscilloscope which can display various channel outputs on the graphics screen. In addition to DMA2APL, there are two other available workspaces, PLOTDATA and SPECTRAL. These contain plotting routines and spectral analyses tools, respectively. They are fully documented in reference 7.

CHAPTER 3

Design of the test model

3.1 Design objectives

Several limitations were imposed from the beginning in the design of the rotor model. One obvious restriction was that of a size and weight limit imposed by the test facility. Rotor span was limited to 8 feet or less in diameter and weight to 50 lbs or less. Lack of a full-time professional staff forced a different approach from the custom model construction techniques used in earlier V/STOL experiments. Thus, a cost and time effective method for building a model was sought. Since the objectives in this experiment pertain to rotor dynamics, the scaling of the rotor system became vital and that of the fuselage relatively unimportant, so long as it was scaled in size with respect to the rotor system. Specific characteristics of the rotor blades are discussed in subsequent sections. A method for instrumenting the rotor blades with sensors which would yield accurate rotor state measurements had to be developed. Also, in order to eventually be able to implement adaptive controls on the model, it was desired to have the capability of both individual blade control (IBC) and higher harmonic control (HHC).

These described some of the basic objectives to be met by the model to be tested in the PRDL. More specific requirements are discussed as they were encountered during the actual design phase.

3.2 Designing the model

To satisfy mainly the time and money constraints, an off-the-shelf radio control helicopter kit manufactured by Schlueter Inc., West Germany, was purchased. This type of kit which is readily available today, has reached a level of sophistication unavailable only several years ago. It was used as a structural basis for the test model, and is shown in figure 3.1 along with major modifications.

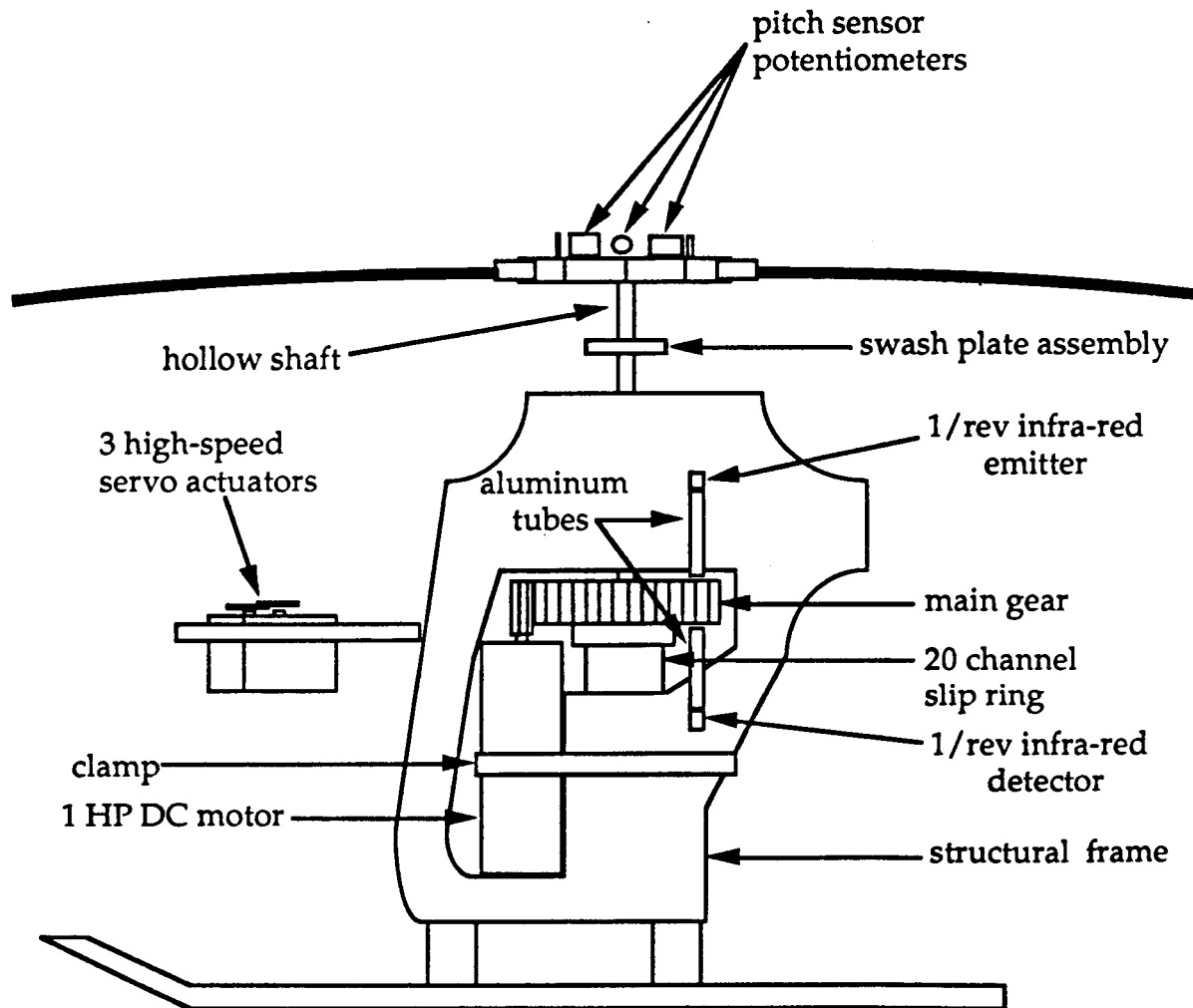


Fig. 3.1 Helicopter test model arrangement

3.2.1 Choosing the helicopter kit

The model support frame, as shown in the figure, was provided by the helicopter kit, as was the main gear, swashplate assembly, and rotor hub. The reason for choosing this model was because of its three-bladed rotor hub configuration, as well as its size and weight which were well below imposed limits. A three-bladed rotor was necessary to be able to use IBC without having to use actuators in the rotating frame. As was explained earlier, IBC can be implemented using a conventional swashplate setup as long as the rotor system consists of no more than three blades. This can physically be explained by the fact that the position of the swashplate in space is defined by three independent points. These, at any point in time, could conceivably define three independent pitch commands corresponding to individual blades. It is for this reason that a blade number less than four was chosen.

The option of a two bladed rotor was also available. The reason it wasn't taken was so that HHC could be implemented without interfering with pilot inputs. HHC commands are usually input at $(b-1)/\text{rev}$, b/rev , and $(b+1)/\text{rev}$ frequencies, where b is the number of blades. That means for a three bladed system, the lowest frequency closed-loop controls would be input at $2/\text{rev}$. In the case of a two bladed one, however, this would occur at $1/\text{rev}$. At that frequency, pilot commands are input, resulting in undesirable interferences in the two bladed rotor case.

3.2.2 The rotor blades

Since the helicopter kit came with a fiberglass fuselage, the size of the model's rotor blades was dictated by the necessity to maintain rotor to fuselage scaling. Thus, blades needed to be made which would be approximately 2 feet long with a 2 inch chord and display low first and

second bending mode frequencies (be relatively soft). With this in mind, a method for making rotor blades, which would assure aerodynamic similarity between them, was developed.

To obtain the necessary softness and flexibility for low frequency natural modes, a light weight foam material which could be poured into a mold in liquid form, was selected. This type of method, which had been used in past experiments, would also insure similarity between blades. Following this reasoning, the next step was to make a mold of a rotor blade with the following dimensional characteristics:

1. 2 foot span
2. 2 inch chord
3. NACA 0012 airfoil
4. no twist
5. no taper

The airfoil section was chosen because it is a standard symmetrical one used on vintage helicopters. No taper or twist simplified the process of making a mold. Because much time would go into making this mold, it was desirable to only have to do it once. This meant making a mold which could be used many times over without breaking or wearing. To meet these specifications, a rotor blade mold was machined out of two 3/4 X 3 X 26 inch aluminum slabs using a computerized Bridgeport milling machine located in the Jadwin machine shop at Princeton University.

The procedure involved writing a program in Anicam (see Appendix) on a minicomputer which was linked to the mill. Anicam is a language similar to Basic or Fortran. The program basically defined coordinates at the tip and root of one half of the blade. It then prompted the milling machine to carve out the material between these sets of coordinates, using specified cutting tools, spindle RPM's, and feed

rates. The procedure of milling was done in steps to assure a smooth finished surface and due to the large amount of material which had to be removed. Thus, a rough cut, consisting of two steps, which would mill to within .01 inches of the final cut, was done first. 14 cuts were made with a 1 inch ball mill from the trailing edge to 30% chord, milling from root to tip. Then, 6 cuts with a 1/8 inch ball mill were used to rough cut from 30% chord to the leading edge. This was necessary because of the small radius of curvature in the leading edge. Following the rough cutting, a 1 inch and a 1/16 inch ball mill were used to make 50 finished cuts from the trailing edge to 30% chord, and 30 finished cuts from that point to the leading edge, respectively. Taking advantage of the precision of the computerized Bridgeport, three aligning holes were then drilled along one edge of the mold. These were necessary to assure perfect aligning of the two mold pieces. Eventually, dowels were pressed into one of the halves and the holes enlarged in the other, allowing for a perfect fit every time.

Due to the many cuts performed by the milling machine, the process of milling one mold half lasted approximately 2.5 hours. The resulting pieces displayed very smooth surfaces, although ridges from the cutting procedure were visible.

Using this mold, a procedure for making the actual rotor blades was devised. A two part polyurethane foam manufactured by the SIG Mfg. company was acquired. In order to use this product with the mold, a release agent had to be found which would insure the blade's release from the mold without braking. After testing several possibilities such as glycerin, oils, etc., a paste car wax was chosen for its good release characteristics. The procedure for making a rotor blade consisted of several steps. First, the mold had to be lined with a very thin, uniform layer of release wax. The next step was to mix the two foam components

one part to one. Initially, 18 ml of each component were mixed together resulting in rotor blades weighing approximately 35 grams. However, after a 35 gram blade was eventually instrumented, it weighed approximately 48 grams. As a result, the two non-instrumented blades had to be made heavier to maintain weight balance. This was accomplished by mixing 24 ml of each foam component together, yielding approximately 48 gram rotor blades (these figures play an important role in achieving Froude scale characteristics). The mixing procedure turned out to be very crucial, as under- or over-mixing slightly meant less than maximum expansion. This would result in large air bubbles inside the blade, or simply an incomplete blade. A good indication that the foam had been mixed the proper amount was when small bubbles started to form on the surface of the mixture. This would happen within a matter of about one minute (one nice characteristic of the foam was that it didn't require external heat to react as was often the case with products used in the past). Once this point was reached, the foam was poured uniformly into the mold. It was then quickly closed and clamped shut with c-clamps to prevent foam from gushing out the sides. To obtain best results the mold was left overnight to allow curing. It was found that although the foam hardened in a matter of minutes, it was more advantageous to let it cure for 24 hours. This resulted in much easier release from the mold. The procedure of retrieving the rotor blade necessitated some carefulness. When slowly prying the mold open with a screwdriver at specially made slots, attention needed to be paid to what the blade was doing inside the mold. On one or two occasions a blade was lost because opposite ends were stuck to opposite mold pieces, resulting in a break when the mold was opened all the way. After a blade was removed successfully, fine grade sandpaper was used to smooth the seems which resulted from the molding procedure.

As was mentioned earlier, the blades' mass was an important parameter for scaling purposes. In order to obtain realistic experimental data, it was very desirable to have Froude scaled rotor blades. Froude scaling is scaling between aerodynamic and inertial forces. The lock number (γ) of a rotor blade, defined as

$$\gamma = \rho a c R^4 / I_b \quad , \text{ or}$$
$$\gamma = 3 \rho a c R^2 / M \quad , \text{ for } I_b = MR^2 / 3$$

is the ratio of aerodynamic and inertial forces acting on it. Hence, to obtain Froude scaled rotor blades, it was necessary for them to have realistic lock numbers. Full scale rotors usually have lock numbers between 8 and 13, this defining our acceptable range. As the definition of γ shows, the only freedom to vary once the blade mold was finished lay in the mass parameter, M . As a result, the blades weighing 35 and 48 grams had lock numbers of 11.4 and 8.3, respectively, both falling within the acceptable range.

To adapt the rotor blades to the rotor hub, blade holders were machined from aluminum. These were made as to hold the blades with friction as well as sets of two bolts. This unit in turn would fit into the blade holding slot of the rotor hub and be held in place by the lead-lag hinge. Figure 3.2 more clearly demonstrates this.

With this blade holder, a rotor blade could now be clamped down and tested for modal properties. In subsequent sections, it will be shown that first and second out of plane bending mode shapes become very important. How they were obtained will be discussed. At this point it was important to know if the rotor blades possessed low natural frequencies for these modes, such that good frequency ratios could be

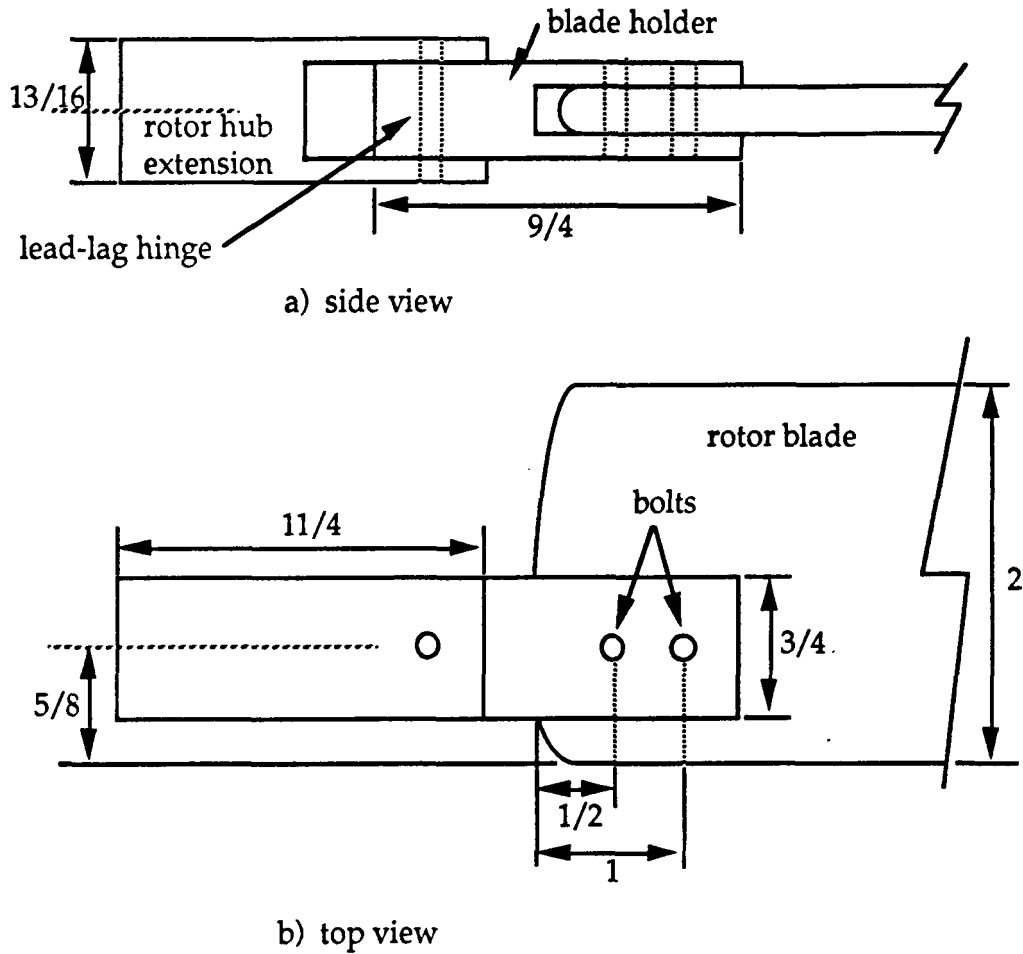


Fig. 3.2 a,b Side and top views of rotor blade and holder arrangement
(note: all dimensions in inches)

obtained at slow rotor speeds. To obtain this information, a blade was clamped down horizontally at its holder for impact testing. This type of modal analysis technique is thoroughly explained in reference 12. It consists of using a force hammer to create impulse force inputs to the blade. With a portable PC, the response of a miniature accelerometer, attached at the tip of the blade, as well as the hammer input, were sampled at 100 Hz. The transfer function between the output and input was then calculated and its frequency response plotted. This was done at

one impact point over several samples and also their average. A typical transfer function plot is shown in figure 3.3.

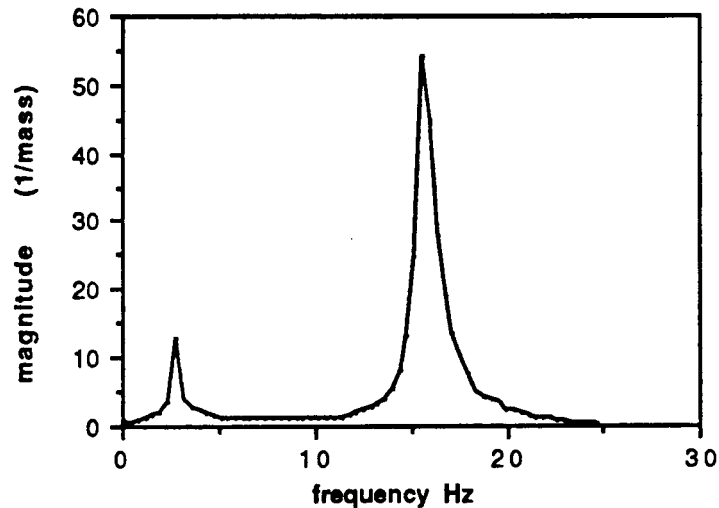


Fig. 3.3 Typical transfer function

The results showed that for a 48 gram rotor blade, the first and second out of plane bending mode natural frequencies (non-rotating) were 2.34 and 15.62 Hz, respectively (This is where the peaks occurred). These figures could now be used for determining frequency ratios. A method for finding rotating natural bending frequencies using non-rotating ones is described in detail in reference 13. It consists of augmenting the non-rotating frequency by the effected centrifugal stiffening depending on rotational speed as :

$$\omega_{Rn}^2 = \omega_{NRn}^2 + K_n \Omega^2 ,$$

where the subscript n signifies the nth mode, R and NR for rotating and non-rotating. K_n can be broken down to

$$K_n = K_{0n} + K_{1n}e ,$$

K_{0n} and K_{1n} being referred to as the zero-offset Southwell coefficient and offset correction factor for that coefficient. e is the offset of the flap hinge or point of fixity from the axis of rotation. ω_{NRn} can be represented in terms of a nonrotating-beam frequency coefficient a_n , and the mass stiffness of the beam at the root as

$$\omega_{NRn}^2 = a_n^2 (EI_0 / m_0L^4) ,$$

m_0 being mass per unit length at the blade root, and L the rotor length. For a cantilever beam with uniform mass and stiffness distribution,

$$a_1 \cong 3.5 \quad \text{and}$$

$$a_2 \cong 22.0$$

according to [14]. With these coefficients, the experimental results for ω_{NR1} and ω_{NR2} could be verified by showing that

$$\frac{\omega_{NR1}}{a_1} \cong \frac{\omega_{NR2}}{a_2}$$

Doing these calculations, results of .69 and .71 were found, being within 3% of each other. Values for K_{01} , K_{02} , K_{11} , and K_{12} were determined from sets of plots found in reference 13. They yielded:

$$K_{01} = 1.19, \quad K_{11} = 0.79$$

$$K_{02} = 6.2, \quad K_{12} = 4.1 .$$

With the offset e equaling .47 feet,

$$K_1 = K_{01} + K_{11} e = 1.56$$

$$K_2 = K_{02} + K_{12} e = 8.13 .$$

With these factors known, frequency ratios were determined to be :

$$\omega \text{ (1st bending) } / \Omega = 1.28 \quad \text{and}$$

$$\omega \text{ (2nd bending) } / \Omega = 3.43 \quad \text{at}$$

$$\Omega = 8 \text{ Hz.}$$

A Cambell diagram which shows approximate modal characteristics of the tested rotor blade is shown in figure 3.4.

In summary, important rotor blade and hub characteristics are listed as follows:

- 1) rotor blade radius : 2 feet
- 2) rotor blade chord : 2 inches
- 3) airfoil section : NACA 0012
- 4) ω (1st bending) / $\Omega \cong 1.3$ ($\Omega=8$ Hz)
- 5) ω (2nd bending) / $\Omega \cong 3.4$ ($\Omega=8$ Hz)
- 6) rotor hub configuration:
 - a) 3 blades
 - b) lead-lag hinge
 - c) no flap hinge

d) lag hinge offset : 3.9 inches

e) $e = 5.7$ inches

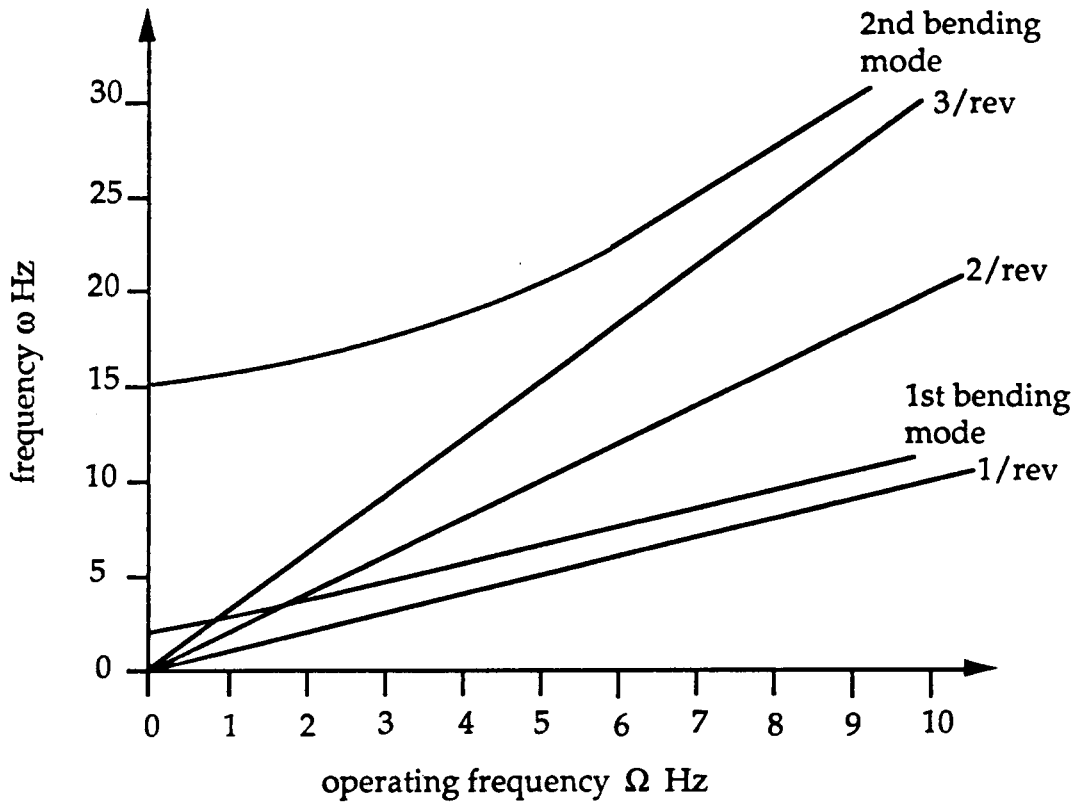


Fig. 3.4 Cambell diagram of rotor blade properties

3.2.3 Powering the model

With the given rotor system specifications, a power source for driving the model needed to be found and adapted to it. A simple required power calculation was performed. By conservatively assuming a thrust coefficient to solidity ratio (C_T / σ) of .1, where solidity is defined as total blade to disc area ratio or

$$\sigma = \frac{b \int_0^R c \, dr}{\pi R^2}$$

the thrust coefficient was determined to be 0.008.

By using the relationships

$$C_Q = \frac{C_T^{3/2}}{\sqrt{2}}$$

$$C_P = C_Q$$

$$P = C_P (\rho \pi R^2) (\Omega R)^3$$

necessary power was determined to be 0.9 HP at 480 RPM. These results helped in choosing a motor for driving the model. Because operating speed wasn't anticipated to be much more than 8 Hz, a 1.0 HP, permanent magnet, DC motor was used.

This motor was adapted to the helicopter model by attaching a gear comparable to the rotor's main gear to its drive shaft. The motor was then clamped into position against the helicopter's frame as is shown in figure 3.1.

3.2.4 The servo actuators

A set of three servo actuators was used for positioning the swashplate through pushrod assemblies. Located, as shown in figure 3.1, were JRS4051 high speed servos manufactured by JR CIRCUS inc. The setup was such that for lateral cyclic the two outside ones were used and for longitudinal cyclic, the middle one. Collective commands were

achieved with all three servos in combination.

Positioning of these off the shelf radio control (R.C.) actuators was accomplished with pulse width modulated (PWM) signals. To be able to input collective or cyclic commands, an integrated circuit (IC) card was designed. This card was to be carried by a card bus on the carriage. Its job was to take cyclic or collective inputs and electronically convert them into three individual servo commands, by generating and controlling pulses and their widths. Since both pilot as well as closed-loop control inputs would eventually go through this unit, it comprised an essential part for future experiments.

To determine these actuators' capabilities, a test was performed. Again making use of a portable PC, pitch input commands were sampled, sweeping through a range of frequencies. Pitch responses to these inputs, measured by pitch sensors, were also sampled. Transfer functions from this test revealed that the JR servos were effective up to approximately 3 Hz. For future closed-loop experiments attempting to reduce rotor vibrations, this would be insufficient.

3.2.5 Additional model modifications

Additional modifications to the stock helicopter kit were made in support of the rotor experimental program. Sensing each blade's pitch angle was a necessity for doing system identification as well as for future closed-loop experiments. Thus, for each blade, potentiometers were installed on the hub. By using a simple gear drive, pitch angles could be measured very accurately by ranging the potentiometers through a 30 volt differential (between +/- 15 volts).

In order to send signals from the rotating to the nonrotating reference frame, a slip ring had to be installed. This assembly had the

capability of twenty channels, a number limited by the size of the rotor shaft. As was noted in figure 3.1, a hollow shaft replaced the original. This part had to be machined out of a stock piece of steel, as drilling into the kit's hardened steel shaft was an impossibility. The procedure for machining the new shaft consisted of first drilling a hole into a large piece of steel. Then a lathe was used to cut that piece down, maintaining the hole as its center. Twenty wires were then installed to conduct signals from the rotor hub to the slipring base. How these channels were used will be described in subsequent sections.

Another important modification to the model was the addition of a 1/rev sensor. This sensor consisted of an infrared emitter-detector pair, mounted as shown in figure 3.1. Aluminum tubes were used for alignment as well as light shielding purposes. A small hole was drilled through the helicopter's main gear, resulting in a pulse once every revolution. This signal was fed into a phase lock loop card which would lock on to it. An LED and a beeper were installed to verify this lock. The card would then perform various functions with the locked-on signal. The 1/rev signal was routed to various locations in support of a host of timing applications. First, in order to generate the swashplate commands for Individual Blade Control inputs, the pulse was used to synchronize a sine/cosine function generator as part of the analog electronics on the swashplate command mixer card. In addition, the pulse drove a ramp generator that was fed into the commutator as an additional data channel. This ramp was used as an indicator of lost data in the telemetry signal, as the reconstructed signal would indicate discrete jumps in signal level for missing stretches of time-sampled data. Finally, the pulse was subdivided to provide synchronized sampling pulses for future use with carriage-mounted digital feedback control applications.

3.3 Sensor configuration and instrumentation

As was mentioned in chapter one, the objective in this experiment was to build a model whose rotor states could be identified by directly instrumenting the rotor blades. To be more specific, first and second out of plane bending modal position and velocity of one of the three blades were to be determined. To accomplish this, miniature accelerometers were used. This type of sensor configuration had been successfully used in previous system identification studies of helicopter rotor dynamics [8]. In this reference, first out-of-plane bending mode positions and velocities were estimated during hover using a rotor blade instrumented with two miniature accelerometers. This experiment demonstrated the advantages of accelerometer sensors over conventional strain gauges. In this type of application, strain gauges would encounter serious problems. When differentiating electronic position signals from the gauge, any spiky noise would spell disaster. This kind of problem is avoided by using accelerometers and electronically integrating to obtain velocity and position estimates.

3.3.1 Accelerometer signal content

Planted inside the rotor blade, the accelerometers would measure components of out-of-plane inertial as well as centrifugal acceleration. Figure 3.5 shows the sensor geometry. According to this setup, the accelerometers yield:

$$\text{accel}(t) = \ddot{z}(r,t) + r\Omega^2 \frac{dz(r,t)}{dr}$$

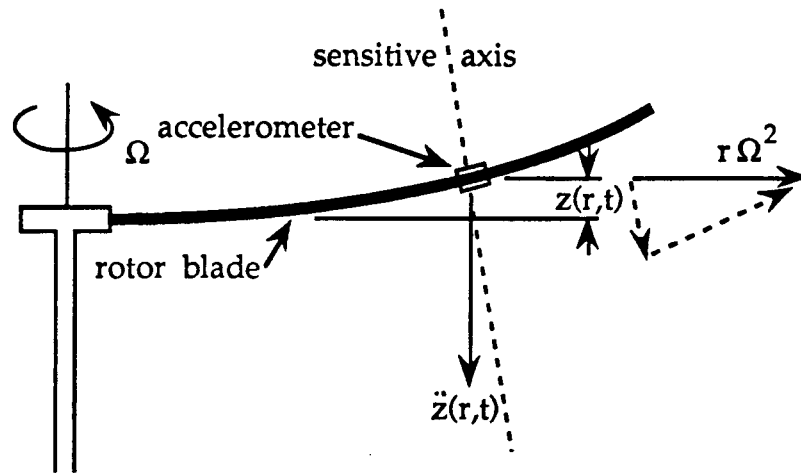


Fig. 3.5 Blade accelerometer dynamics

representing the out-of-plane inertial and centrifugal acceleration components along the accelerometer's sensitive axis. If the deflection of the rotor blades were represented in terms of a modal expansion:

$$z(r,t) = \sum_i \eta_i(r) g_i(t)$$

then each accelerometer content would be:

$$\text{accel}(t) = \sum_{i=1}^n \left[\eta_i(r) \ddot{g}_i(t) + r\Omega^2 g_i(t) \frac{d\eta_i(r)}{dr} \right]$$

n representing the number of modes considered in the expansion [15]. Being interested in only the first two out of plane modes, a set of four accelerometers needed to be installed. Their signal contents can be represented as follows:

$$\begin{bmatrix} \text{accel}_1 \\ \text{accel}_2 \\ \text{accel}_3 \\ \text{accel}_4 \end{bmatrix} = \begin{bmatrix} r_1 \Omega^2 \partial \eta_1(r_1) / \partial r & \eta_1(r_1) & r_1 \Omega^2 \partial \eta_2(r_1) / \partial r & \eta_2(r_1) \\ r_2 \Omega^2 \partial \eta_1(r_2) / \partial r & \eta_1(r_2) & r_2 \Omega^2 \partial \eta_2(r_2) / \partial r & \eta_2(r_2) \\ r_3 \Omega^2 \partial \eta_1(r_3) / \partial r & \eta_1(r_3) & r_3 \Omega^2 \partial \eta_2(r_3) / \partial r & \eta_2(r_3) \\ r_4 \Omega^2 \partial \eta_1(r_4) / \partial r & \eta_1(r_4) & r_4 \Omega^2 \partial \eta_2(r_4) / \partial r & \eta_2(r_4) \end{bmatrix} \begin{bmatrix} \beta(t) \\ \dot{\beta}(t) \\ g(t) \\ \ddot{g}(t) \end{bmatrix}$$

where η represents mode shape, β first bending mode position, $\dot{\beta}$ first mode acceleration, g and \ddot{g} second mode position and acceleration, and r_i the spanwise position of the i^{th} accelerometer. Thus, knowing the mode shapes of the first two out of plane bending modes, this 4x4 matrix (referred to as modal sensitivity matrix) could be inverted and post multiplied by the four accelerometer signals (It becomes evident here that because each sensor output actually comprises two components, twice as many sensors as desired modes are necessary to obtain an invertible matrix. For this reason, four accelerometers were used). This would result in first and second bending modal position and acceleration measurements. With this information, a kinematic observer, structured to avoid difficult dynamic modeling tasks, could be implemented. As described in detail in reference 16, the equations of motion can be written as:

$$\begin{bmatrix} \beta'(t) \\ \dot{\beta}(t) \\ g(t) \\ \dot{g}(t) \end{bmatrix} = \begin{bmatrix} 0 & 1 & 0 & 0 \\ 0 & 0 & 0 & 0 \\ 0 & 0 & 0 & 1 \\ 0 & 0 & 0 & 0 \end{bmatrix} \begin{bmatrix} \beta(t) \\ \dot{\beta}(t) \\ g(t) \\ \dot{g}(t) \end{bmatrix} + \begin{bmatrix} 0 & 0 \\ 1 & 0 \\ 0 & 0 \\ 0 & 1 \end{bmatrix} \begin{bmatrix} \beta(t) \\ g(t) \end{bmatrix} + \begin{bmatrix} 0 & 0 \\ 1 & 0 \\ 0 & 0 \\ 0 & 1 \end{bmatrix} \begin{pmatrix} w_1(t) \\ w_2(t) \end{pmatrix}$$

where w represents external disturbances. These equations basically say that modal position is the double integral of modal acceleration. Being that modal position measurements were available, the observation equations

$$y(t) = \begin{bmatrix} 1 & 0 & 0 & 0 \\ 0 & 0 & 1 & 0 \end{bmatrix} \begin{bmatrix} \beta(t) \\ \dot{\beta}(t) \\ g(t) \\ \dot{g}(t) \end{bmatrix} + \begin{bmatrix} 1 & 0 \\ 0 & 1 \end{bmatrix} \begin{pmatrix} v_1(t) \\ v_2(t) \end{pmatrix}$$

where v is measurement noise, could be included in a Kalman-filter type observer. This would yield a net result of integrating the acceleration information to obtain modal positions and velocities. The actual modal position measurements would be used for displacement error feedback to drive position and velocity estimation errors to zero [16].

3.3.2 Blade accelerometer installation

Having now structured the sensor arrangement, the task of instrumenting a rotor blade arose. Placement of the accelerometers became an important issue. The criterion for placing the sensors was the necessity to obtain accurate measurements. This would be achieved only if the modal matrix mentioned earlier were as invertible as possible. A measure of invertibility is given by the matrix's condition number. This was a parameter which could be varied as a function of placement of the accelerometers. However, to find optimum sensor positions, first the first and second bending mode shapes and their derivatives had to be determined and inserted into the modal matrix.

The mode shapes were determined using the previously mentioned

mode shape analysis technique [12]. Again, an impact hammer was used to impart impulse forces along a rotor blade, clamped down at its holder in the horizontal direction. The response of an accelerometer mounted as shown in figure 3.6 along with the input force were first sent through a low pass filter with a cutoff frequency of 25 Hz before being sampled. This was necessary to filter out unwanted high frequency information and, in the process, increase data quality. A portable IBM PC then sampled the data at 100 Hz. Using this data, frequency response functions $H(f)$ were determined for each impact test as:

$$H(f) = G_{uv}(f) / G_u(f)$$

where $G_{uv}(f) = U^*(f) V(f)$, cross-spectrum between $u(t)$ and $v(t)$

$U(f)$ = Fourier transform of system input $u(t)$

$V(f)$ = Fourier transform of system output $v(t)$

$G_u(f) = U^*(f) U(f)$, power spectrum of $u(t)$

U^* = complex conjugate of $U(f)$

This was done eight times at each of 10 impact locations distributed as in figure 3.6.

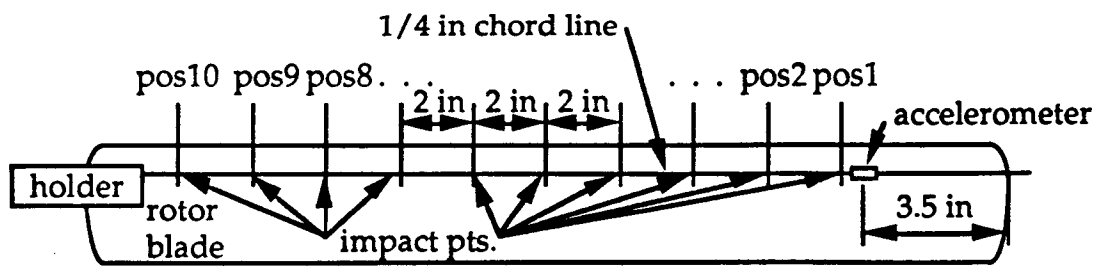


Fig 3.6 Impact test locations

For each of these sets of eight tests, transfer functions were averaged and plotted in the frequency domain. The results are summarized in figures

3.7 a through c.

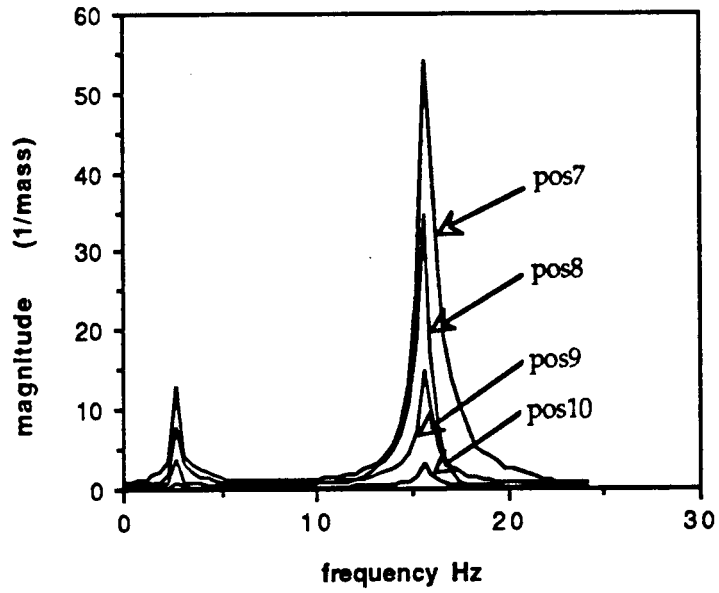


Fig 3.7a Transfer functions for pos10 through pos7

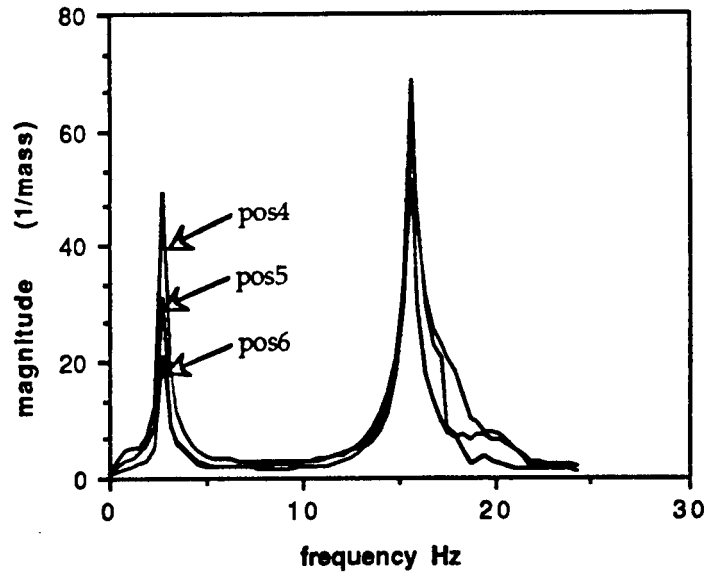


Fig. 3.7b Transfer functions for pos6 through pos4

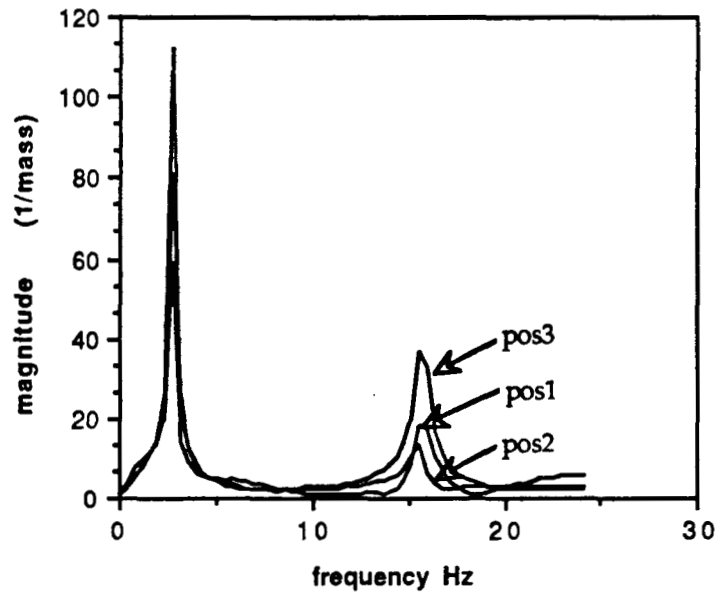


Fig. 3.7c Transfer functions for pos3 through pos1

Again one can see that the first and second bending modes for each impact point occur at identical natural frequencies, 2.34 and 15.62 Hz respectively. To assure that these averaged transfer functions were comprised of good data, the coherence functions between the eight tests at each impact position defined as

$$\gamma_{xy}^2(f) = \frac{|G_{xy}(f)|^2}{G_x(f)G_y(f)}$$

were determined. The coherence function is a measure of the contamination of two signals by noise and nonlinear effects. Thus, a value of 1 indicates a perfect linear system correlation between the two channels, while one of 0 shows no correlation. Figures 3.8a through e show the results. Although coherence is poor in some of the figures over various frequencies, all impact tests show coherences close to 1 in

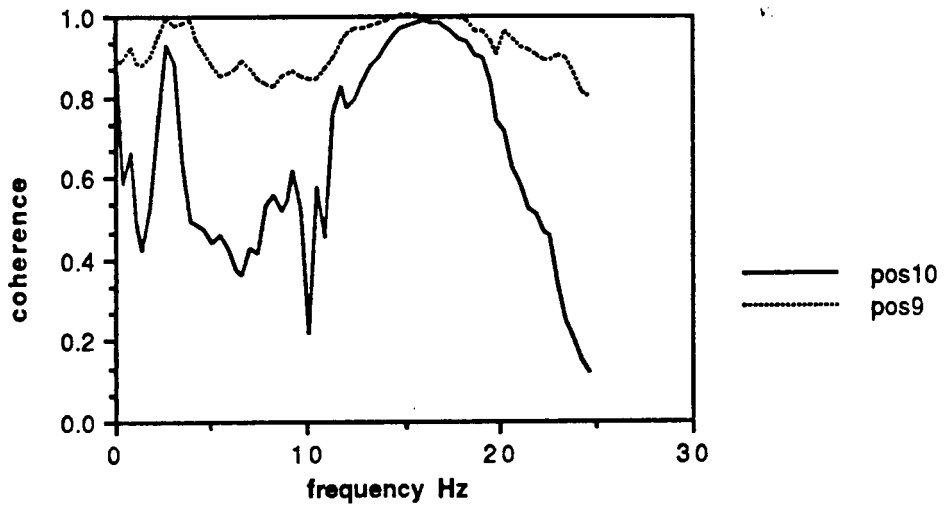


Fig. 3.8a Coherence function for pos10 and pos9

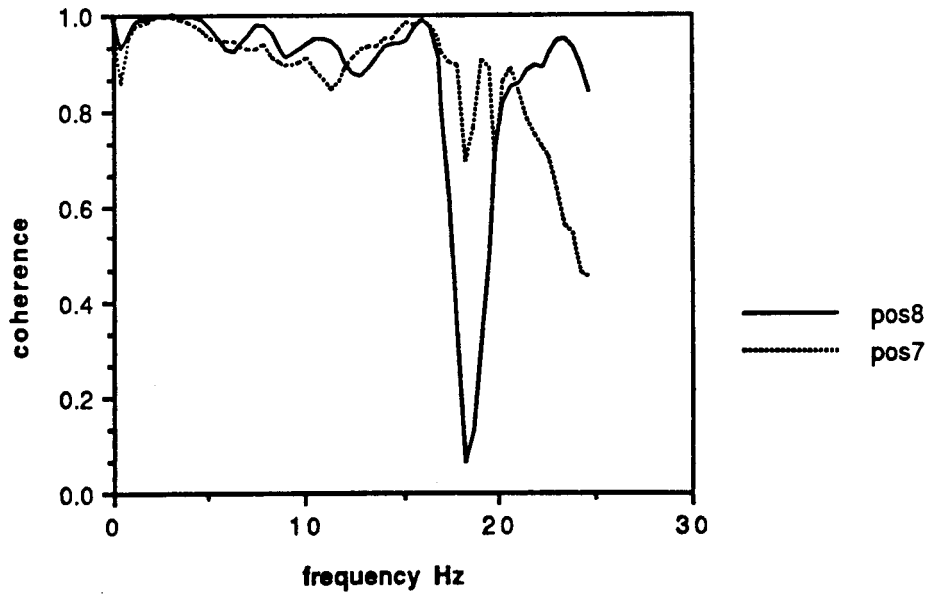


Fig. 3.8b Coherences for pos8 and pos7

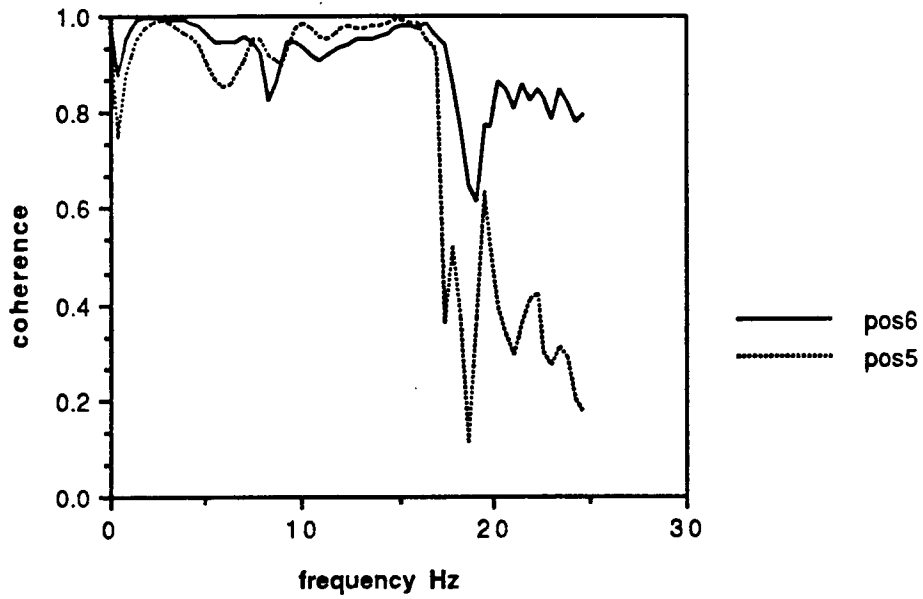


Fig. 3.8c Coherence functions for pos6 and pos5

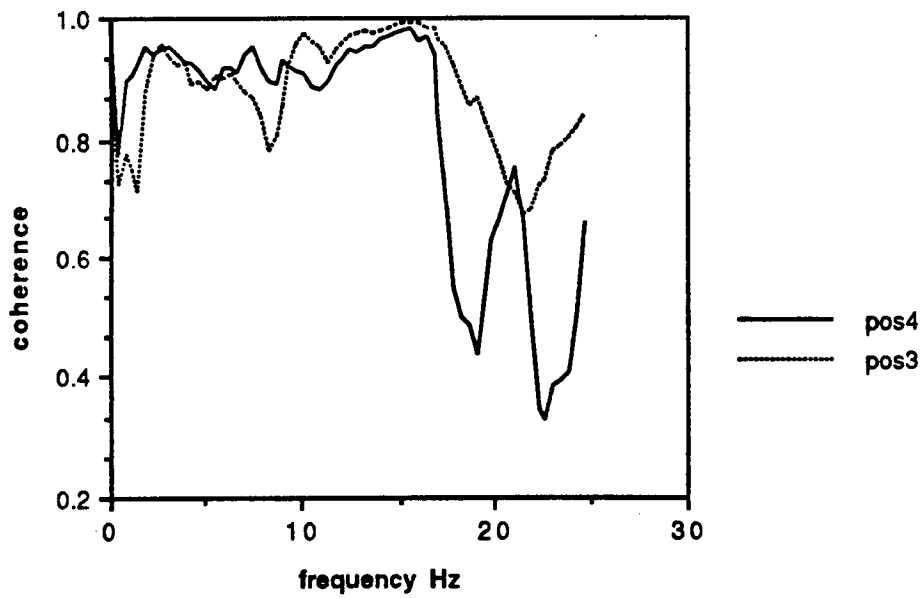


Fig. 3.8d Coherences for pos4 and pos3

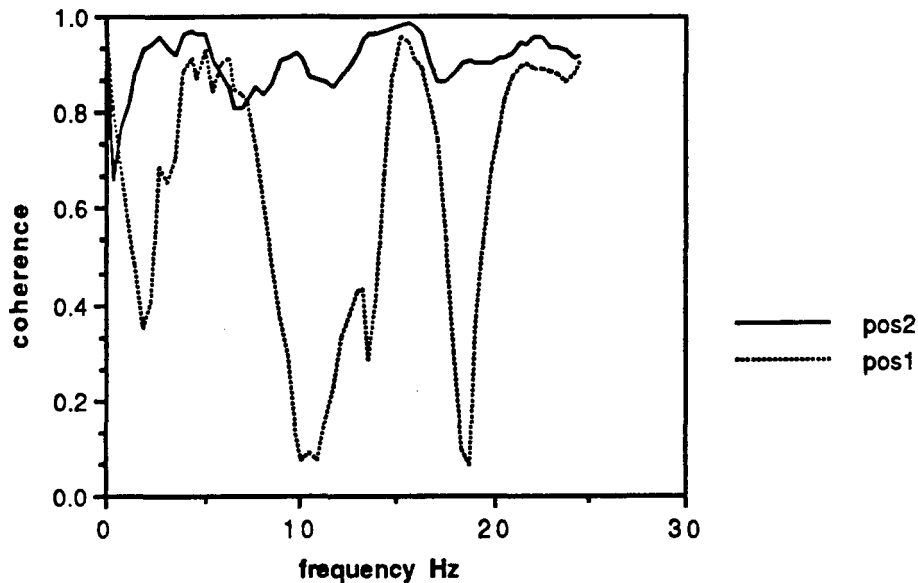


Fig. 3.8e Coherence functions for pos2 and pos1

the neighborhoods of resonant frequencies. This leads one to have a certain degree of confidence in the test data, since these points contained all the relevant information. The natural bending frequencies were already determined from this data. Next, first and second bending mode shapes were to be obtained.

The mode shape information lay in the magnitudes of the transfer functions at their resonance peaks. This was extracted and plotted versus corresponding nondimensionalized rotor blade position. Polynomials were then fit to these data to represent the mode shapes analytically. The results are shown in figure 3.9. To determine what order polynomial to fit the data with such that best presentation of the mode shapes would be obtained, an F-test was performed on the data. According to [17], when going to the next higher order polynomial, and F becomes less than 4.7 in this case, then that step up in order does not significantly improve the

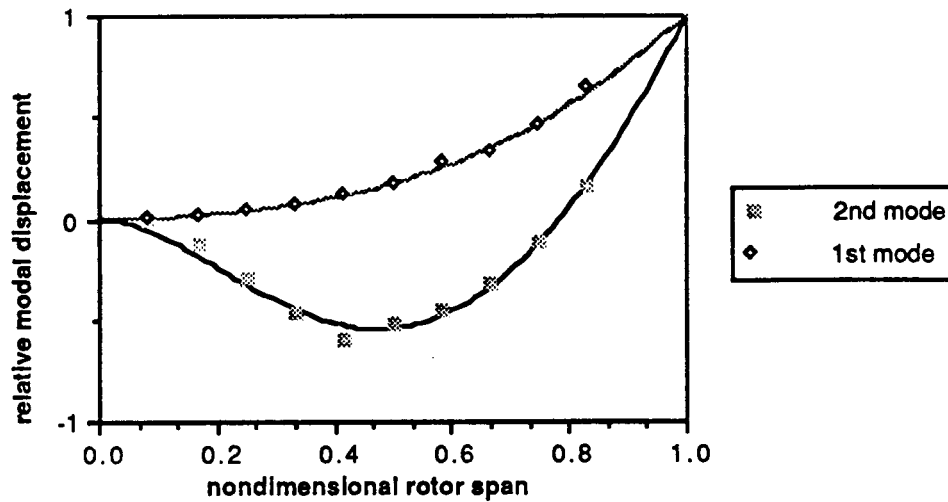


Fig. 3.9 1st and 2nd bending mode shape data with 5th-order polynomial fits

polynomial fit error. The value F is defined as:

$$F = \frac{V_{n_1} - V_{n_2}}{V_{n_2}} \times \frac{N - n_2}{n_2 - n_1}$$

$$V_{n_i} = \sum (\text{error})^2 \text{ for } n_i \text{ parameters}$$

$$n_i = \text{polynomial order} + 1$$

$$N = \text{number of data points}$$

The test revealed that for the first mode, a 3rd-order polynomial was sufficient and for the second, a 4th-order. Going to the next higher order polynomial in either case yielded F values of .15 and .06 for first and second modes, respectively (The polynomials which were eventually used, however, were of order 5, reason being that additional software for

optimally placing sensors ran into convergence problems with inputs of lower than 5th-order).

Having obtained mode shape functions, accelerometer placements along the rotor blade could now be optimized. This was accomplished by optimizing the modal matrix's condition number varying r_1 , r_2 , r_3 , and r_4 , the sensor positions. The condition number of a matrix A in a system such as

$$Ax = b$$

is defined as the ratio of largest to smallest singular value of A . It can be shown that these singular values are the positive square roots of the eigenvalues of $(A A^T)$. To obtain most reliable results from the accelerometer signals, this condition number had to be minimized [15]. Software to perform this optimization was written and utilized. Mode shape information was input into this program as 5th-order polynomial coefficients. The first and second mode shape functions as plotted in figure 3.9 were:

$$Y_{\text{mode1}}(x) = .0335 x^2 + 3.925 x^3 - 4.914 x^4 + 1.903 x^5$$

$$Y_{\text{mode2}}(x) = -11.878 x^2 + 16.261 x^3 + 2.934 x^4 - 6.360 x^5$$

The accelerometers themselves introduced a constraint in terms of their own placement in the blade. Each sensor was equipped with a temperature compensator which was located 18 inches from the sensor itself. One non-standard accelerometer, however, with its temperature compensator located 23 inches from the sensing point, was obtained. From the optimization routine, it was found that one sensor should be located as close to the blade tip as possible. Thus, this accelerometer was

planted closest to the tip. A layout of all the sensor placements resulting from the optimization routine is shown in figure 3.10.

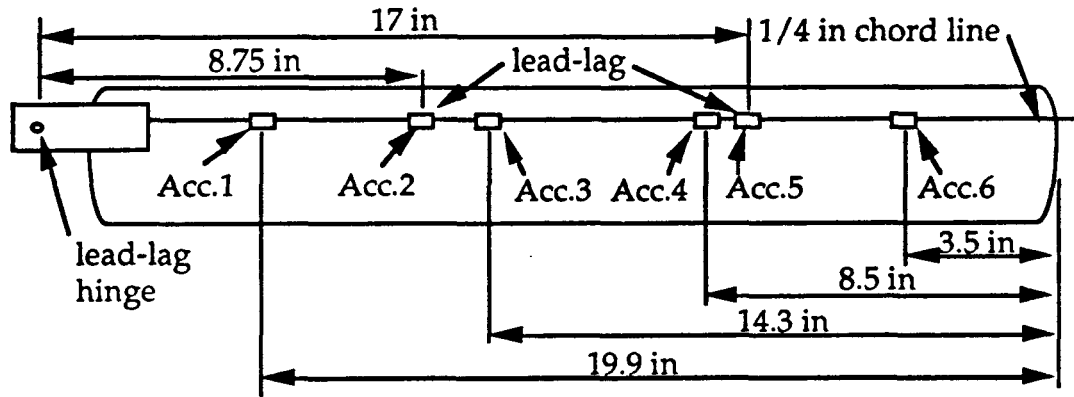


Fig. 3.10 Accelerometer position layout in a rotor blade

In addition to the four out of plane bending sensors, two lead-lag ones were also incorporated in the rotor blade. Their placement was not as vital as that of the out of plane sensors. This was due to the fact that only rigid lead-lag motion was to be detected.

Having determined where to place the miniature accelerometers to obtain best possible measurement results, the physical instrumentation stage was reached. First, a fresh blade was made and left stuck in one half of the mold. This would allow easier handling while instrumenting. The exposed half of the blade was then sanded down until only its bottom half remained. This was necessary in order to obtain a smooth finished product, as will become evident. Next, the cavities for each accelerometer as well as the channels for the wiring were cut into the blade half making sure not to puncture through the bottom surface. This surface's smoothness was to be preserved as it would be the top of the rotor blade. Each sensor was then wrapped in aluminum foil. The purpose for this was to allow easy removal from the blade if the necessity

arose. Following this, the accelerometers were carefully placed in position, facing up for out of plane and sideways for lead-lag. Since 30 wires had to come out of the mold, a small groove was milled into the other mold half at the root end. Care had to be taken in choosing which end of the blade to make the root or tip when implanting the sensors. This would determine which surface would become the top and bottom of the rotor blade. It was desirable to make the untouched surface of the blade (the surface stuck to the mold half) the low dynamic pressure surface since this was likely to be the smoother of the two. Once the sensors were in place, the mold was prepared to be shut. Half of the usual amount of liquid foam was mixed and poured over the instrumented half. The mold was shut, clamped, and left over night. When the blade was finally removed, and seams were sanded off, a smooth finished product was obtained. The specimen weighed 48 grams prompting the making of heavier non-instrumented blades to maintain rotor balance.

CHAPTER 4

Experimental procedure

4.1 Test preparation

Several tasks needed to be completed before testing could begin. The six-component strain-gauged sting balance had to be calibrated, procedures for which can be found in reference 7. To accurately identify forces and moments on the model, the 6x6 matrix relating voltage signals to the six degrees of freedom had to be constructed such that:

$$y = H x$$

where $y = [X \ L \ M \ Z \ Y \ N]^T$, x the corresponding voltage signals, and H the 6x6 calibration matrix. This was accomplished by calibrating each degree of freedom and keeping track of every input and output during this procedure. Then, taking the differenced force and moment inputs and voltage outputs,

$$y_d = (y - y_0)$$

$$x_d = (x - x_0)$$

over all samples, a least squares estimate of H was to be found by:

$$H^T = (x_d x_d^T)^{-1} x_d y_d^T$$

This procedure was done, however a small problem was encountered. After having taken calibration data for the first five degrees of freedom,

it was realized that the channel carrying the yawing moment had been switched off the entire time. Due to time constraints and data channel priorities established for these tests, it was decided to sacrifice its accuracy. However, the entire H matrix could still be constructed using calibration data from the last degree of freedom, where the yaw channel was turned on. This was accomplished as follows. In the matrix equation

$$\begin{bmatrix} y_5 \\ y_{yaw} \end{bmatrix} = \begin{bmatrix} H_{5 \times 5} & A_{5 \times 1} \\ B_{1 \times 5} & C_{1 \times 1} \end{bmatrix} \begin{bmatrix} x_5 \\ x_{yaw} \end{bmatrix}$$

B and C were determined with the last set of calibration data by:

$$[B \ C] = \left\{ \left[\begin{pmatrix} x_5 \\ x_{yaw} \end{pmatrix} (x_5 \ x_{yaw}) \right]^{-1} \begin{pmatrix} x_5 \\ x_{yaw} \end{pmatrix} y_{yaw}^T \right\}^T$$

The $H_{5 \times 5}$ matrix was determined by neglecting any yaw coupling as:

$$H_{5 \times 5} = \left\{ \left[x_5 \ x_5^T \right]^{-1} x_5 y_5^T \right\}^T$$

using data from the first five degree of freedom calibrations. Knowing, at this point, $H_{5 \times 5}$, B, and C, a least squares expression for A was determined utilizing the yaw calibration data:

$$A = \left\{ \left[(M)(M)^T \right]^{-1} (M) [y_5 - H_{5 \times 5} x_5]^T \right\}^T$$

$$\text{where } (M) = C^{-1} [y_{yaw} - B x_5]$$

Thus a complete H matrix was constructed the result being:

$$H = \begin{bmatrix} .031 & 3.34E-4 & 1.33E-4 & -2.08E-4 & 2.80E-3 & 5.75E-3 \\ 1.85E-5 & .122 & 2.61E-4 & 1.29E-3 & 5.61E-3 & .013 \\ -2.35E-3 & 7.81E-4 & .308 & -4.68E-3 & -3.59E-3 & -.023 \\ 1.88E-4 & 4.06E-5 & 1.31E-4 & .108 & -2.35E-3 & -4.21E-3 \\ -2.56E-4 & 8.76E-5 & 2.42E-3 & -3.71E-3 & .140 & .371 \\ -.323 & .507 & .103 & -.111 & -.350 & .115 \end{bmatrix}$$

How this effected the results will be discussed in chapter 5. The balance was capable of measuring forces much larger than the ones it would experience from the small model in this experiment. Thus, the gains in the commutator box were set to their maximum values, resulting in maximum sensitivity.

A fiberglass fuselage which came with the helicopter kit was added to the model. To mount the helicopter on the sting balance, an adapter had to be machined. This piece had to bolt into the model frame and attach to an already existing balance holder. The final mounting arrangement is best described by figures 4.1a and b.

Once the strain gauge balance was mounted on the carriage boom, and the model on the balance, the pitch sensors had to be calibrated. These sensors were actually potentiometers, the voltage across which was ranged between -15 and +15 volts. This provided ample sensitivity. The fact that the commutator box only accepted signals within -5 and +5 volts didn't pose a problem since only a small portion of the pots' total throw was being used. The potentiometers were easily adjusted such that pitch amplitudes between -5 and +20 degrees would produce outputs falling within that range. Using a digital inclinometer, calibration curves had already been generated prior to mounting the model. Thus, only zeros and a small set of test points for each sensor needed to be found. These would verify the calibration curve slopes and provide

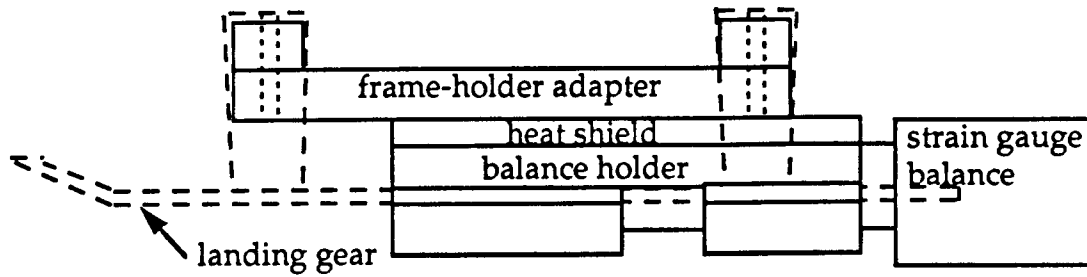


Fig. 4.1a Model-strain gauge adapter setup (sideview)

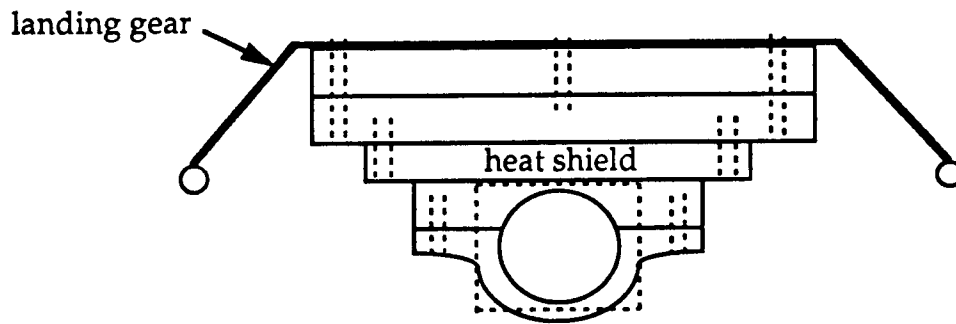


Fig. 4.1b Rearview of the adapter

reference points in case of shifts in the curves.

The digital inclinometer, which was accurate to within 0.1 degrees, served two additional purposes. First, it was used to adjust pitch links between the swashplate and pitch arms. This would assure tracking between the blades. In addition, the inclinometer was used to statically trim the rotor. In other words, the servo actuators were set such that at no control input, each blade was at zero angle of attack. Since the experiments to follow were to be open-loop, the low bandwidth actuators described earlier were satisfactory. The only necessary inputs to the model were to be random pitch commands. Thus, the easiest way to obtain them was to use a servo-compatible off-the-shelf radio control transmitter/receiver pair. This radio was equipped with trim tabs which

were set for static trim.

To transport the sensor signals from the rotor system to the nonrotating reference frame, their wire leads had to be connected to the slip ring assembly connectors. Each accelerometer had four wires, two signal and two excitation voltages. Each pitch sensor had three leads, one signal and two excitation voltages. Since the slip ring assembly was limited to only twenty channels, the excitation voltages on both the potentiometers and accelerometers were made common among each set. This resulted in nineteen channels being used. The other end of the slip ring hooked up to a 25 pin connector. A wire carried the signals from here to the data bus on the carriage. At this point, the accelerometer signals were picked up by a set of amplifier balances which provided 10 volts of excitation per unit. The pitch sensor excitations were provided by onboard power supplies. Pitch signals were then fed directly into channels 7, 8, and 9 of the PDS-700 commutator. To allow lower sampling rates by electing to skip selected data frames (see chapter 2), a longer sample period could be achieved. This, however, required the accelerometer signals to be prefiltered to smooth them out and get rid of unwanted higher frequency information. Thus, the six accelerometer outputs were first fed through a variable cutoff frequency filter box (with f_{cutoff} set at 25 Hz), before being sent to channels 10 through 15 of the commutator.

Other vital information was provided by the 1/rev pulse and the ramp function, which were sent over channels 2 and 3, respectively. The output of a tachometer, located at the top of the monorail, was fed into channel 16. This device had previously been calibrated. To obtain accurate carriage position information, a position sensor was also used. It consisted of an infrared emitter/detector pair mounted near the bottom of the carriage, facing the near wall. Reflective tape which would

trigger the sensor was attached at the same level on every support post along the track. The resulting data from this setup were pulses at exactly every ten feet of carriage travel. This signal was then scaled to TTL levels and fed into channel 17 of the PDS-700 unit.

4.2 Test procedure

With all vital sensors hooked up and ready, the data sampling stage was nearing. First, the dip switches corresponding to channels to be sampled on the buffer box were turned on. With the data acquisition system powered, as well as the card bus and sensors (carriage plugged into wall socket), the model rotor was powered up. This was achieved with a variac located in the control room. It was connected to two rails running the length of the track. As was mentioned in chapter 2, there were two sets of four rails, the lower of which used to power the carriage. The two rails for powering the model were the lower two of the upper set. This power, again, was picked up via sets of brushes. Rotor RPM was adjusted using this variac, with a digital RPM readout available in the control panel. While the rotor was spinning, each data channel was checked at the buffer box with an oscilloscope. This procedure allowed better balancing of the accelerometer signals. It also verified that all channels were in working order, and tests could begin.

First, a file of data was written before powering up the rotor. This would provide a zero for the strain gauge signals. After providing power to the rotor, and 295 RPM were reached, according to the RPM indicator, the DMA2FILE program was used to write additional data. Two samples were taken at hover with no pitch inputs. Two more sets were taken while inputting random cyclic pitch commands. The next step was to power up the carriage and do forward flight tests. Carriage power up and

operating procedures are explained in reference 7. Four data sets were written, two at flight velocities of 5 ft/sec and two at 10 ft/sec. Two additional sets were taken during transition from hover to forward flight. The forward flight tests at this point required two operators, one for carriage control on the track, and the other for data acquisition inside the control room. It is a future goal to be able to control both these processes from inside the control room.

After eleven sets of data were successfully written, the first day of sampling came to an end. The facility was powered down with the exception of the PDS-700 commutator which was to continue providing power to the sting balance (to prevent harmful moisture from accumulating on it). Results from this test are described in the following chapter.

CHAPTER 5

Results and conclusions

5.1 Resulting data and post-processing

Having made several data runs, enough results were obtained to verify the usefulness of the model and facility. Some important test conditions can be summarized as:

- 1) rotor RPM : 4.05 Hz
- 2) forward flight velocity : 5 ft/sec
- 3) advance ratio : 0.08
- 4) $\omega_1(\text{bending}) / \Omega = 1.38$
- 5) $\omega_2(\text{bending}) / \Omega = 4.80$

Figures 5.1 through 5.18 show time histories from the helicopter model and its rotor. First, a ramp signal verifies that lock of the data transmission link was maintained, yielding good data in that sense (fig. 5.1). A 1/rev clock shows rotor speed to be 4.05 Hz (fig. 5.2). Although noisy, the tachometer signal (fig. 5.3) shows approximately 5 ft/sec flight velocity. The noise on this signal due to an unknown source occurs at about 80 Hz. A possible solution to this problem may be to filter the signal before transmitting it. Figures 5.4 through 5.6 show pitch angles of each blade. It is important to note that these were input via a radio transmitter and just happened to be more negative than positive. This fact should be reflected in the measured forces and moments and actually is in figure 5.15. Here, the z-force, defined positive in the downward direction, is more positive than negative, as expected. Comparing the plots, it can be seen that the second and third blades lag

the reference blade by 1/3 and 2/3 revolutions, again as expected. Figures 5.7 through 5.10 are the out of plane accelerometer signals. For reference, the accelerometers were numbered 1 through 6, 1 being at the root and 6 at the tip as shown earlier in figure 3.10. According to this scheme, sensors number 2 and 5 corresponded to in-plane measurements. The figures show larger accelerations near the tip than the root, expressed in g's. This makes sense, as does the fact that the further outboard lead-lag sensor response is larger than the inboard one. Figures 5.13 through 5.18 show the measured forces and moments. Periodicity in each of these signals can be attributed to residual rotor unbalance. The high frequency noise which is embedded in all the signals is due to an unknown source. The roll, pitch and yaw moment responses all show oscillation about an average positive value. This is consistent with expected results. When a hingeless rotor is subjected to forward velocity, it will tilt back and right resulting in hub moments causing positive pitch and roll. Since there was no power on the tail rotor, rotor torque reactions imparted a positive yawing moment.

The accelerometer signals could now be used with a kinematic observer to estimate rotor states. Figures 5.7 through 5.12 show the raw accelerometer responses. Eventhough these signals went through a filter before being transmitted, some high frequency noise still managed to slip by, as is evident by the signals. Thus, they were filtered again using a low-pass filter with a 25 Hz break frequency. Figures 5.19 through 5.22 show the results of this step on the out of plane accelerometer outputs. Using these responses and constructing the modal sensitivity matrix as:

$$M = \begin{bmatrix} 0.743 & 0.273 & -7.294 & -4.330 \\ 6.011 & 2.526 & -11.312 & -18.057 \\ 13.931 & 7.056 & 27.904 & -12.763 \\ 20.506 & 11.810 & 79.674 & 2.259 \end{bmatrix}$$

the measurement vector $[\beta \ \dot{\beta} \ g \ \dot{g}]^T$ was determined. This was done by pre-multiplying the filtered accelerometer responses by the inverse of the modal matrix. These measurements could now be used in determining first and second bending mode position and velocity estimates. Feeding back the error between position measurements and estimates to the position and velocity estimates and integrating the acceleration measurements, the desired states were propagated. To use the position error feedback, feedback gains had to be chosen for all four states. In the case of first mode position and velocity, low enough gains needed to be used such that higher frequency information in the measurements was filtered out. Resulting gains used for these two states were 3 and 4, respectively, to set the speed of response of the observer to less than 2/rev. In the case of the second mode, this was not necessary. Here, the gains used were 30 and 10 for second mode position and velocity, respectively. Figures 5.23 and 5.24 show the first mode position and velocity estimates. The position estimates are somewhat suspect. Realistically, not much more flap position than approximately 0.2 radians was expected. Adjusting the feedback gains may yield better results. Figure 5.25 shows the actual modal acceleration measurements which were used in determining the state estimates. The second mode position and velocity estimates are shown in figures 5.26 and 5.27. The position estimates show more realistic amplitudes, not exceeding 3 degrees. Again, the second mode acceleration measurements used in determining these states are shown in figure 5.28.

Having knowledge now of β , $\dot{\beta}/\Omega$, $\ddot{\beta}/\Omega^2$, g , \dot{g}/Ω , \ddot{g}/Ω^2 , and θ , where β and g represent first and second modes, the flap equation and bending equation coefficients from

$$\ddot{\beta}(t)/\Omega^2 = -M_{\beta}(t) \beta(t) - M_{\dot{\beta}/\Omega}(t) \dot{\beta}(t)/\Omega + M_{\theta_1}(t) \theta(t) + C(t)$$

$$\ddot{g}(t)/\Omega^2 = -M_g(t) g(t) - M_{\dot{g}/\Omega}(t) \dot{g}(t)/\Omega + M_{\theta_2}(t) \theta(t) + D(t)$$

could be determined using a recursive weighted least-squares technique utilizing a UDU^T factorized error covariance matrix. This method, which is more thoroughly explained in reference 18, would yield more accurate results than a standard least squares fit. Another advantage it has over the least squares fit is that it doesn't require large data storage which makes it more realizable in application. To determine the coefficients mentioned above, they first had to be broken down into their constant and harmonic parts, since in forward flight they are not constant but periodic. Since additional terms in the flap and bending equations due to torsional effects were not modeled, additional periodic terms were added(C(t) and D(t)). Complete flap and bending equations can be found in [19]. The individual constant coefficients could then be determined using the recursive estimation method.

The non-dimensional flap spring and damping coefficients as shown in the flap equation above, were determined. Figures 5.29 and 5.30 show the resulting estimates. The spring coefficient was expected to be oscillating slightly about a value equaling the first mode frequency ratio squared, approximately 1.9. According to reference 19 the damping coefficient should be oscillating slightly about a value of approximately 0.5. The actual results, however show functions oscillating about 4.4 and 2.0, respectively (these were the values which the constant parts of the coefficients approached). This may be due to poor state estimates from the kinematic observer, or coupling effects on the measurements by torsional modes (the first torsional mode natural frequency was found in reference 11 to be approximately 40 Hz). The oscillations are also

much larger than expected. The first mode pitch forcing coefficient as shown in figure 5.31 was expected to oscillate about a value of about 0.5 according to reference 19, but didn't. In this case, the oscillations were about a value of approximately 0.1.

From bending equations in reference 19, non-dimensional second mode spring and damping coefficients were expected to oscillate about values of approximately 16 and 0.6, respectively. Figures 5.32 and 5.33, however, show disagreement with these values. The constant part of the estimated spring coefficient settled down at an unrealistic value of about -0.4 while that of the damping coefficient approached 0.003, nearly zero. Oscillations of the damping coefficient were expected to be between about ± 0.05 . Actual results oscillated at larger amplitudes. The second mode pitch forcing coefficient was expected to oscillate with an amplitude of between approximately ± 0.01 about a value of approximately 0.5 [19]. The actual results oscillate with about double that amplitude about a value close to zero, 0.004.

Although not totally obvious from the figures, almost all the constant parts of each estimated coefficient had not actually settled to constant values at the end of the estimation routine. Thus, it may be possible to increase quality of the results by simply allowing more time for the estimates to settle down.

There are a number of other possible causes for why the resulting coefficient estimates didn't agree with theory. The fact that the flap position estimates were suspect to begin with is only one. The quality of results for this state estimate could possibly be increased by using more optimal feedback gains in the kinematic observer. The same goes for the other states as well. By not modeling any pitch accelerations due to blade lead-lag in the sensor geometry, the actual measurements may become suspect. Thus, another solution to the problem may be to include that

component in the sensor geometry.

5.2 Conclusions

Having performed the tasks discussed in this paper, several conclusions may be drawn:

(1) The data acquisition system upgrade at the Princeton Rotorcraft Dynamics Laboratory has made high speed data sample rates possible as well as real-time data monitoring. These are two essentials for performing any type of high frequency active helicopter control experiments.

(2) Froude scaled model rotor blades were made yielding frequency ratios of 1.3 and 3.4 for first and second out-of-plane bending modes at $\Omega = 8$ Hz, respectively. Active control experiments in the future, however, will likely require a rotor speed of approximately 5 Hz, in order to reduce necessary sampling and actuator bandwidths. To achieve frequency ratios near 1 and 3 for the two bending modes at lower RPM, tip masses or distributed masses could be added to the existing blades. Another way to obtain the natural frequencies would be to find a new, softer material for making the blades.

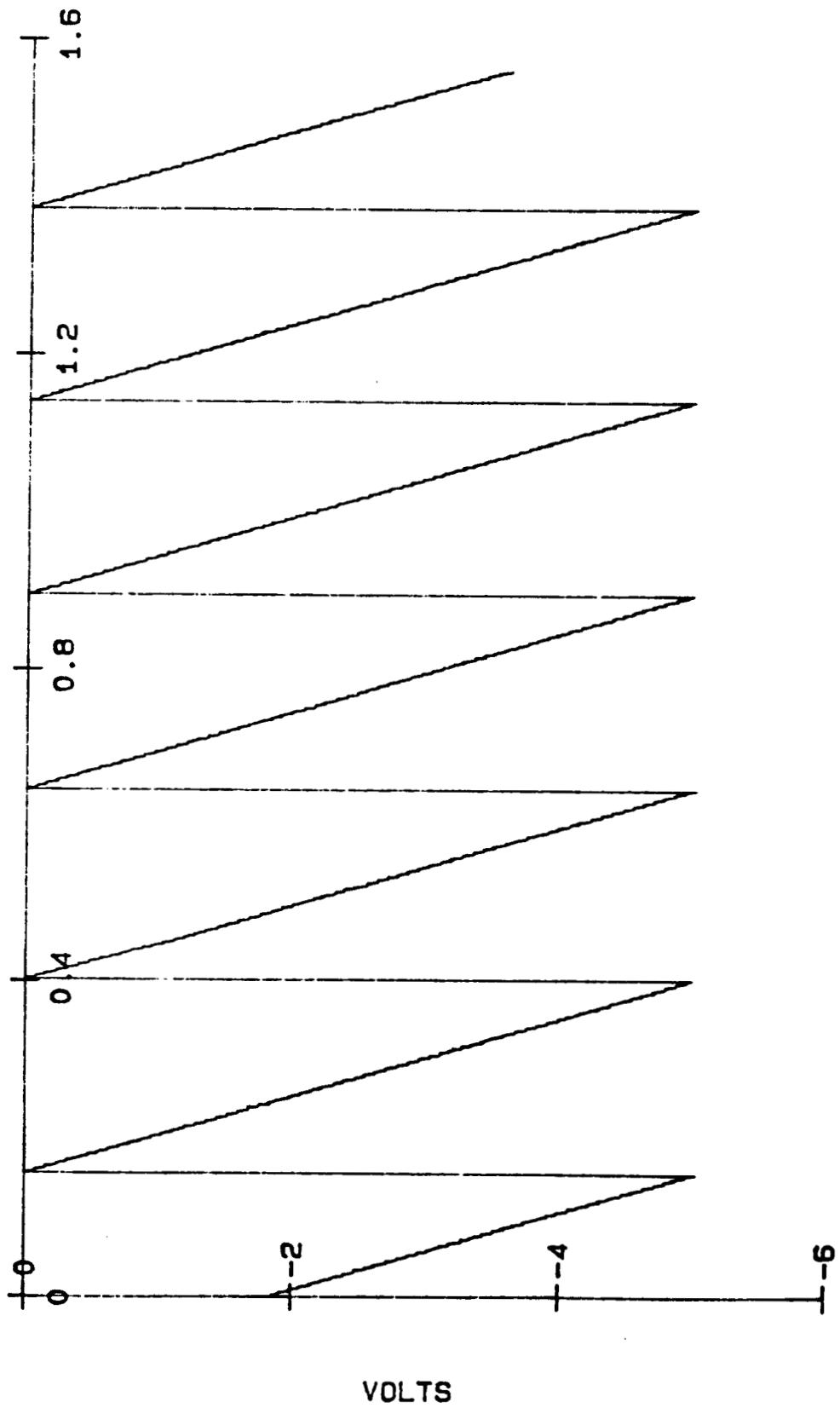
(3) Current actuators' bandwidths were too low for active control, however, they were sufficient for trimming the rotor and providing a means for introducing random pitch inputs into the model. For the rotor spinning near 5 Hz, a useful actuator will be expected to be able to input +/- 1 degrees of pitch at a minimum of 20 Hz. Thus, the search for a more capable actuator will continue.

(4) Very time- and cost-effective methods for making scaled rotor blades and constructing a helicopter test model were developed. Lack of a professional full-time staff for making the test articles forced

this kind of approach.

(5) Experimental data show that rotor states can be estimated using accelerometer mounted rotor blades. Quality of the results may possibly be improved through optimal feedback gain computations in the kinematic observer or by including pitch acceleration in the sensor geometry. Since the point of this experiment was to illustrate the data capabilities of the model rotor, lots of fine tuning can be done to the process to yield better results. These state estimates could then be used to do more accurate system identification using the procedures discussed.

FIG. 5.1 ONE PER REV RAMP SIGNAL



VOLTS

TIME (SEC)

FIG. 5.2 ONE PER REV CLOCK

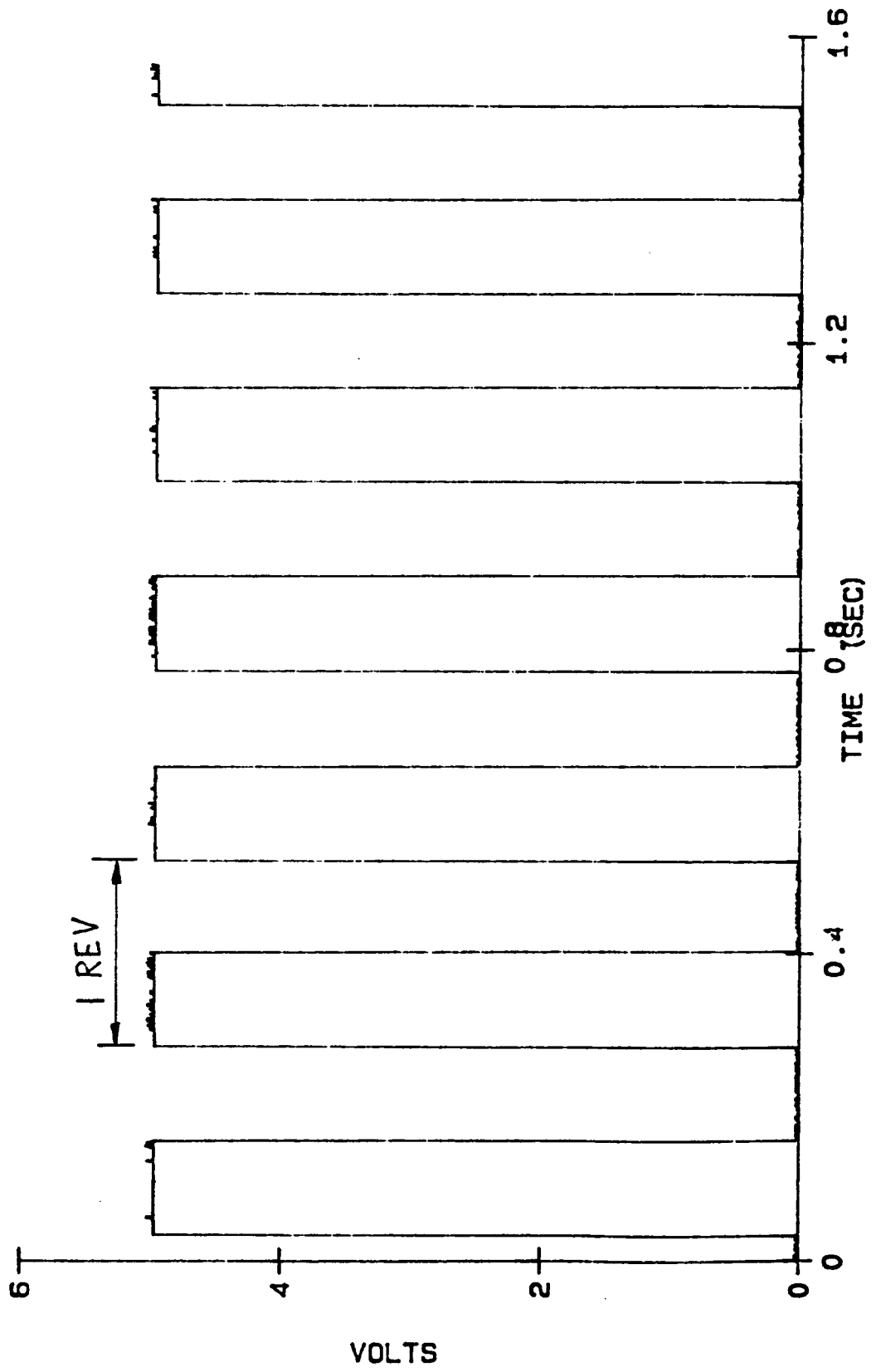


FIG. 5.3 FORWARD FLIGHT VELOCITY (TACHOMETER OUTPUT)

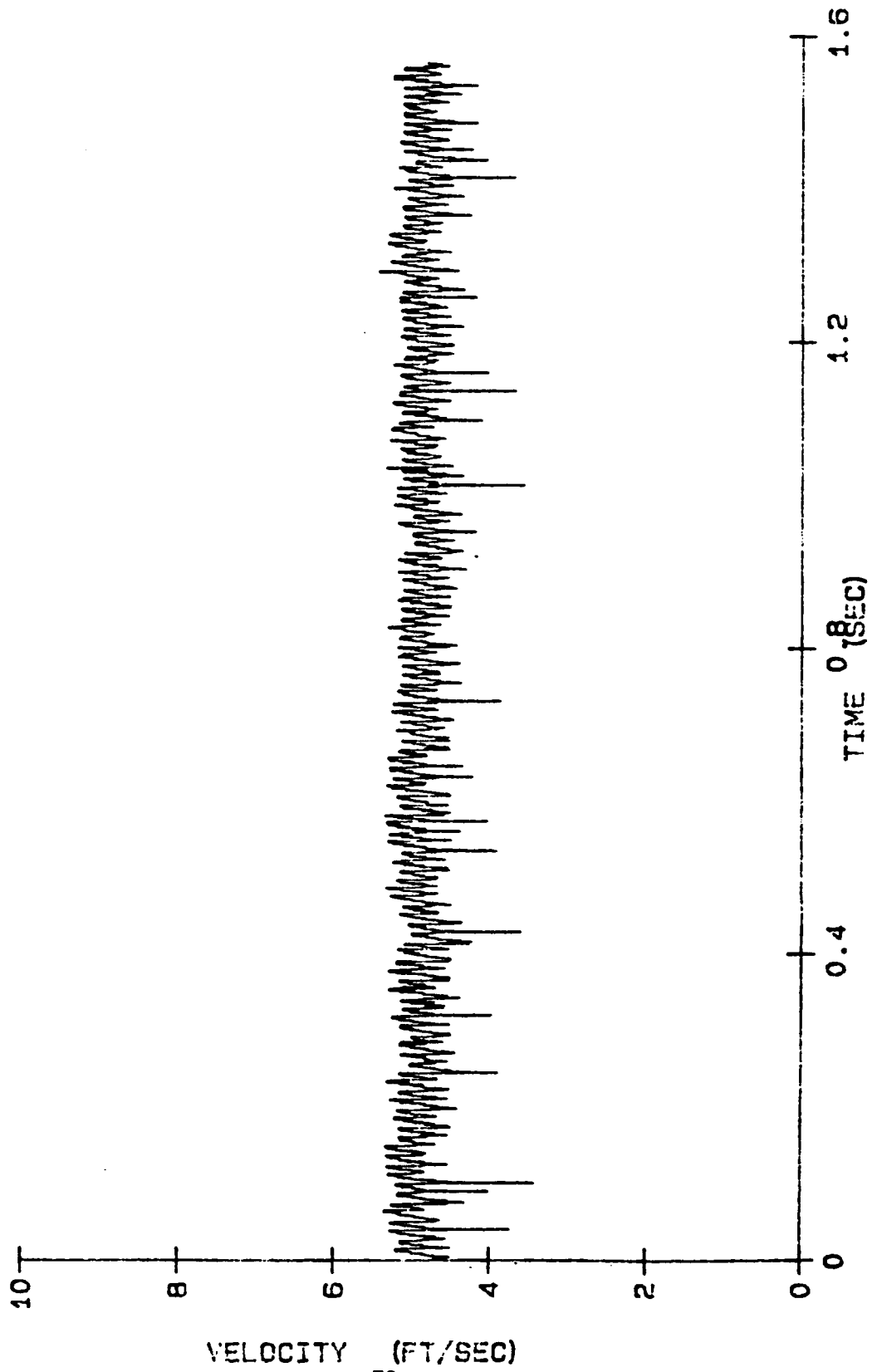


FIG. 5.4 REFERENCE BLADE PITCH ANGLE (THETA 1)

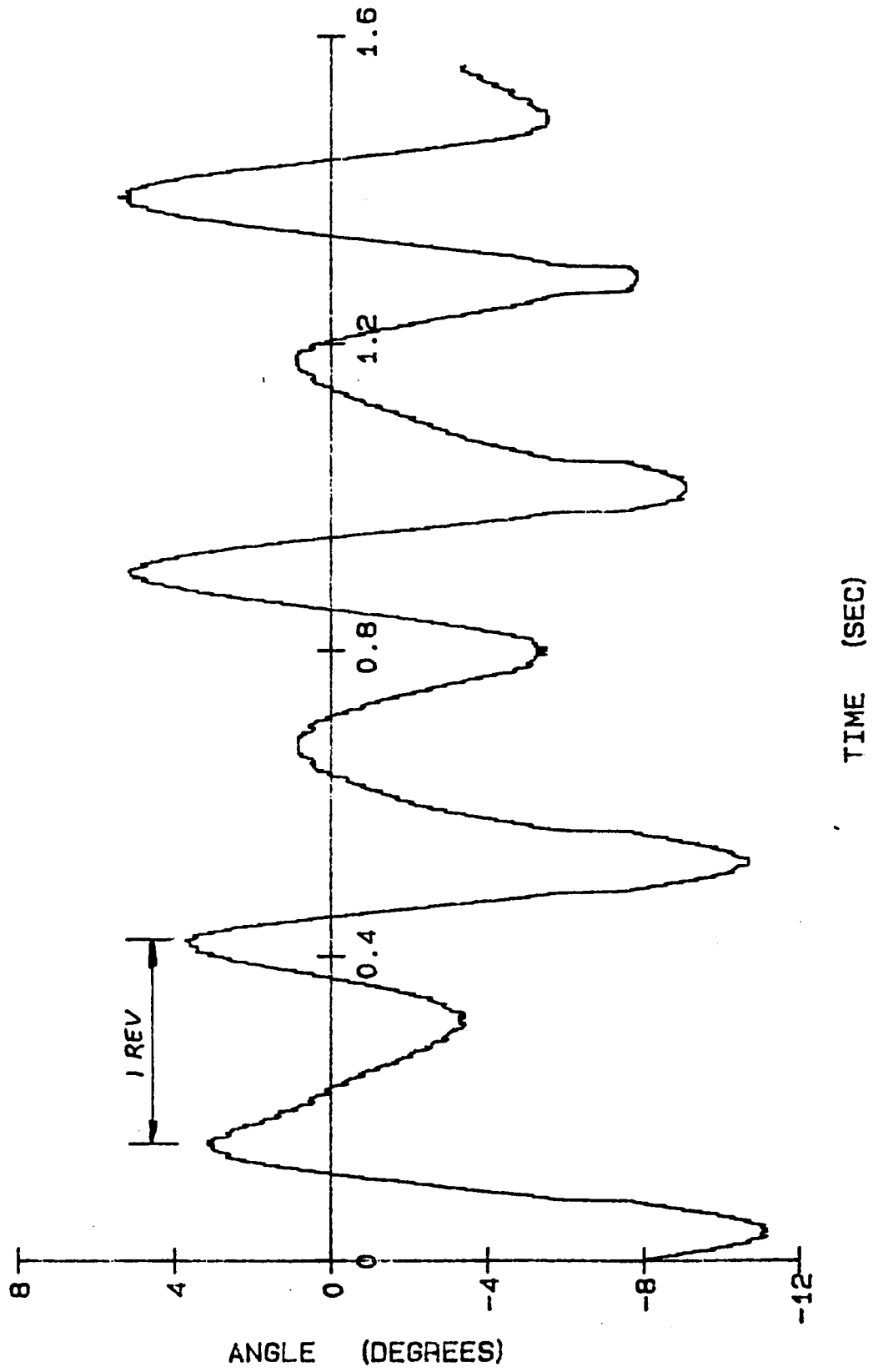


FIG. 5.5 SECOND BLADE PITCH ANGLE (THETA 2)

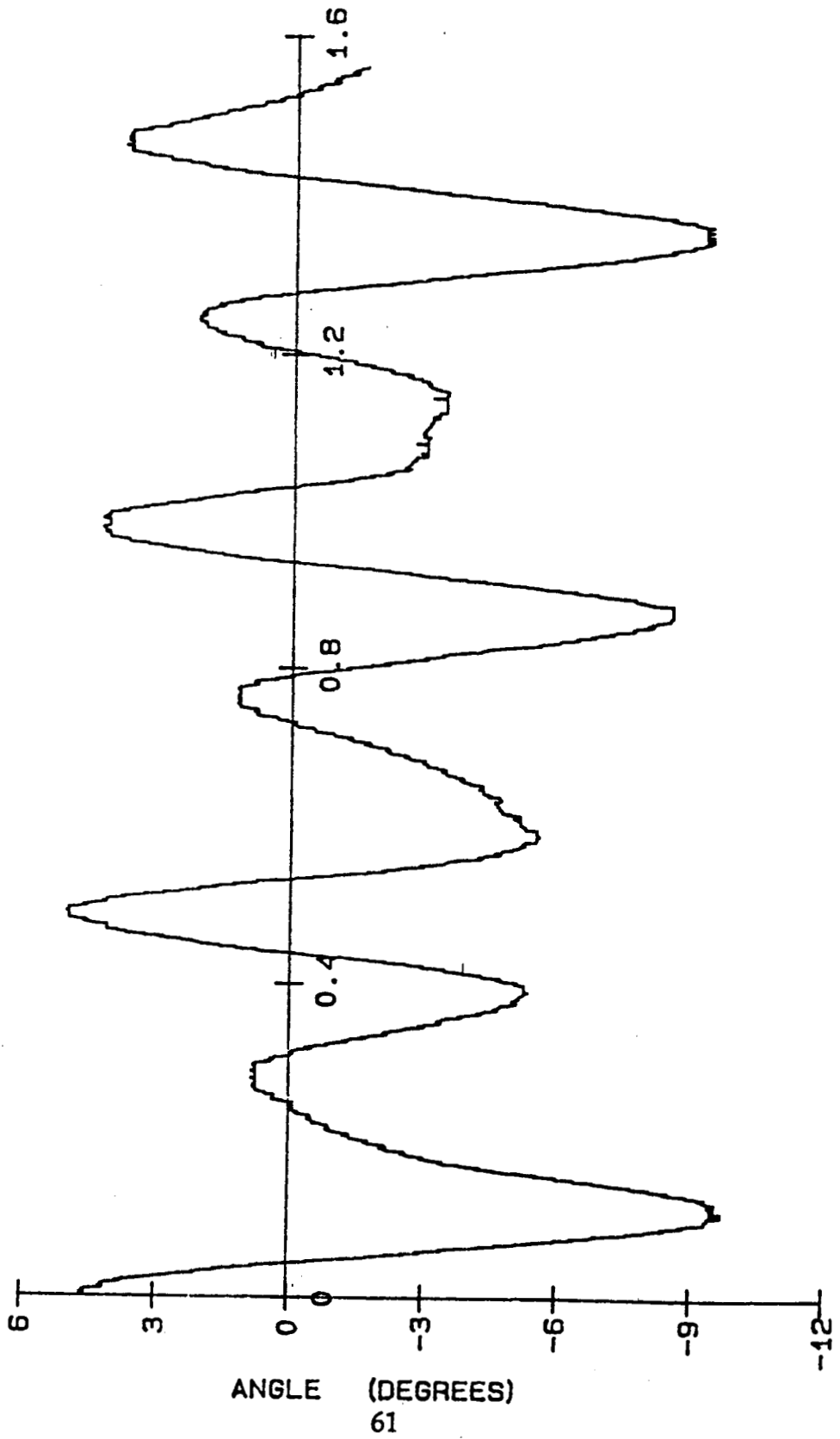


FIG. 5.6 THIRD BLADE PITCH ANGLE (THETA 3)

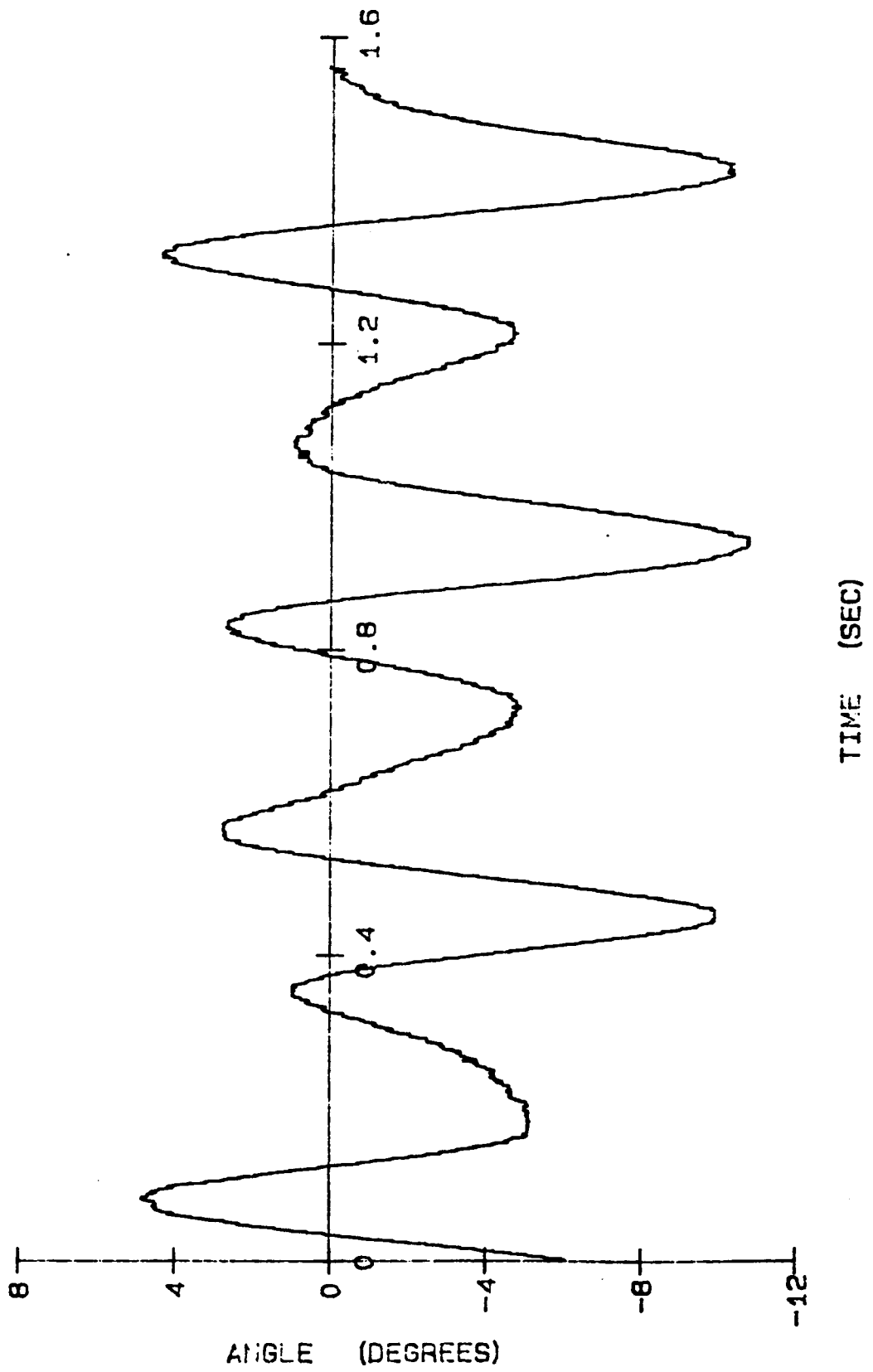


FIG. 5.7 TIP ACCELEROMETER RESPONSE (ACC. 6, OUT-OF-PLANE)

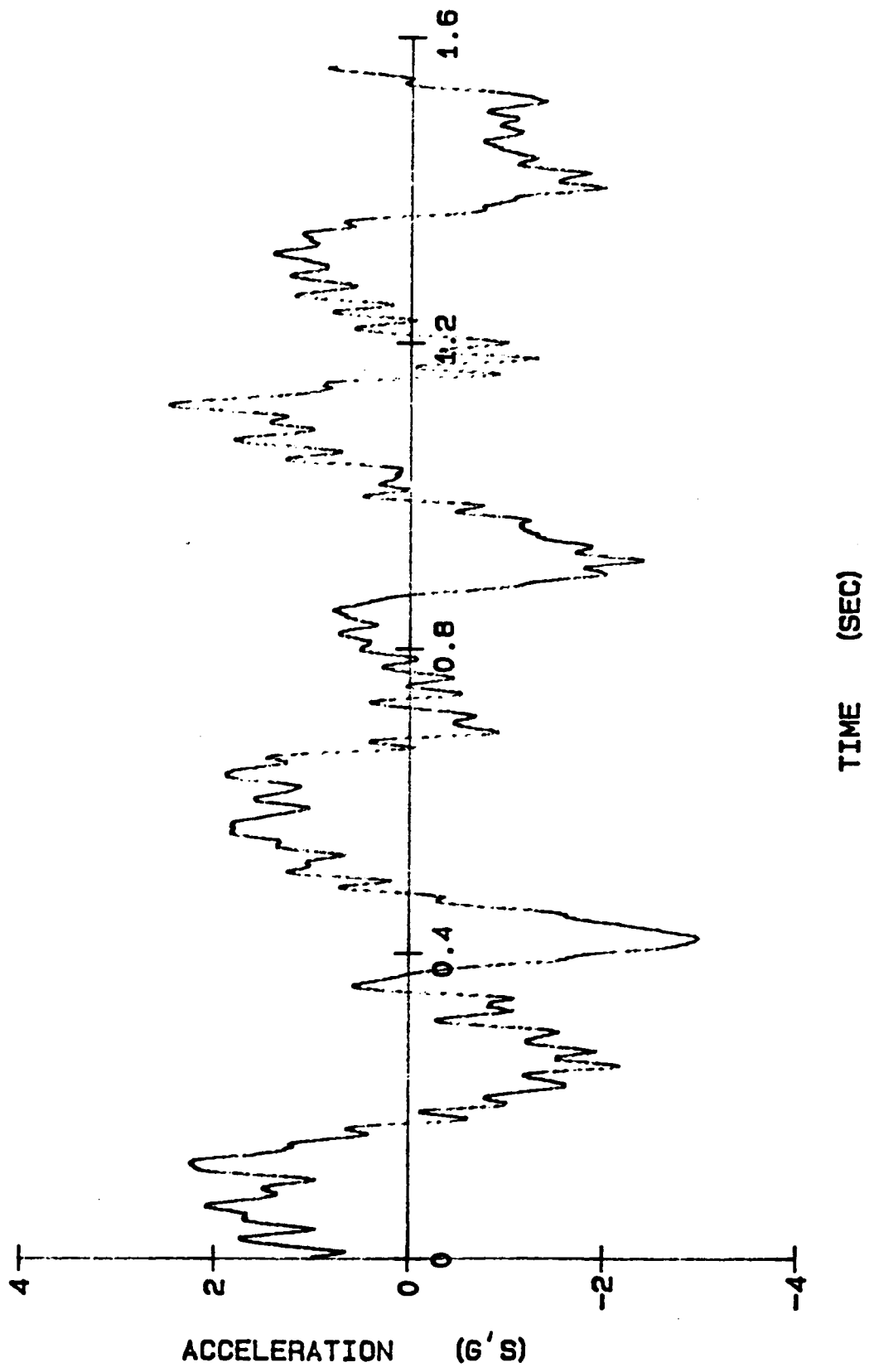


FIG. 5.8 ACCELEROMETER 4 RESPONSE (OUT-OF-PLANE)

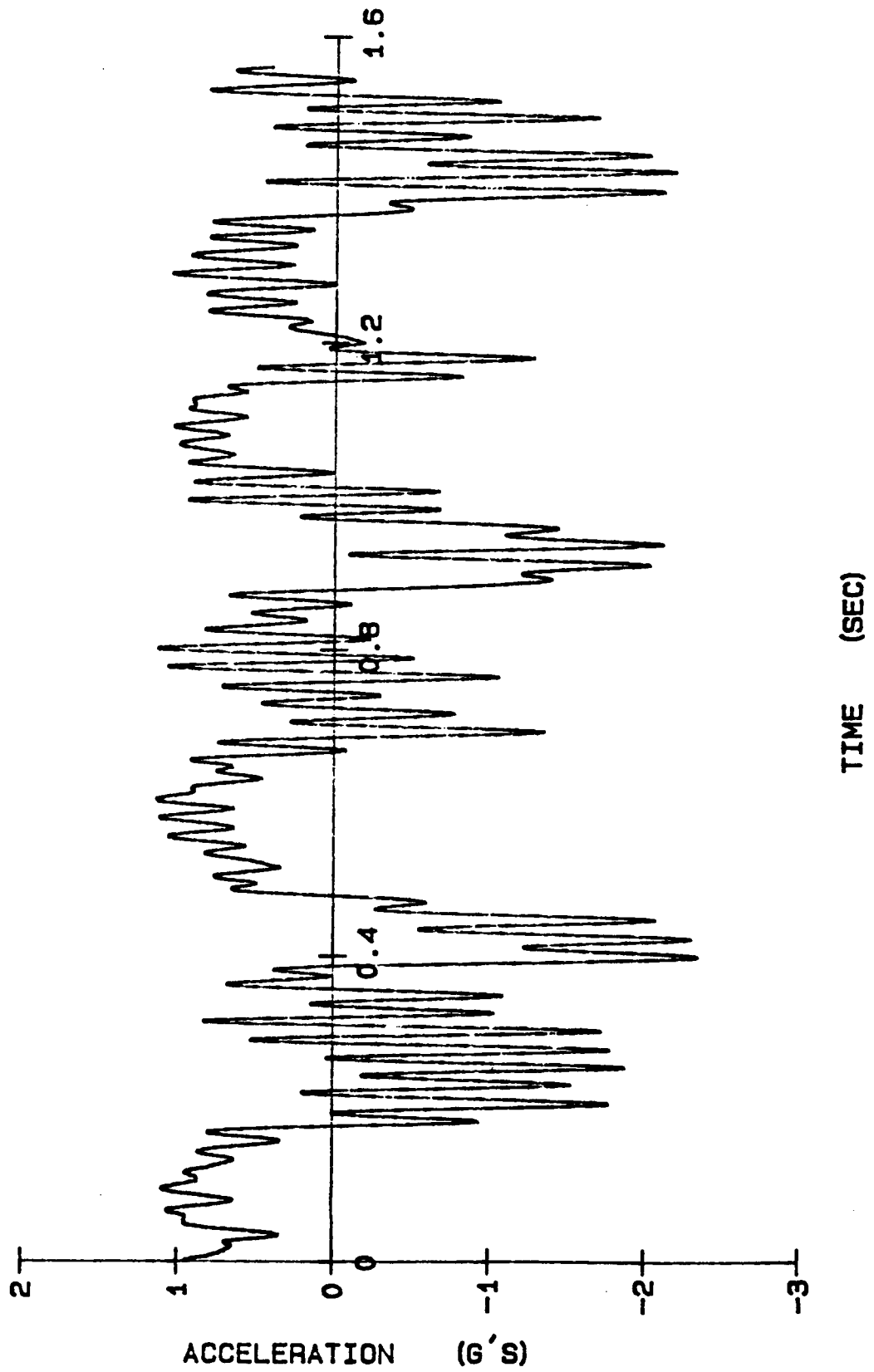


FIG. 5.9 ACCELEROMETER 3 RESPONSE (OUT-OF-PLANE)

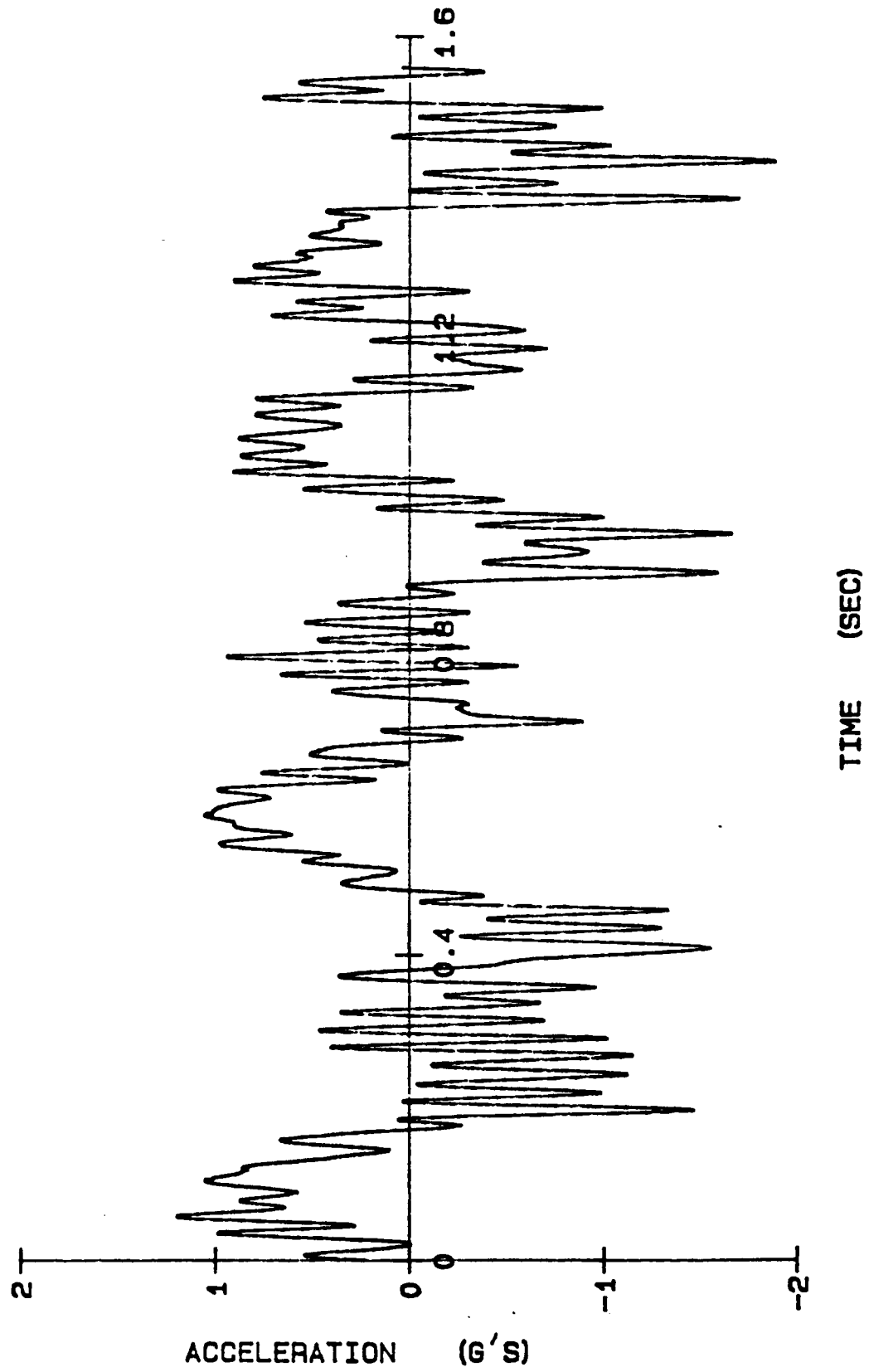


FIG. 5.10 ROOT ACCELEROMETER RESPONSE (ACC.1, OUT-OF-PLANE)

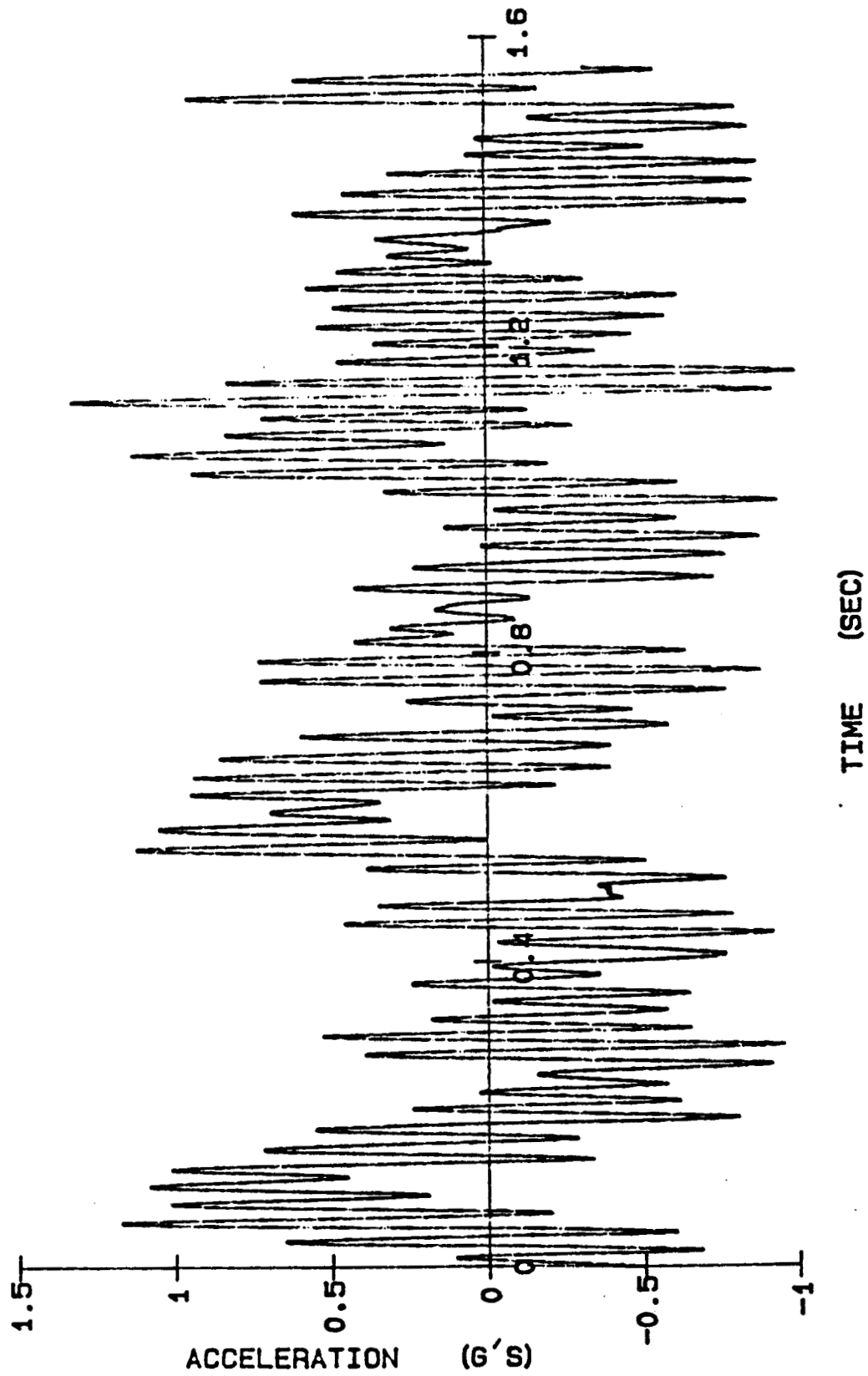


FIG. 5.11 ACCELEROMETER 5 RESPONSE (LEAD-LAG)

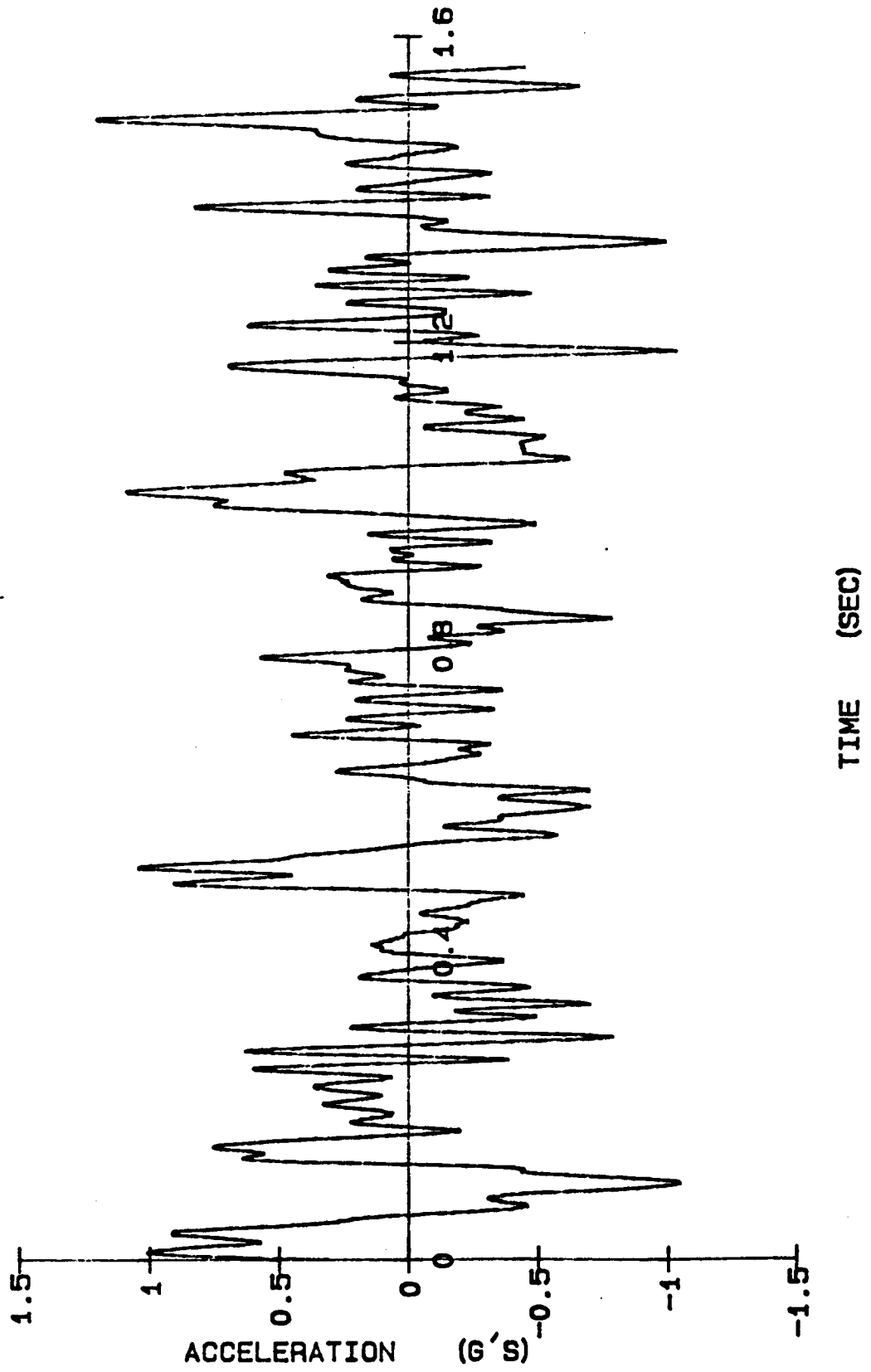


FIG. 5.12 ACCELEROMETER 2 RESPONSE (LEAD-LAG)

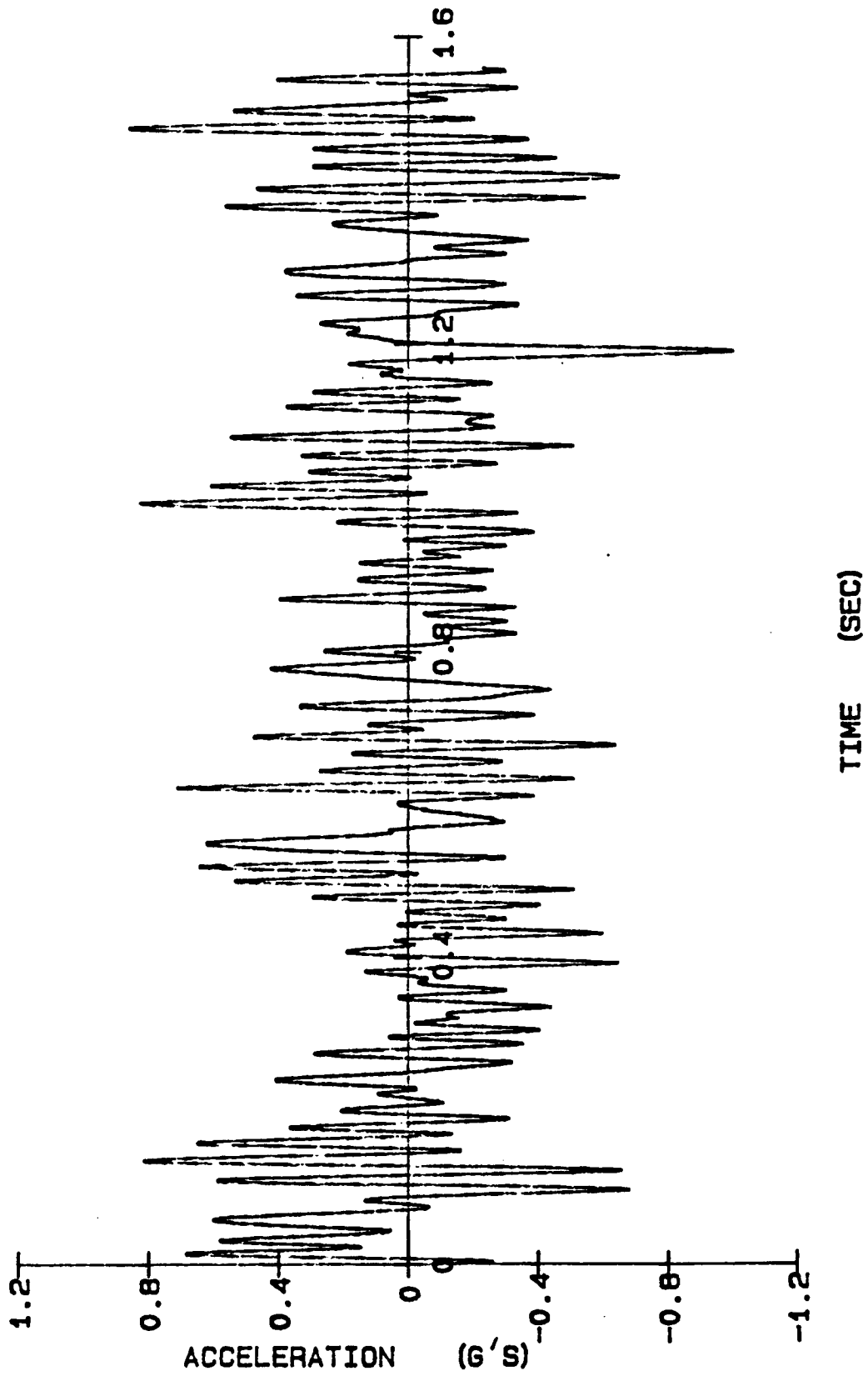


FIG. 5.13 AERODYNAMIC X-FORCE

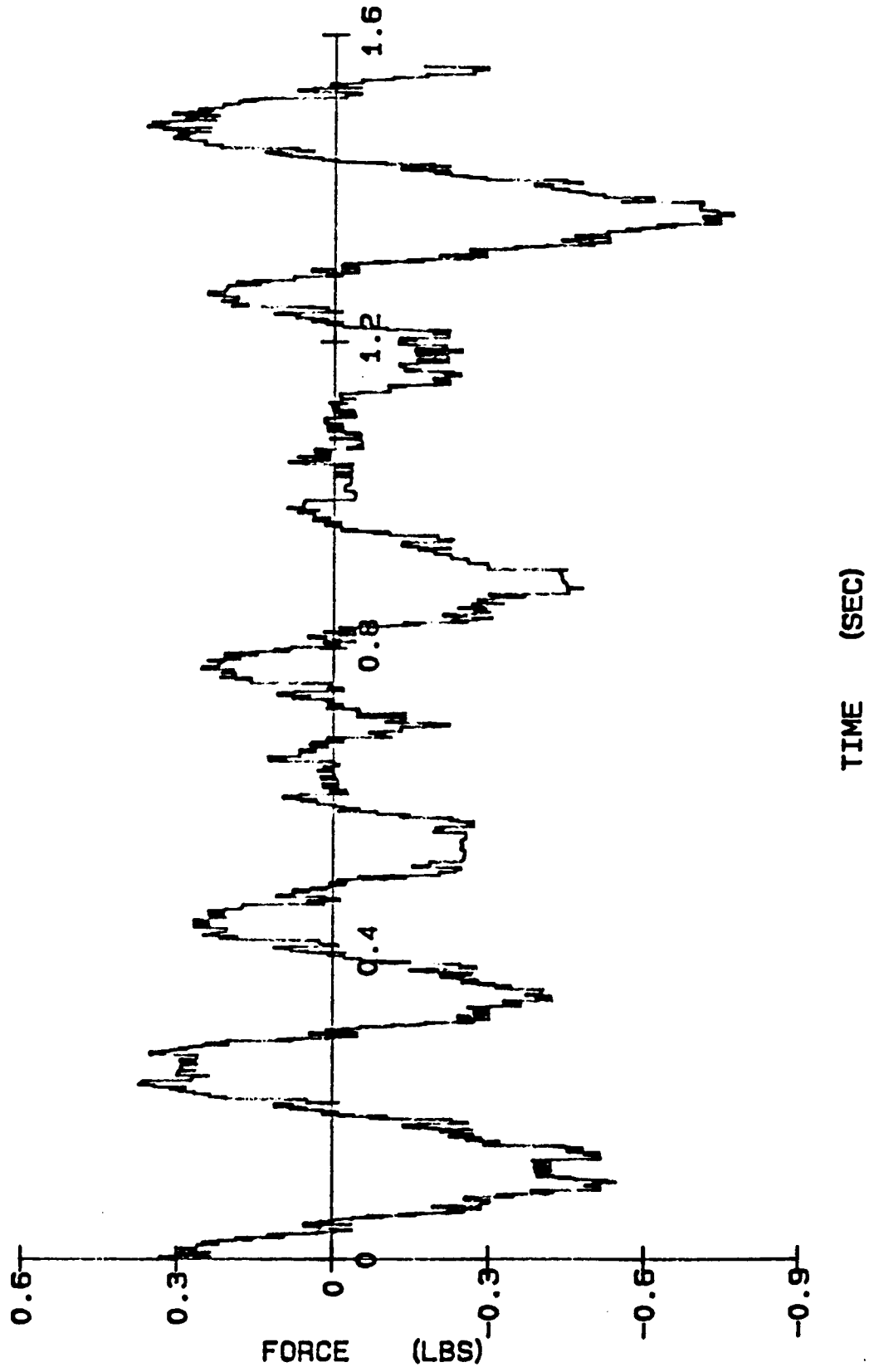


FIG. 5.14 AERODYNAMIC Y-FORCE

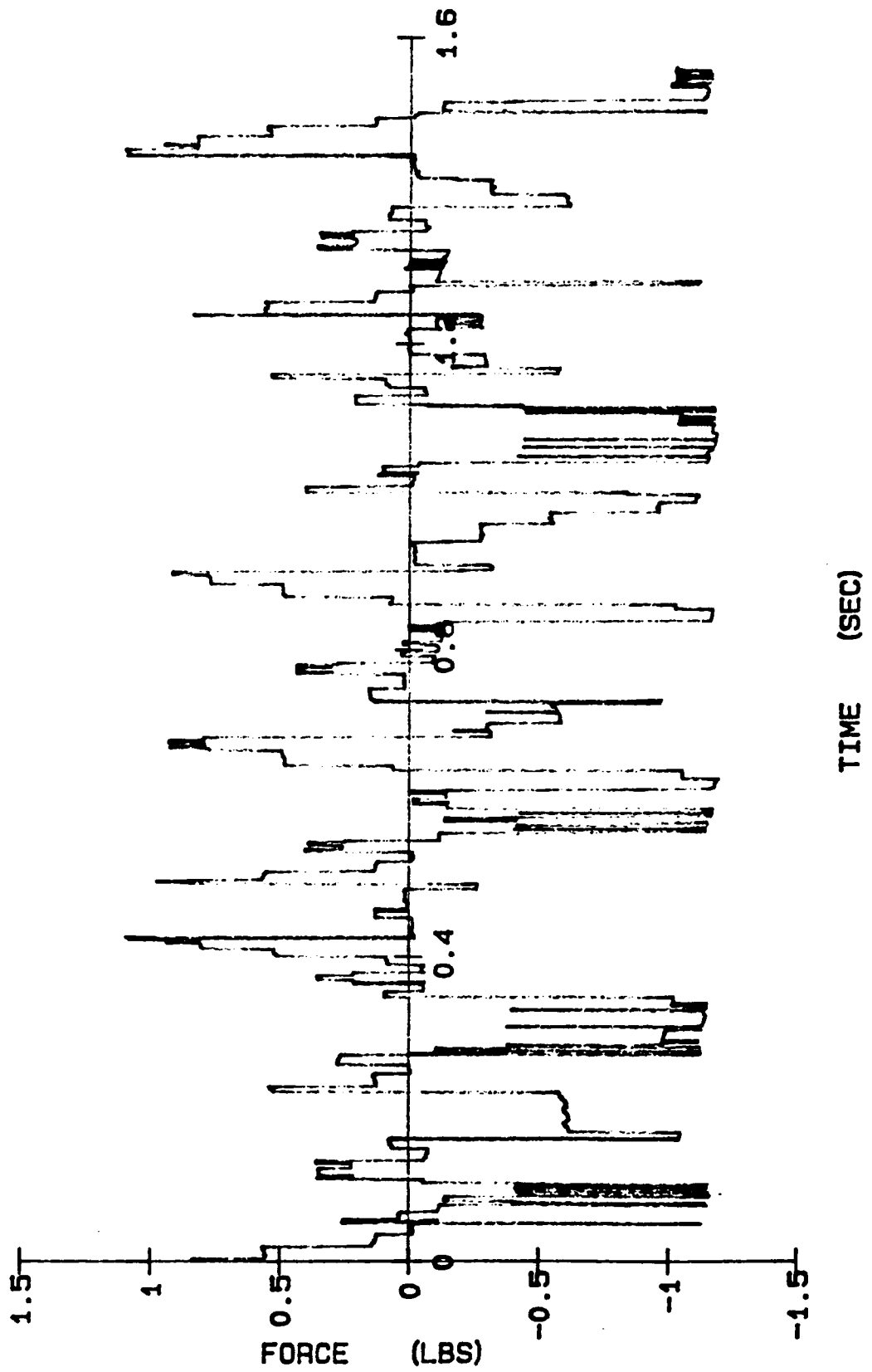


FIG. 5.15 AERODYNAMIC Z-FORCE

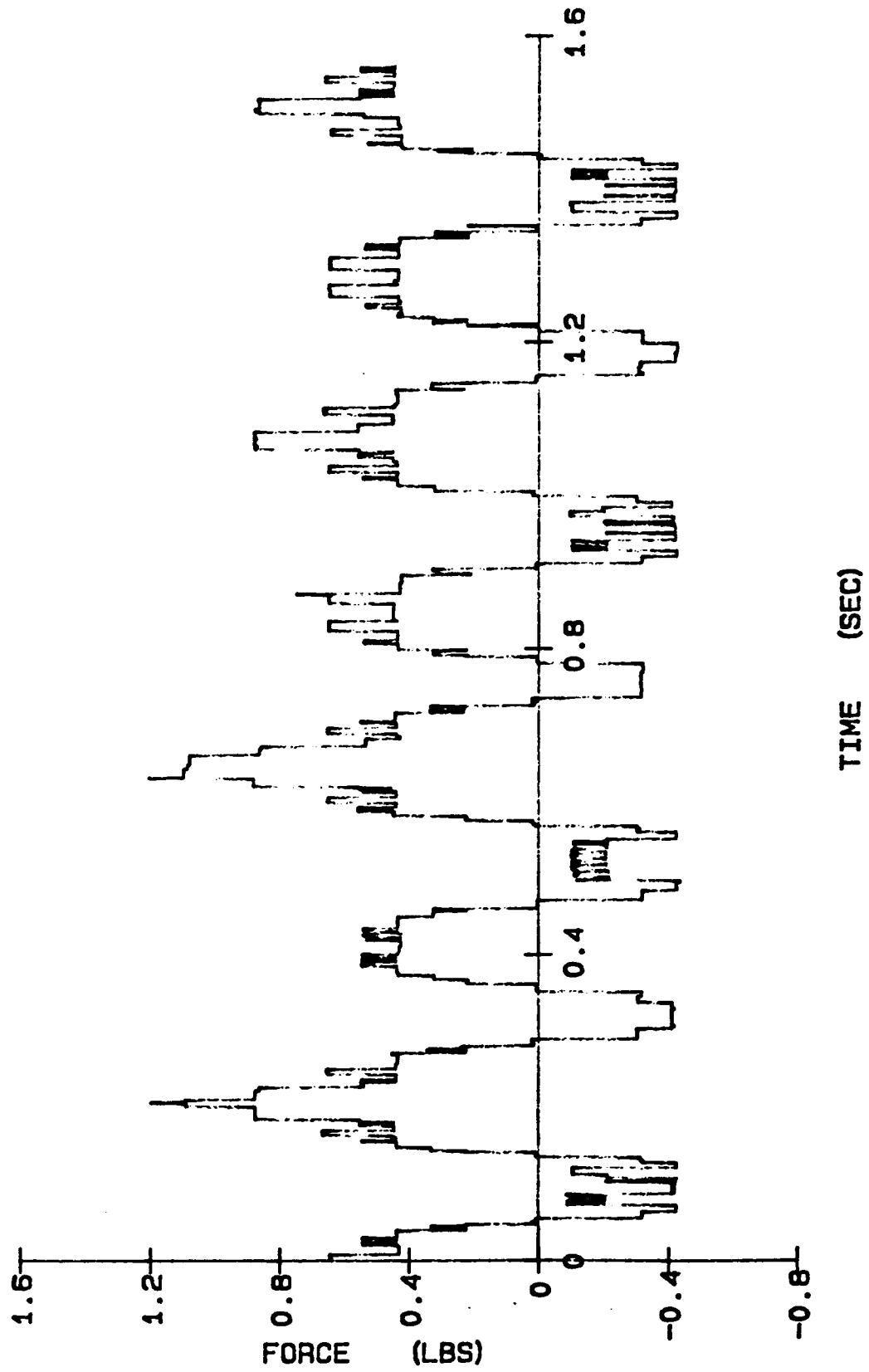


FIG. 5.16 AERODYNAMIC ROLL MOMENT

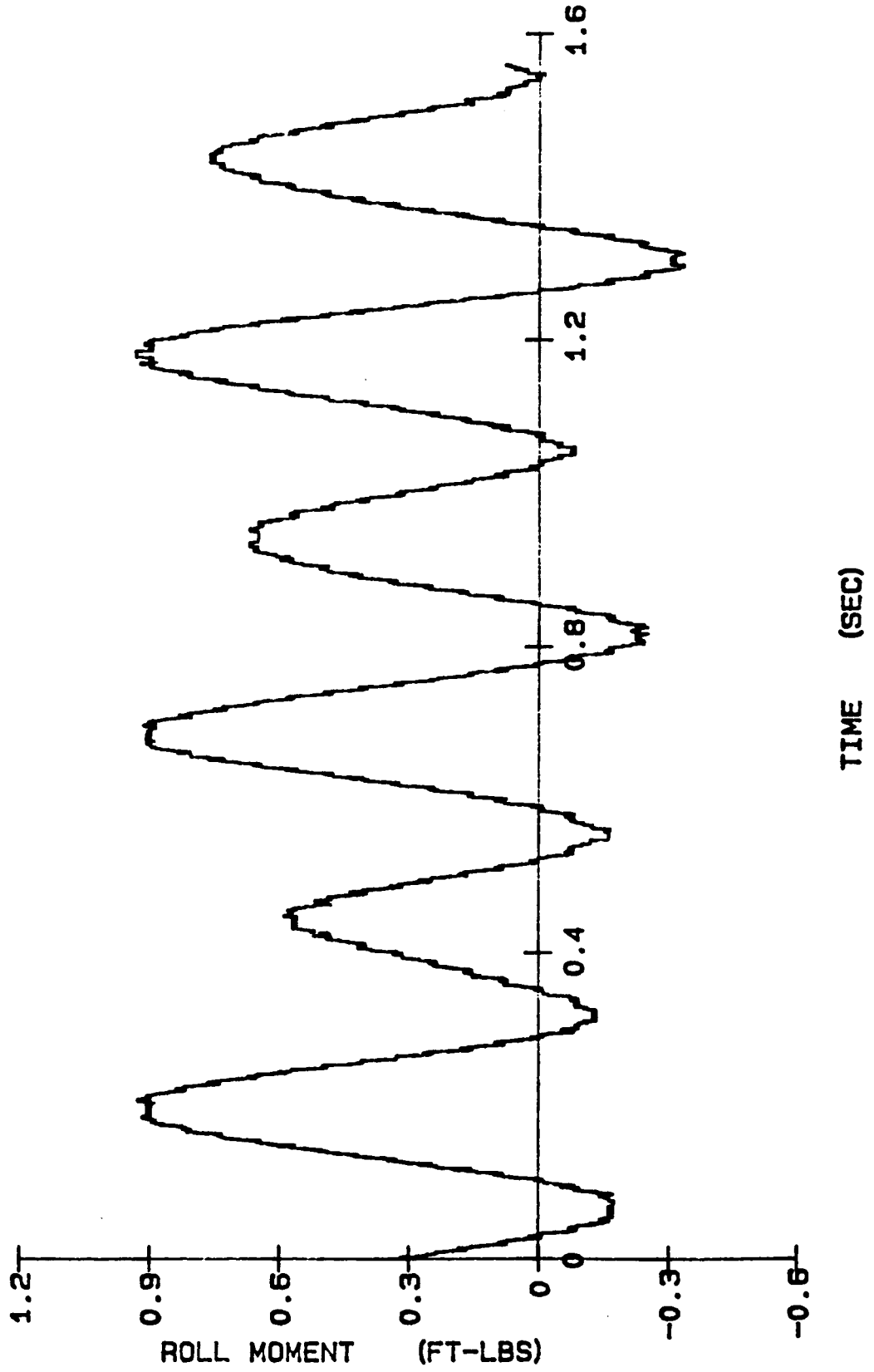


FIG. 5.17 AERODYNAMIC PITCH MOMENT

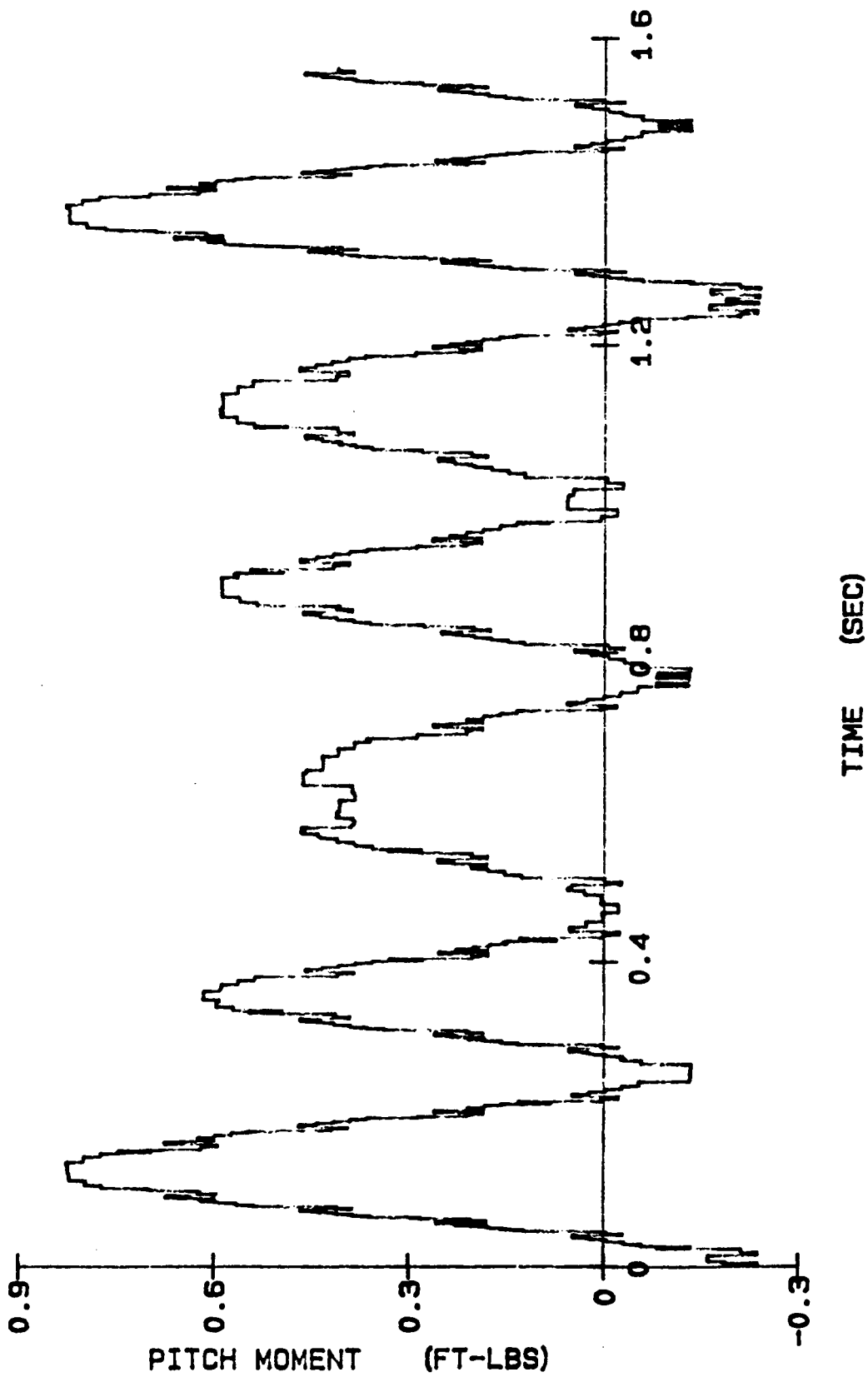


FIG. 5.18 AERODYNAMIC YAW MOMENT

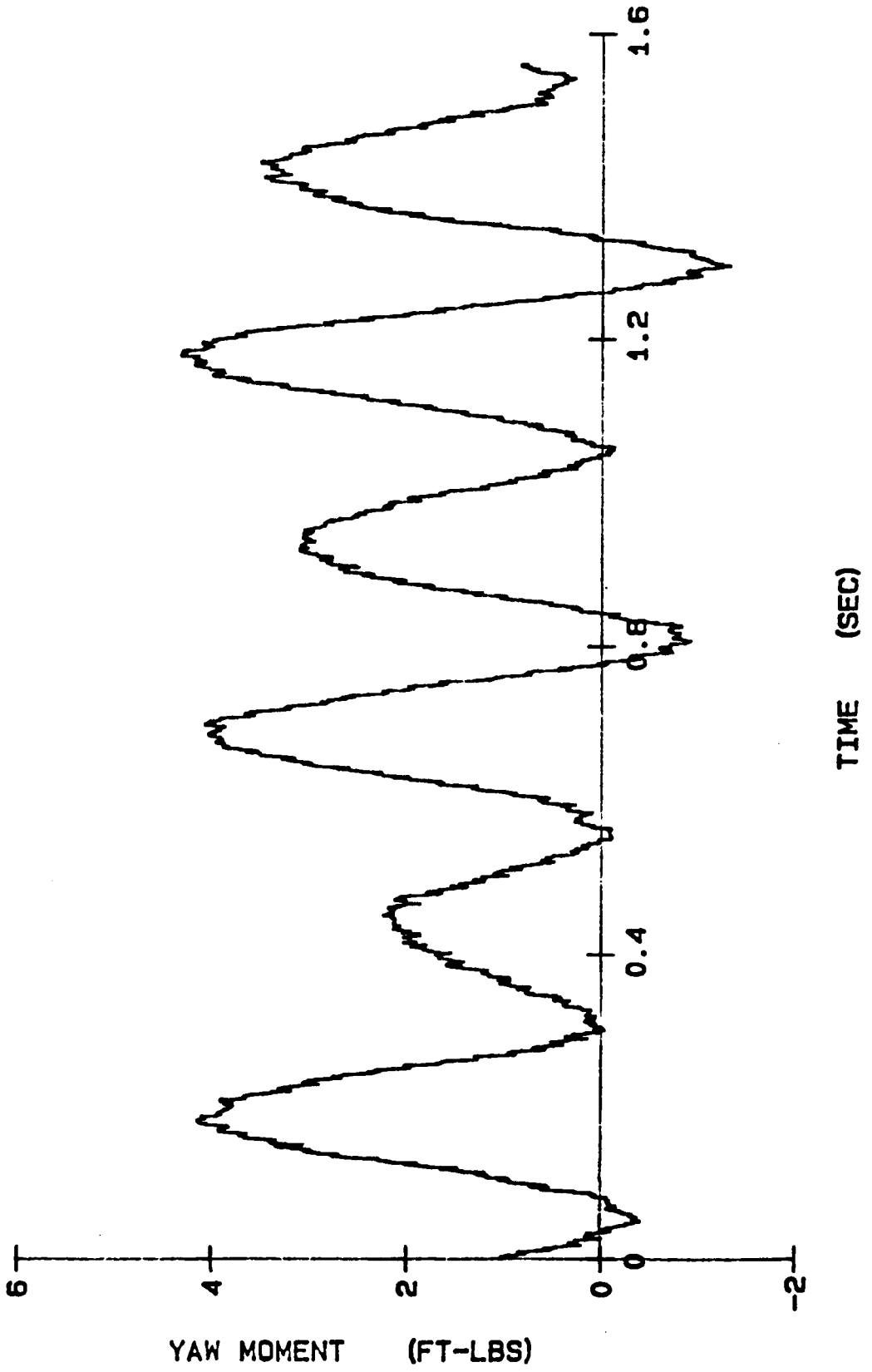


FIG. 5.19 PRE-FILTERED ACCELEROMETER OUTPUT FROM ACC.1

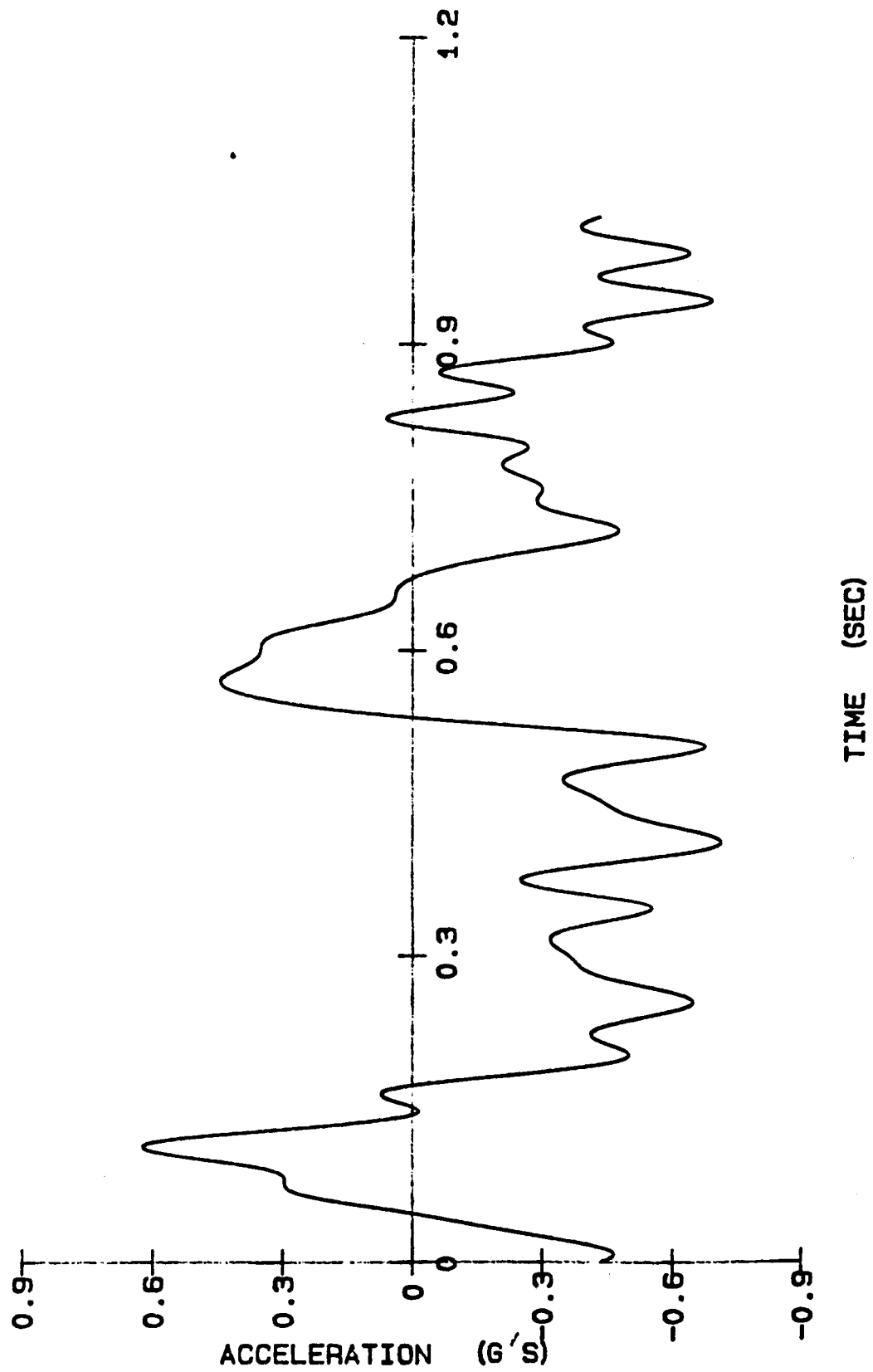


FIG. 5.20 PRE-FILTERED ACCELEROMETER OUTPUT FROM ACC.3

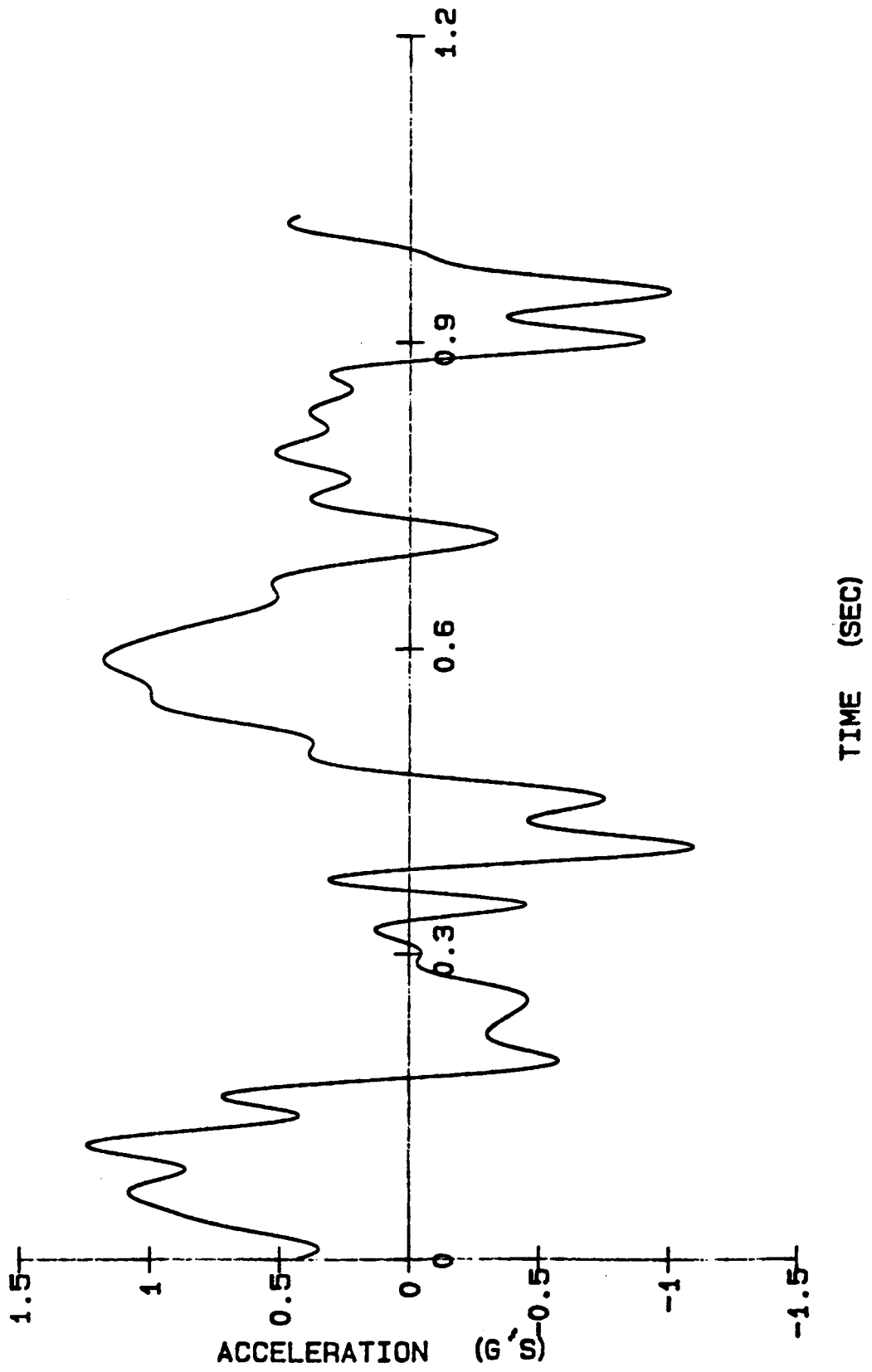


FIG. 5.21 PRE-FILTERED ACCELEROMETER OUTPUT FROM ACC.4

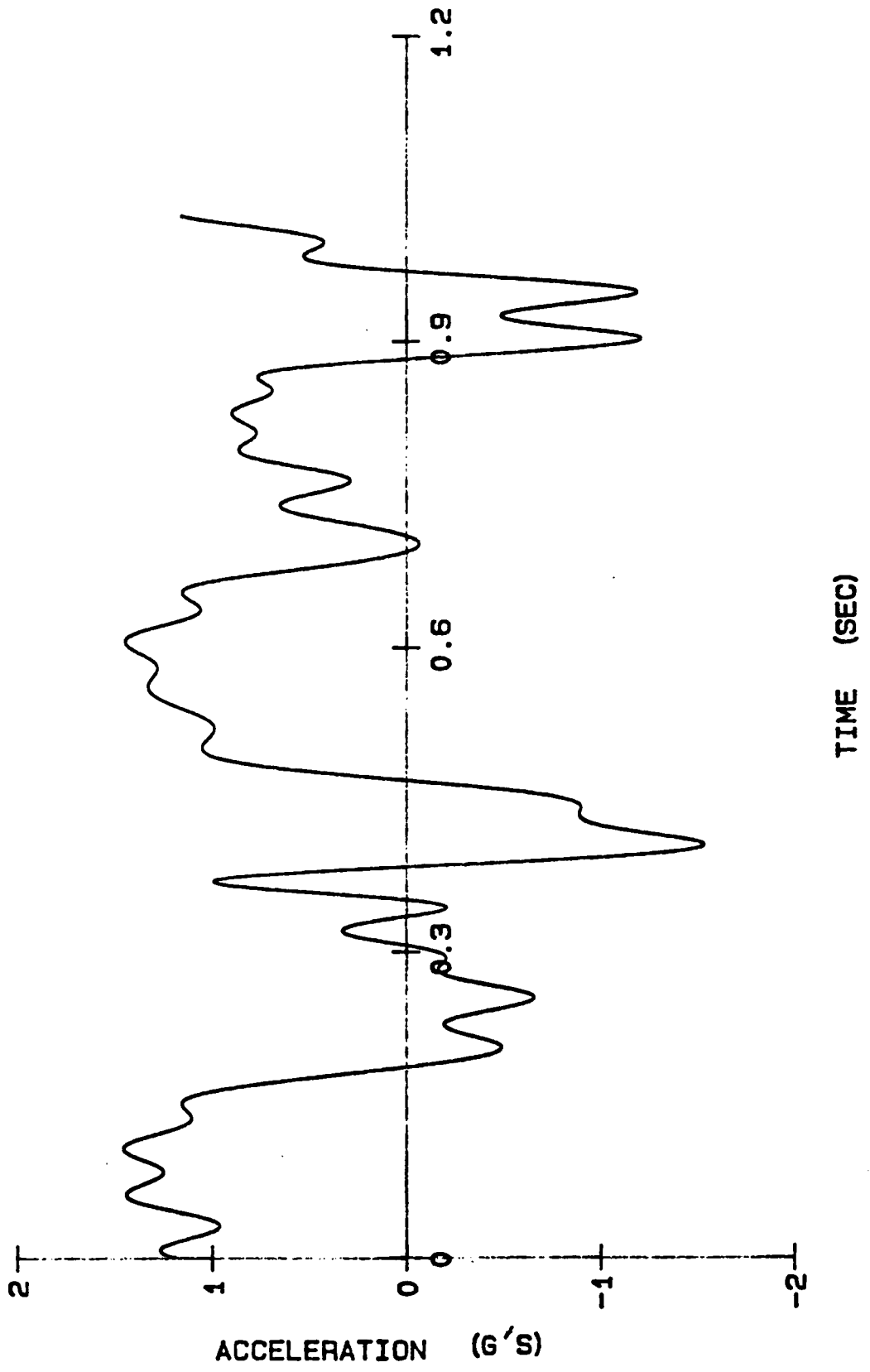


FIG. 5.22 PRE-FILTERED ACCELEROMETER OUTPUT FROM ACC.6

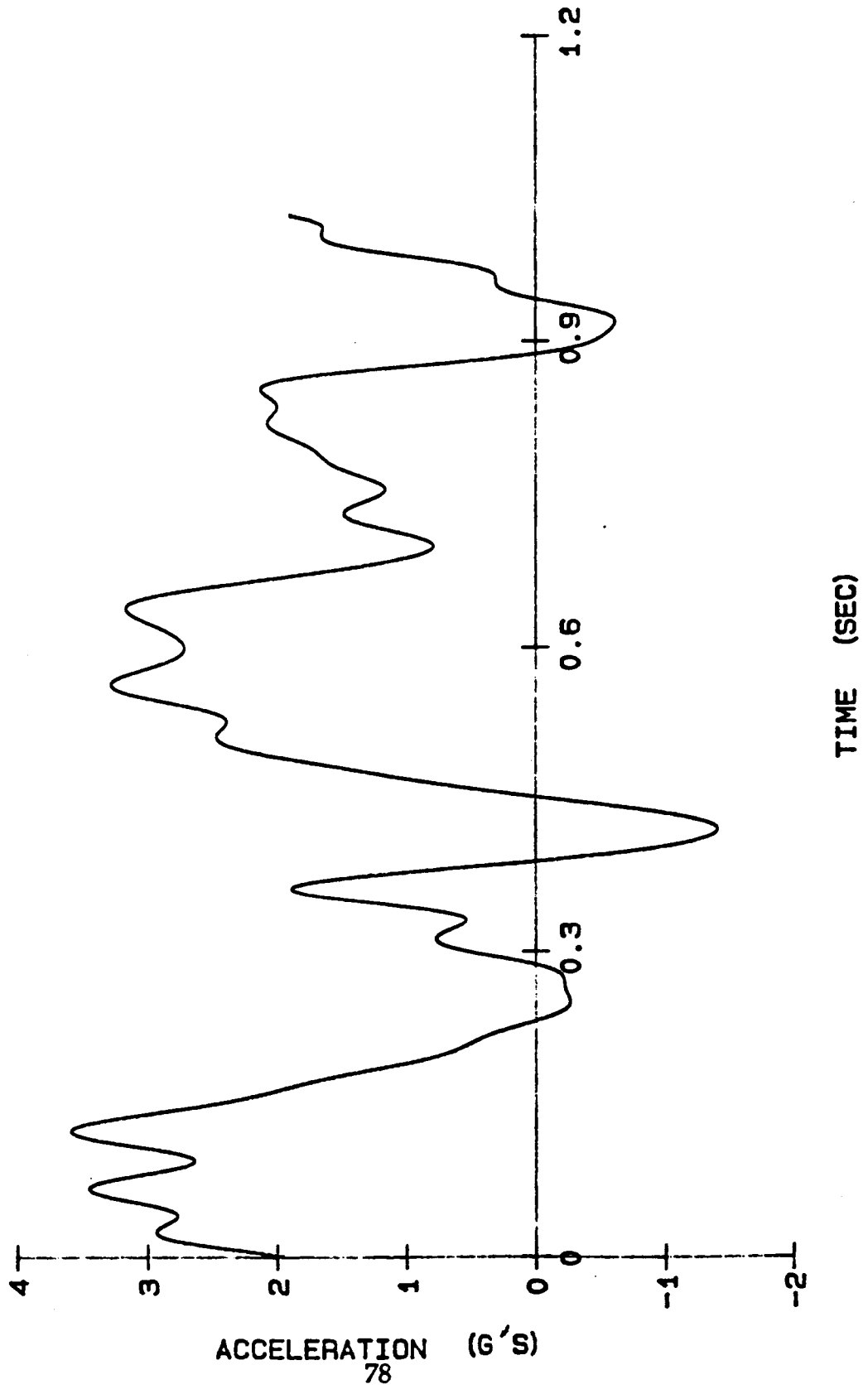


FIG. 5.23 ESTIMATED FIRST MODE DISPLACEMENT

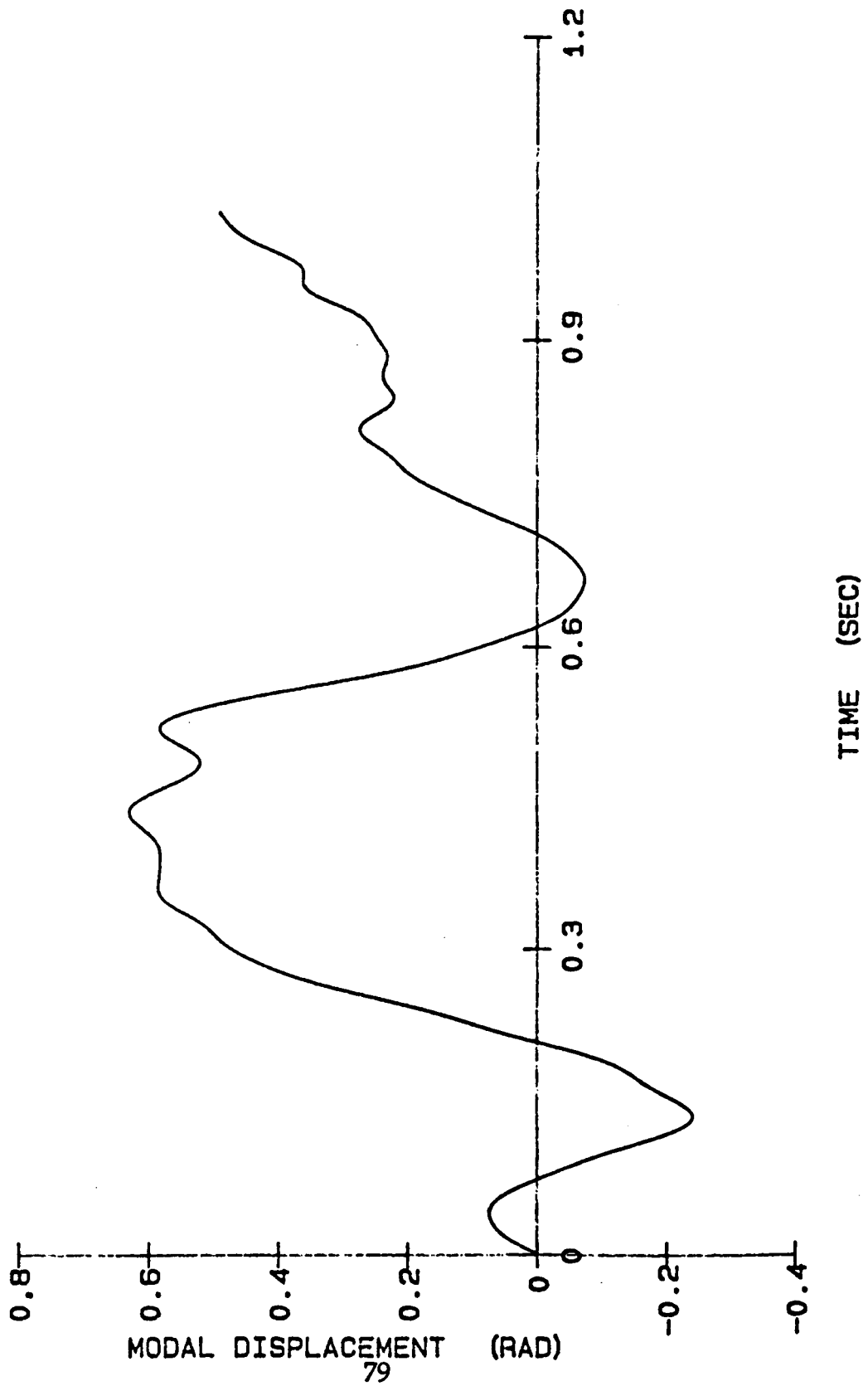


FIG. 5.24 FIRST MODE VELOCITY ESTIMATE

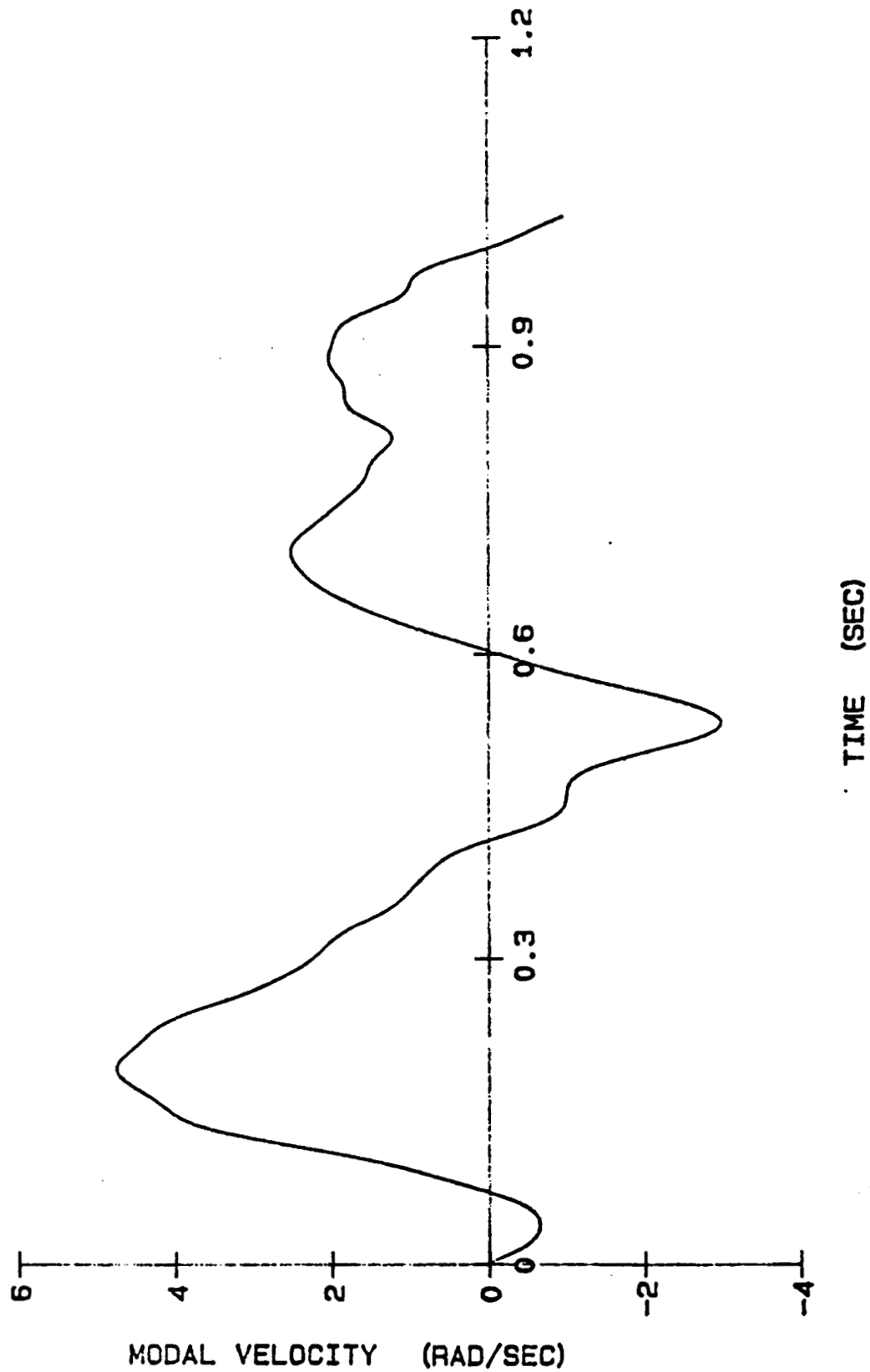


FIG. 5.25 FIRST MODE ACCELERATION MEASUREMENTS

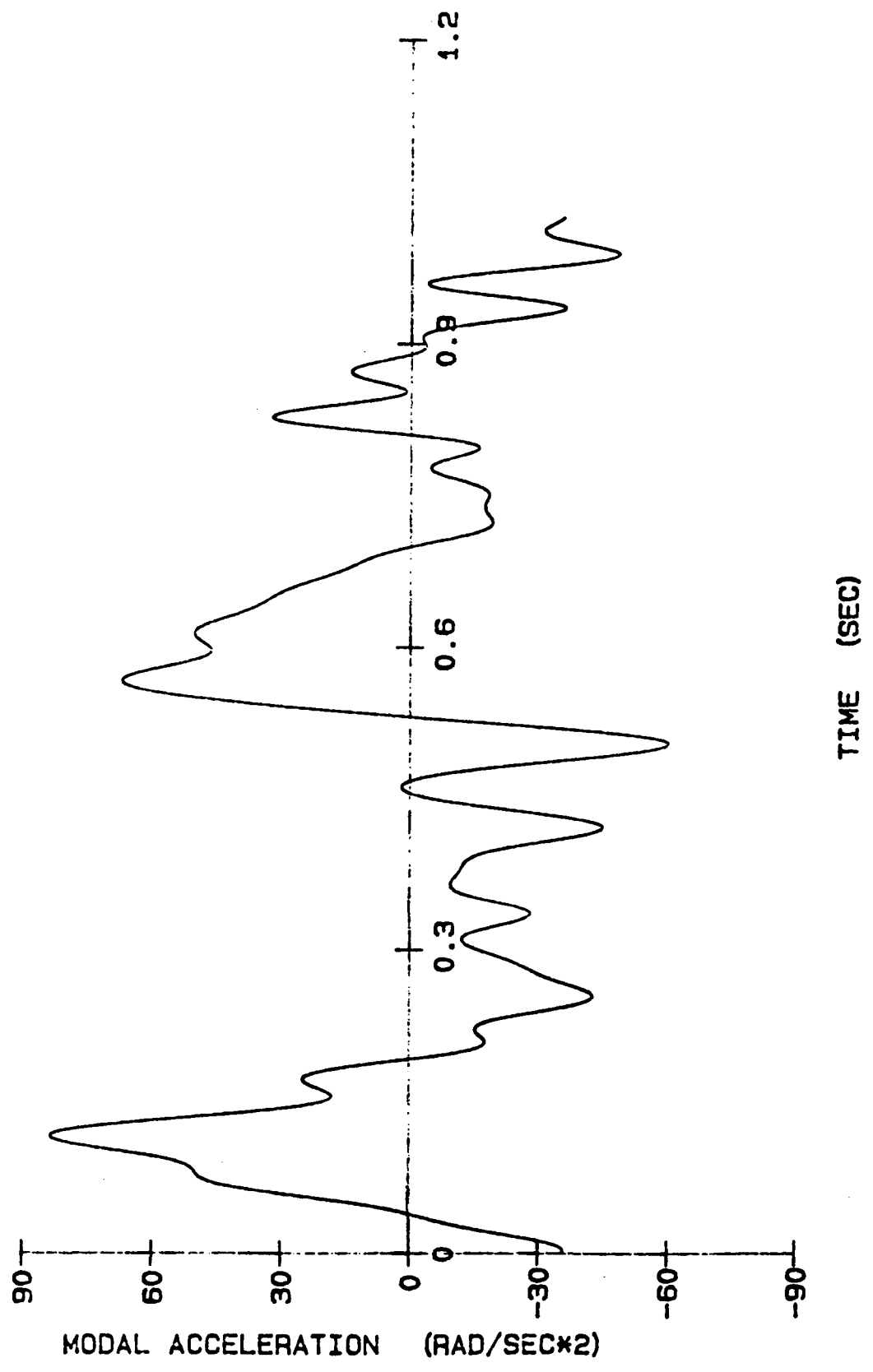


FIG. 5.26 ESTIMATED SECOND MODE DISPLACEMENT

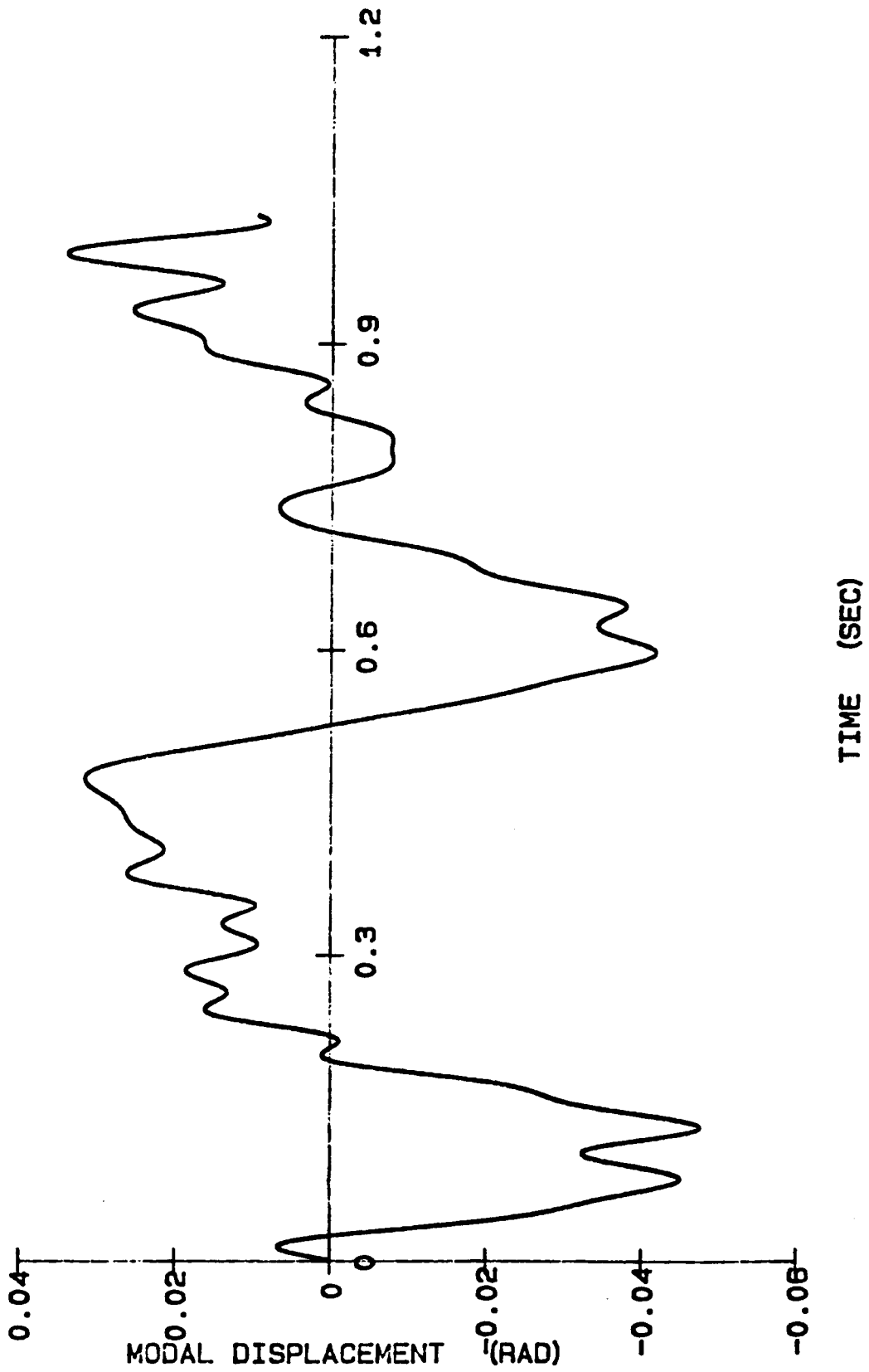


FIG. 5.27 SECOND MODE VELOCITY ESTIMATE

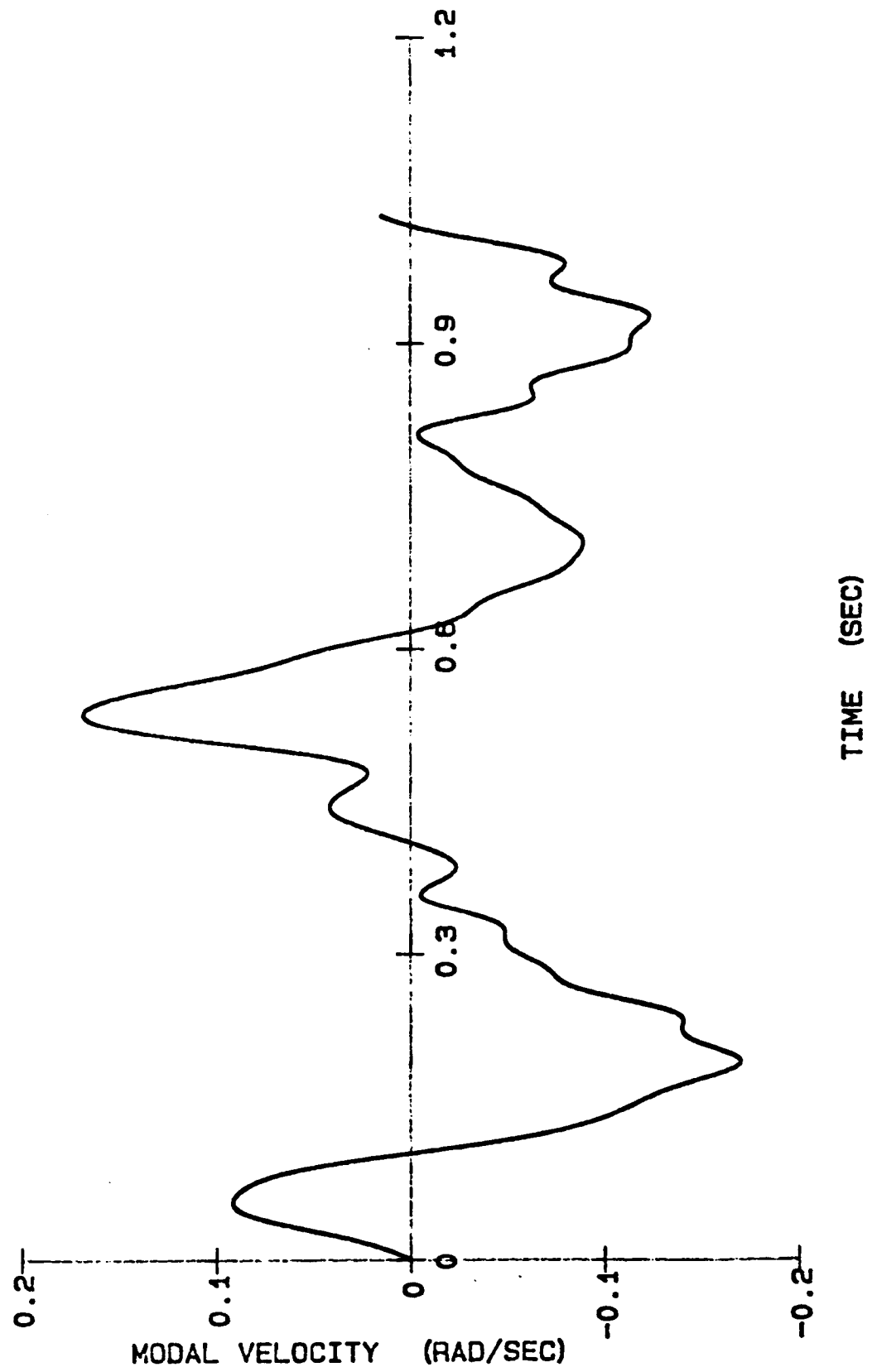


FIG. 5.28 SECOND MODE ACCELERATION MEASUREMENTS

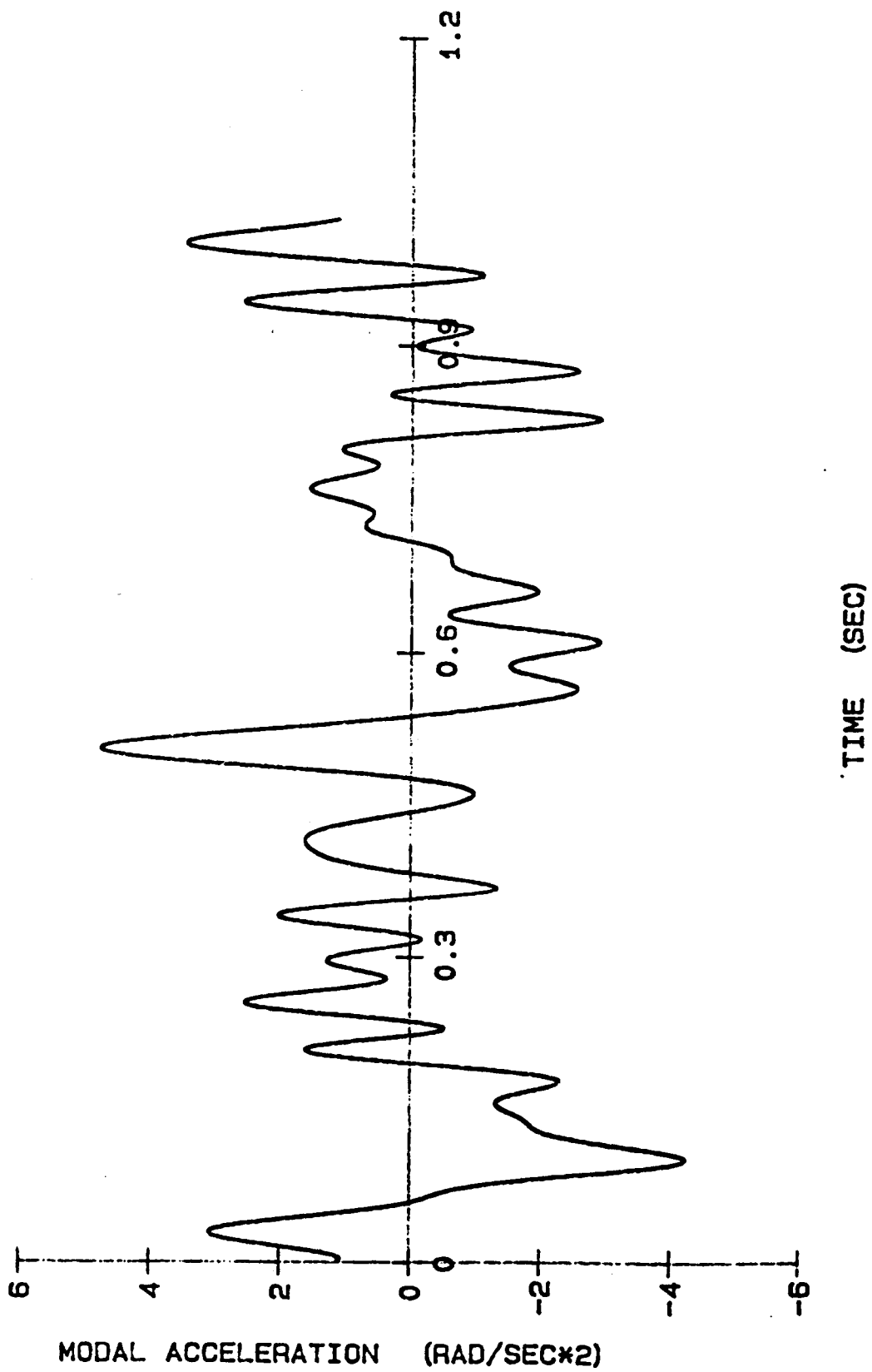


FIG. 5.29 ESTIMATED NON-DIMENSIONAL FLAP SPRING COEFFICIENT

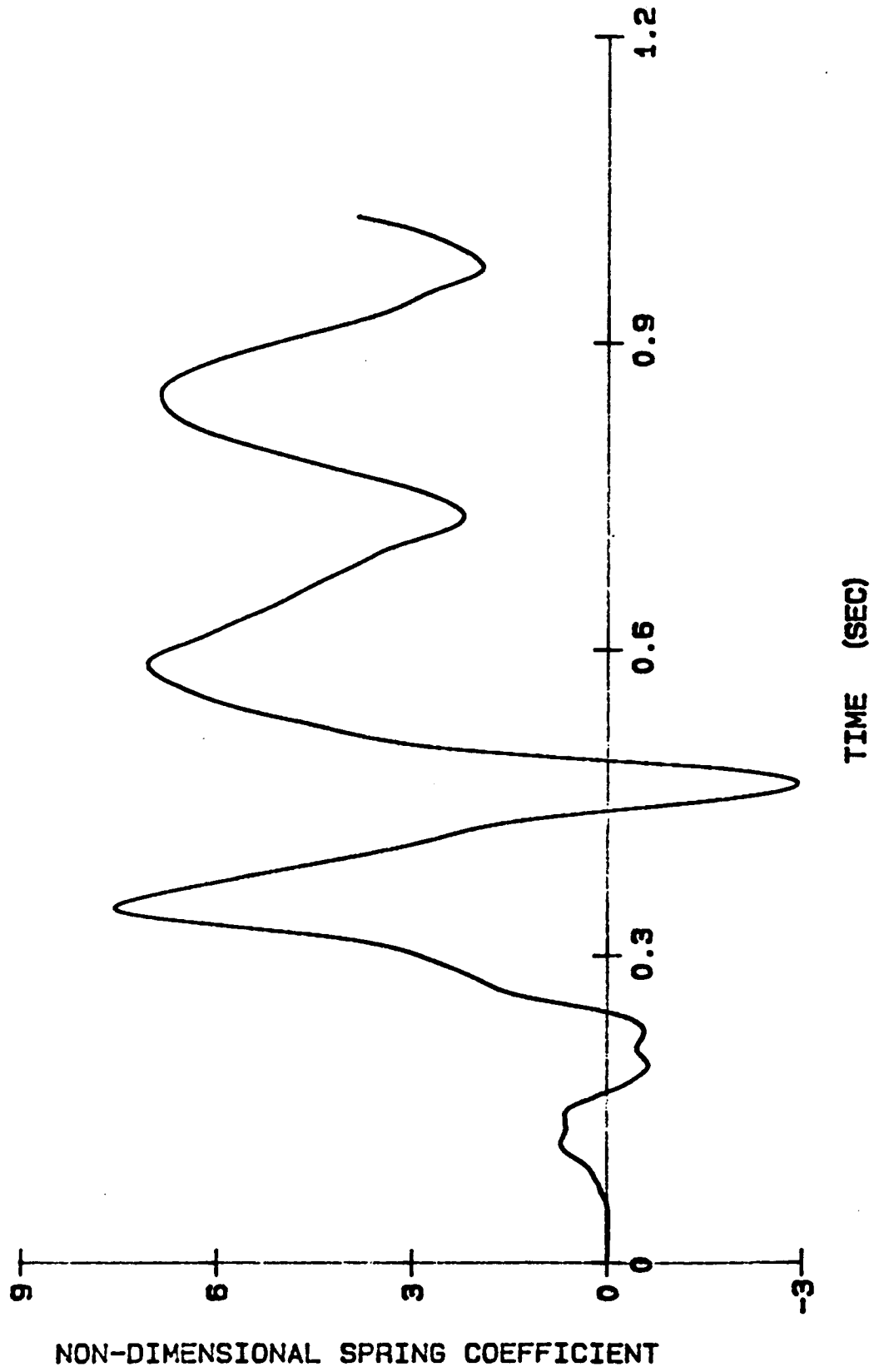


FIG. 5.30 ESTIMATED NON-DIMENSIONAL FLAP DAMPING COEFFICIENT

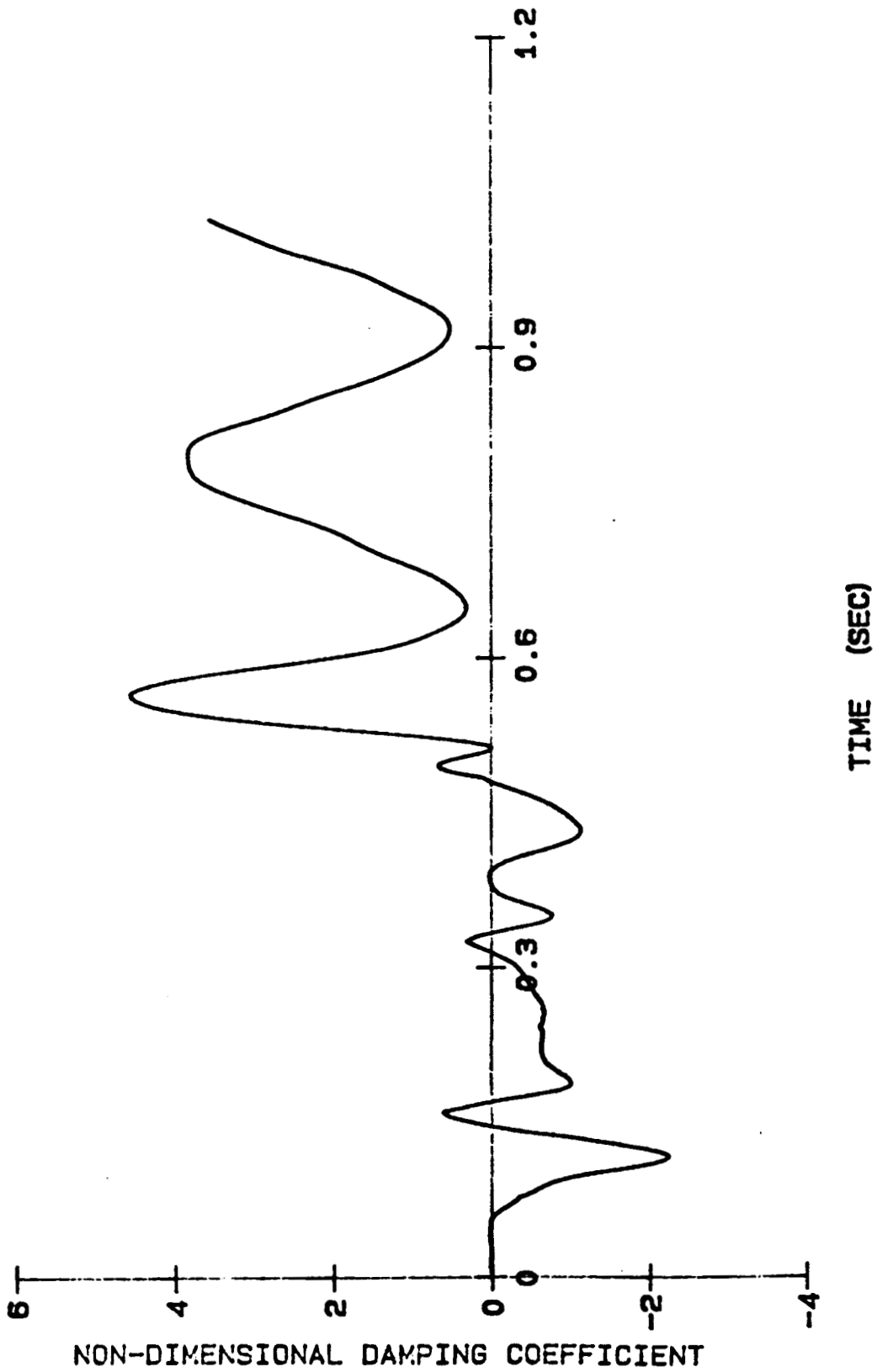


FIG. 5.31 FIRST MODE PITCH FORCING COEFFICIENT

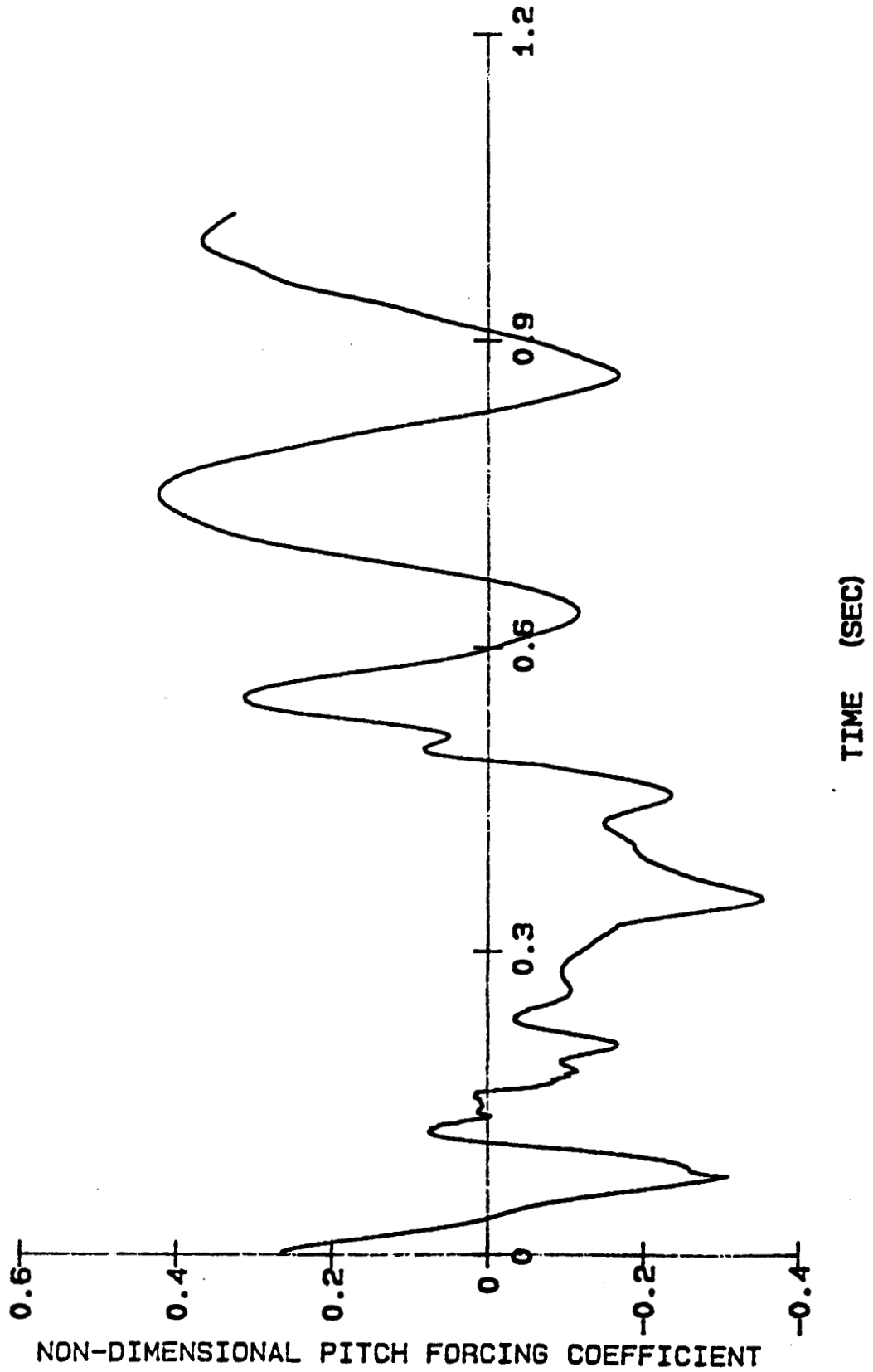
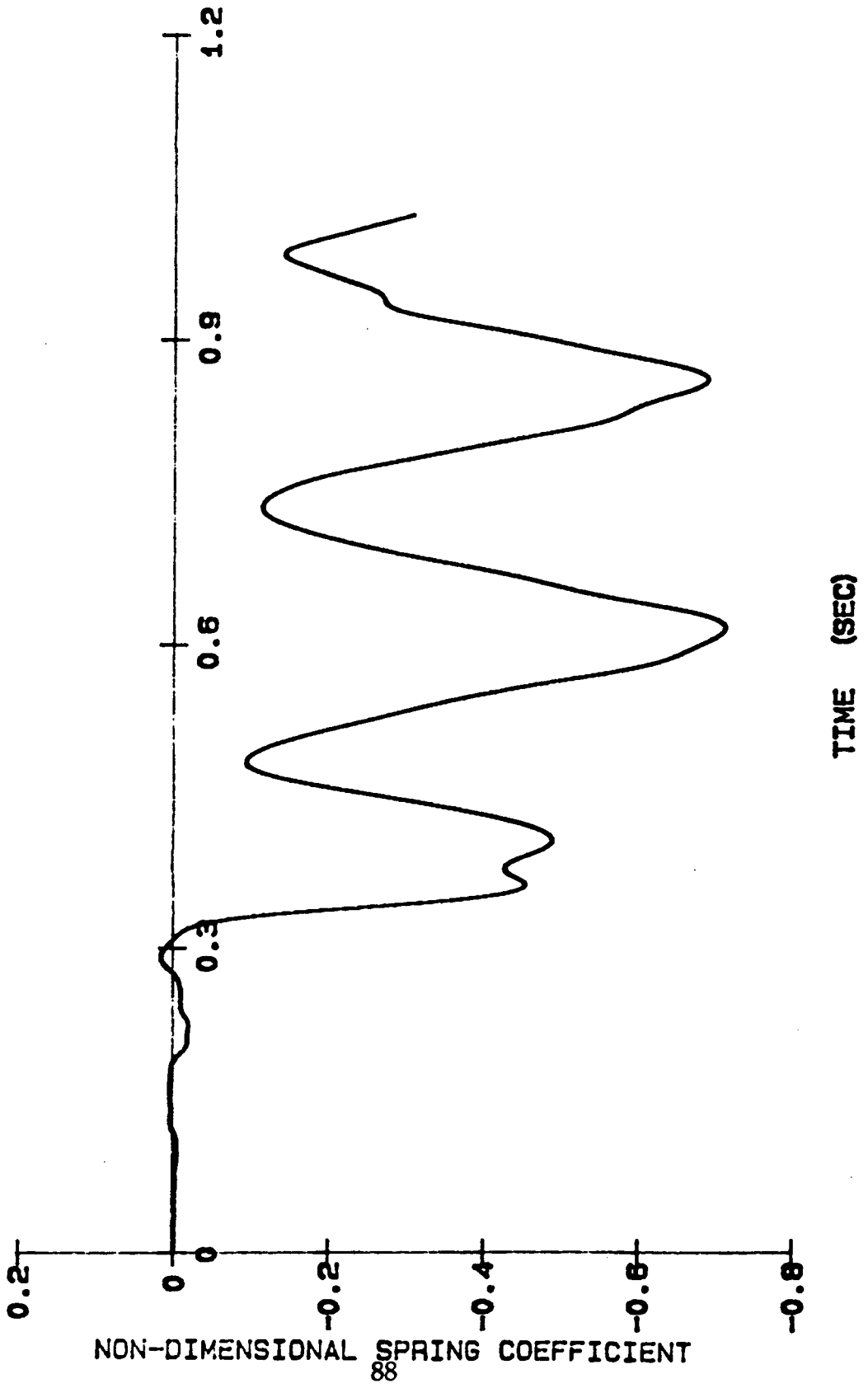


FIG. 5.32 SECOND BENDING MODE SPRING COEFFICIENT



C-2

FIG. 5.33 SECOND BENDING MODE DAMPING COEFFICIENT

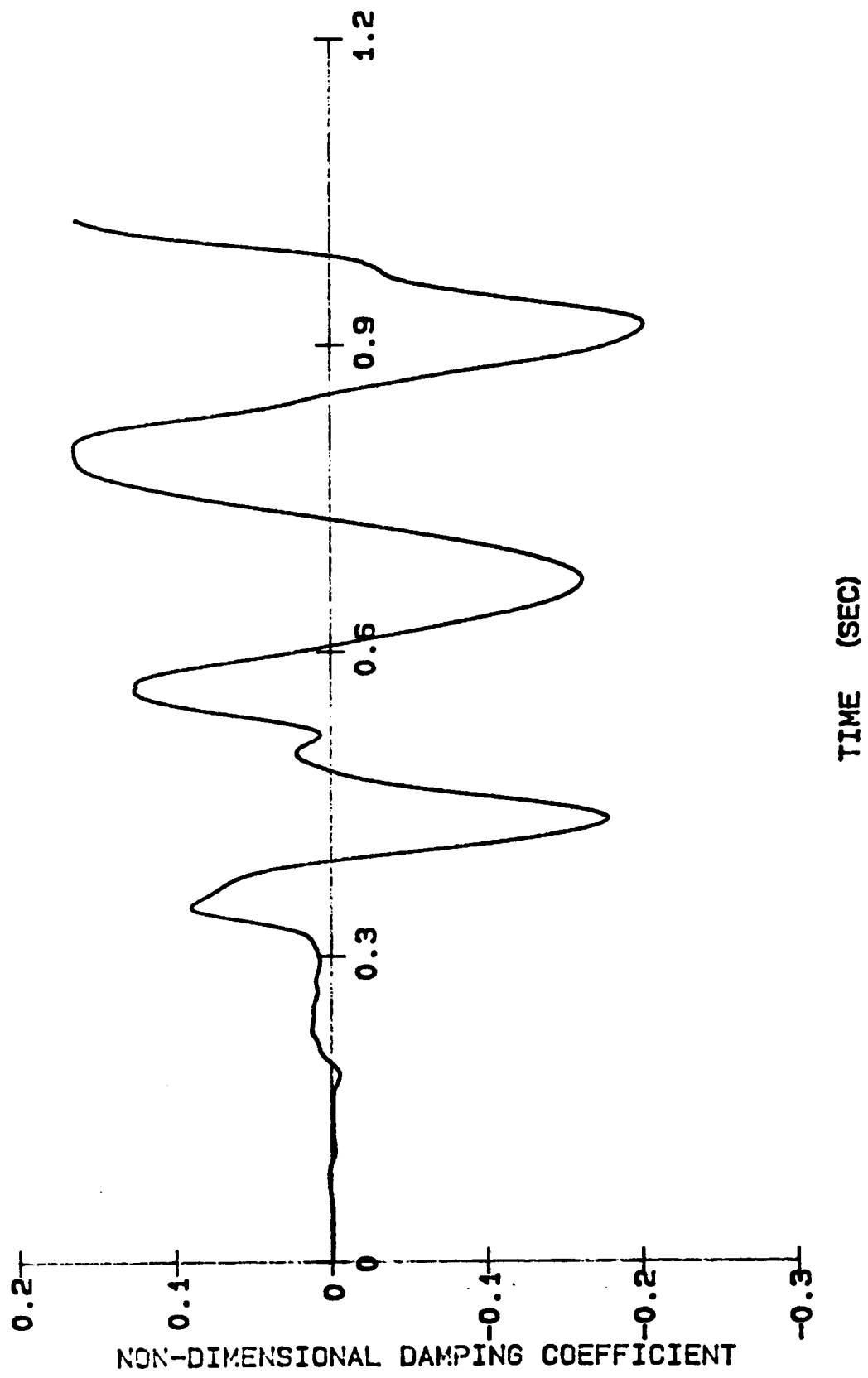
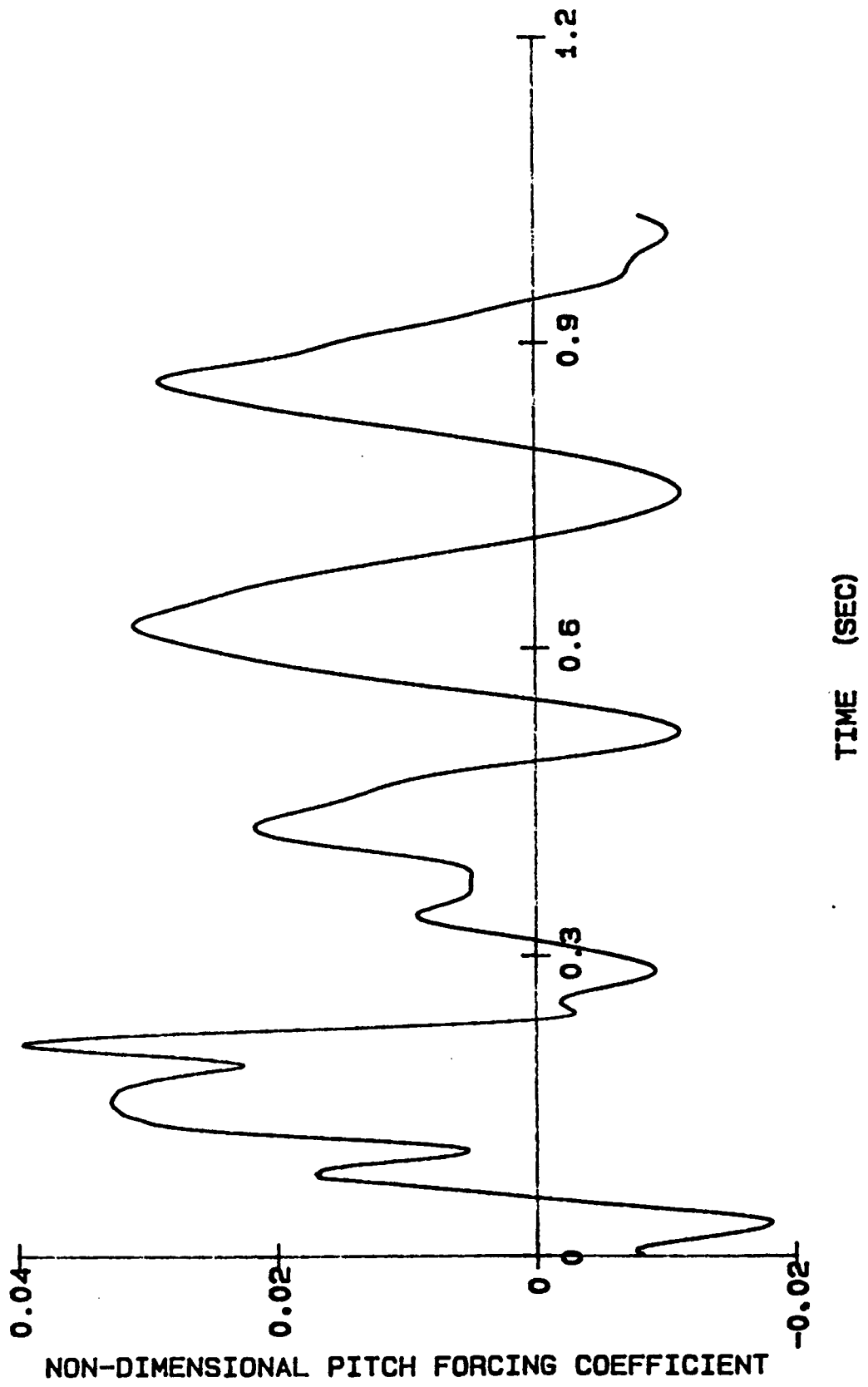


FIG. 5.34 SECOND BENDING MODE PITCH FORCING COEFFICIENT



References

- 1) Fay, John, *The Helicopter; history, piloting and how it flies*, David & Charles, Inc., North Pomfret, Vt, 1976.
- 2) Shaw, John, Albion, Nicholas, Hanker, Edward J. Jr, and Teal, Richard S., *Higher Harmonic Control: wind tunnel demonstration of fully effective vibratory hub force suppression*, *Journal of the AHS*, January, 1989.
- 3) Johnson, Wayne, *Helicopter Theory*, Princeton University Press, 1980.
- 4) Bramwell, A. R. S., *Helicopter Dynamics*, Edward Arnold Ltd, London, 1976.
- 5) Putman, W., Curtiss, H. Jr., and Lapins, M., *Low Speed Testing Techniques for V/STOL Aircraft in the Princeton Dynamic Model Track*, Proc., AIAA 17th Aerospace Sciences Meeting, New Orleans, La, January, 1979.
- 6) McKillip, Robert M. Jr., *Active control rotor model testing at Princeton's Rotorcraft Dynamics Laboratory*, 2nd International Conference on Rotorcraft Basic Research, University of Maryland, Md, February, 1988.
- 7) Demko, Michael G., *High Speed Data Acquisition for the Princeton University Dynamic Model Track*, Master's Thesis, MAE Department, Princeton University, Princeton, NJ, November, 1987.
- 8) McKillip, Robert M. Jr., *Experimental Studies in System Identification of Helicopter Rotor Dynamics*, 14th European Rotorcraft Forum, Milano, Italy, September, 1988.
- 9) *Technical Manual, PDS-700-45, manual # M-4247, AYDIN VECTOR*, 31 January, 1985.

- 10) Technical Manual, PAD-400-2, manual # M-4054, AYDIN VECTOR, 31 January, 1985.
- 11) Hardy, Greg, Analysis and Design Methodology for Aeroelastic Model Construction, Senior Independent Work, MAE Department, Princeton University, Princeton, NJ, January, 1988.
- 12) Halvorsen, William G., and Brown, David L., Impulse Technique for Structural Frequency Response Testing, Cincinnati, Ohio.
- 13) Yntema, Robert T., Simplified Procedures and Charts for the rapid Estimation of Bending Frequencies of Rotating Beams, National Advisory Committee for Aeronautics Technical Note 3459, Langley Aeronautical Laboratory, Langley Field, Va, June, 1955.
- 14) Meirovitch, Leonard, Elements of Vibration Analysis, McGraw-Hill, Inc., USA, 1986.
- 15) McKillip, Robert M. Jr., Criteria for Determining the Spanwise Position of Flatwise Accelerometers on the Blades of the NASA Ames RTR Model Helicopter, January, 1987.
- 16) McKillip, Robert M. Jr., Kinematic Observers for Active Control of Helicopter Rotor Vibration, Vertica, Volume 12, No. 1/2, pp. 1-11, 1988.
- 17) Moroney, M. J., Facts from Figures, Cox & Wyman Ltd., London, 1951.
- 18) Stengel, Robert F., Stochastic Optimal Control, John Wiley & Sons Inc., 1986.
- 19) Ham, N. D., Helicopter Blade Flutter, AGARD Report No. 607, January, 1973.

APPENDIX

SET ISO ZUP

WINDOW XA:< 0 8 > YA:< 0 5 > ZA:< -3 3 >

NOTE ASSIGN Y-VALUES AT EACH DATA POINT TO VARIABLES USED FOR
NOTE COMPARISONS LATER ON

V2=-.12004

V3=-.11606

V4=-.10588

V5=-.09126

V6=-.07328

V7=-.05246

V8=-.02896

V9=-.01614

V10=-.00252

V12=.6

V13=.8

V14=1.0

V15=1.2

V16=1.4

V17=1.6

V18=1.8

V19=1.9

V20=2.0

NOTE ASSIGN VALUES TO POINTS STARTING FROM TRAILING EDGE MOVING

NOTE OVER IN .05 IN STEPS UP TO 30 % OF THE AIRFOIL

NOTE START LOOP FOR FIRST 29 SETS OF POINTS

NOTE V21 IS THE Y-VALUE ALONG THE CHORD DIRECTION FROM 2 TO 0

V21=2.0

NOTE V22 IS THE # USED TO CHECK AT WHICH POINT WE ARE

V22=20

NOTE V11 REPRESENTS THE POINT NUMBERS FROM 1 TO 80

V11=1

DO 20

V22=V22-1

UNTIL (V22 < 12)

DO 10

UNTIL (V21 < V(V22))

V(23)=V22-10

V(25)=V22-9

V(27)=V22+1

$V(26) = (((V(V23) - V(V25)) / (V(V22) - V(V27))) * (V21 - V(V27))) + V(V25)$

V(24)=V11+80

P(V11)=XA:1 YA:(V21) ZA:(V26)

P(V24)=XA:7 YA:(V21) ZA:(V26)

V11=V11+1

V21=V21-.05

ENDDO

ENDDO

NOTE NOW START THE SAME PROCEDURE FOR THE LAST 30 % OF AIRFOIL

V1=-.0249

V2=-.03788

V3=-.0523

V4=-.0711

V5=-.084

V6=-.09366

V7=-.1069

V8=-.11474

V9=-.11882

V10=-.12004

V11=.01214

```

V12=.025
V13=.05
V14=.1
V15=.15
V16=.2
V17=.3
V18=.4
V19=.5
V20=.6
V21=.6
V22=20
V11=29
DO 20
  V22=V22-1
  UNTIL ( V22 < 12 )
  DO 12
    UNTIL ( V21 < V(V22) )
    V(23)=V22-10
    V(25)=V22-9
    V(27)=V22+1
    V(26)={(((V(V23)-V(V25))/(V(V22)-V(V27)))*(V21-V(V27)))+V(V25))
    V(24)=V11+80
    P(V11)=XA:1 YA:(V21) ZA:(V26)
    P(V24)=XA:7 YA:(V21) ZA:(V26)
    V11=V11+1
    V21=V21-.012
  ENDDO
ENDDO
P77=XA:1 YA:.025 ZA:-.03788
P157=XA:7 YA:.025 ZA:-.03788
P78=XA:1 YA:.01214 ZA:-.0249
P158=XA:7 YA:.01214 ZA:-.0249
P79=XA:1 YA:.0027 ZA:-.01285
P159=XA:7 YA:.0027 ZA:-.01285
P80=XA:1 YA:0 ZA:0
P160=XA:7 YA:0 ZA:0
NOTE START THE MILLING PROCEDURE
HOME XA+4 YA+1 ZA+3
V7=1
DO 3
  IF ( V7 = 1 )
    V6=.065
    V5=20
  ELSE
  ENDIF
  IF ( V7 = 2 )
    V6=.01
    V5=20
  ELSE
  ENDIF
  IF ( V7 = 3 )
    V6=0
    V5=10
  ELSE
  ENDIF
  TOOL #1 D.375 F(V5)
  TOOL #2 D.0625 F(V5)
  IF ( V7 = 1 )
  ELSE
  MOUNT #1

```

```
COMP RIGHT
V1=81
M10=(V6)IN
DO 29
  V2=V1-80
  RAPID XA:7
  FEED P(V1)
  FEED P(V1) P(V2)
  RAPID ZA:1
  V1=V1+1
ENDDO
COMP OFF
HOME
ENDIF
MOUNT #2
COMP RIGHT
V3=30
M10=(V6)IN
DO 51
  V4=V3+80
  RAPID XA:1
  FEED P(V3)
  FEED P(V3) P(V4)
  RAPID ZA:1
  V3=V3+1
ENDDO
COMP OFF
HOME
V7=V7+1
ENDDO
DONE
```